

A Comparative Study of NJL and Sakai-Sugimoto Models

D. Yamada

*Racah Institute of Physics, The Hebrew University of Jerusalem,
Givat Ram, Jerusalem, 91904 Israel*

daisuke@phys.huji.ac.il

Abstract

The Nambu–Jona-Lasinio and Sakai–Sugimoto models are juxtaposed, focusing on the models' dynamically generated masses and the phase diagrams. The models are studied in the parameter space of temperature, constant electromagnetic fields and the quark chemical potential. When the chemical potential is zero or small, the models show good agreement. However, the responses of the models under the large chemical potential are very different. In the presence of the background magnetic field, while the large chemical potential triggers the de Haas-van Alphen oscillation and the boundstate destabilization effect of the magnetic field in the NJL model, the Sakai-Sugimoto model completely fails to capture these phenomena, indicating the lack of the fermi sphere in the latter model. Also the orders of the chiral phase transitions are generally different.

Contents

1	Introduction	3
2	NJL Model	6
2.1	Axial Anomaly	7
2.2	Effective Action	8
2.3	Worldline Formalism	10
2.4	Finite Temperature and Chemical Potential	11
2.5	The Effective Potential	13
2.5.1	Pure B Background	15
2.5.2	Pure E Background	17
2.6	Numerical Evaluation	19
2.6.1	General Observation without Electromagnetic Fields	19
2.6.2	Pure B Background	21
2.6.3	Pure E Background	29
3	Sakai-Sugimoto Model	32
3.1	Chiral Phase Transition and Dynamical Mass	32
3.2	External Parameters	34
3.3	Probe Action and Equations of Motion	36
3.4	Confined Phase	39
3.5	Deconfined Phase	41
3.6	Numerical Evaluation	44
3.6.1	Confined Phase	44
3.6.2	Deconfined Phase	47
4	Comparison	52
4.1	General Observation	52
4.2	Pure B Background	54
4.3	Pure E Background	55
5	Conclusion	55
A	Path Integrals of the Worldline Fields	56
B	Computation of the Functions of $F_{\mu\nu}$	58
C	Treatment of Large Chemical Potential	61

1 Introduction

It has been a while since QCD, the color dynamics, was generally accepted as the theory of strong interaction. Our firm confidence in it mainly comes from the remarkable successes at high energy. In the regime of low energy, however, the degrees of freedom are apparently different from the QCD fundamental particles and we still do not quite understand the mechanism that governs this change in the degrees of freedom. The essence of the problem is the strongly coupled nature of QCD at low energy and the lack of powerful and efficient tools to tackle such theories. Currently, the best tool available is the lattice simulation of QCD and it has been providing affirmative results for QCD even in the low energy regime. Though the lattice simulation is powerful, it has its own weaknesses. For example, it suffers from the notorious “sign problem” when chemical potentials are included in the theory. Therefore, different approaches to the low energy QCD are both essential and important. One such approach is the construction of low energy effective theories, guided by the symmetries of QCD. The famous models along this line are the Nambu–Jona-Lasinio (NJL) model [1] and the chiral perturbation theory, and they are both known to be phenomenologically viable. The prominent feature of the NJL model, in particular, is the dynamical breaking of the chiral symmetry. Because of this feature and the sheer simplicity, this model has been popular, despite the model’s deficiencies, such as the lack of the color gauge fields and confinement, also the model is nonrenormalizable and the cutoff must be explicitly introduced as a part of the definition of the theory.

On the other hand, a very different method to handle strongly coupled field theories emerged as the AdS/CFT correspondence or holography [2, 3, 4]. It is the duality between string theory on the AdS space and a conformal field theory. In the low energy limit, the duality boils down to the equivalence between a gravitational system and a strongly coupled conformal field theory, and therefore, to obtain the information about the latter, one can instead study the gravitational theory, which can be easier to analyze. The dual field theory in the original correspondence is not like QCD, and the search for the holographic dual of QCD has been naturally conducted intensively. One of the most attractive models out of the effort is the Sakai-Sugimoto (SS) model [5]. What makes this model attractive is the intuitive geometric implementation of the dynamical chiral symmetry breaking. Furthermore, it is remarkable that one can obtain the spectrum of the theory, such as mesons, in relative ease. Therefore, even though the model does not exactly correspond to QCD in many parameters, such as the number of the color degrees of freedom, the spectrum of the SS model has been naively compared with the QCD experimental and lattice data. Surprisingly, the data agree fairly well, and it is currently popular to suppose a sort of “universality class” among QCD-like strongly coupled theories with various differences in parameters.

Even with those successes, it is difficult to directly compare the SS model and QCD in more details, such as the response of the theories under external electromagnetic field and chemical potentials. This, of course, is because the strongly coupled QCD cannot be solved analytically and the corresponding experimental setup is hard to achieve. This makes it hard to tell to what extent the holographic model captures the features of QCD. In other words, it is unclear how universal the universality is. Therefore, in this paper, we turn to the NJL model, instead of QCD, to contrast with the SS model. The main motivation is the dynamical chiral symmetry breaking of the models and this allows us to investigate the chiral phase diagrams of the theories in various external parameters and

compare. Additionally, one can compute the dynamically generated masses in both theories and collate the response of the masses under different external conditions. We focus on those two properties of the models in the comparison. In order to dig out the similarities and dissimilarities, we scrutinize the responses of the models in the parameter space of temperature, background constant electromagnetic fields and the quark chemical potential. Each model has an extra parameter, the four-fermion coupling for NJL and the asymptotic inter-brane distance for SS, and we examine the models with respect to those parameters as well.

We consider both theories for $N_f = 1$, this is because of its simplicity, and more importantly because the constant background fields introduced in the SS model in this case exactly correspond to the electromagnetic fields (we will mention this point more carefully in Section 3). However, we remark that the generalization to $N_f > 1$ is straightforward. We take the large N_c limit of the NJL model and the cutoff of this nonrenormalizable theory is left as a parameter and we measure all the quantities in terms of this scale. Similarly, the quantities in the SS model are all measured in the units of the curvature scale, R . As for the NJL coupling, we investigate its relation to the inter-brane distance of the SS model. (The parameters of the NJL model are usually adjusted to be consistent with the experimental data. Most commonly, the NJL coupling and the cutoff are tuned to reproduce the scalar density and the pion decay constant from the experiment. See *e.g.*, References [6, 7].)

The general approaches to the models are the followings. The effective potential of the NJL model is derived by utilizing the worldline formalism [8, 9]. This is known as “the string inspired method” and the reader might feel more comfortable than other methods. Finite temperature is introduced by the imaginary time formalism. We pay attention to the subtlety with the gauge invariance in the presence of the topologically non-trivial time circle, and show that the careful treatment results in the automatic introduction of the chemical potential. For the SS model, the background fields and the chemical potential are introduced from the constant NSNS- B field, similar to Reference [10]. We touch on the issue of the topological constraints on the constant fields and argue that the violation of the constraint directly leads to the instability of the system.

Since both models are studied extensively, it is worthwhile to summarize what are known and what are the novel aspects of this work. First for the NJL part. Among many others, the work by Shovkovy in Reference [11] comes closest to our goal. (See Reference [13] for the similar work.) The worldline formalism is adopted in the reference for the derivation of the one-loop effective potential at finite temperature in the context of QED. The one-loop computation is exact in the large N_c limit and the resulting effective potential is identical to the NJL model. However, as pointed out by Gies [12], Shovkovy glosses over the subtlety of the gauge invariance at finite temperature. As mentioned above, we treat this issue carefully and reproduce Gies’ result in the worldline formalism. In addition to reproducing the result of Reference [12], we apply the Poisson (re)summation formula to obtain the effective potential in more physically transparent and numerically useful form and explain how to treat large values of the chemical potential. Then we proceed to actually solve the theory numerically as the NJL model (and not as QED).

The notable references for the worldline formalism at zero temperature are [8, 14] and the review paper by Schubert [9]. We mention that the more popular approach than the worldline formalism is the proper-time formalism and it originates from Schwinger’s paper [15]. The notable and relevant works based on the proper-time formalism include Refer-

ences [16, 17, 18, 19, 12].

As for the numerical evaluation of the NJL model, the work by Inagaki *et al.* in Reference [20] explores the model in the parameter space of temperature, constant background magnetic field and the chemical potential. Though their derivation of the effective potential is based on the proper-time formalism, the results significantly overlap with ours. However, since we are not comparing the model with the experimental data but with the SS model, the parameter space explored in our work includes the coupling constant. Moreover, we provide considerably deeper investigation and emphasize the importance of the Fermi sphere, which causes the major differences between the NJL and SS models.

Another relevant work is Reference [21] of Klevansky and Lemmer, which deals specifically with the pure electric field background at zero temperature, and the result overlaps with some of ours. They find the second order chiral phase transition with respect to the external electric field and we reproduce this result. However, in addition to the second order phase transition, we uncover the first order transition at a higher value of the NJL coupling and we believe that this first order chiral phase transition is reported for the first time. Furthermore, we examine the real and imaginary parts of the effective potential and discuss the validity of the conclusion drawn from the real part. (The imaginary part is not discussed in Reference [21].) We then turn on the temperature, in the background of the electric field, and handle this case by the weak background field expansion. Though we are not able to go too far in this direction, we still obtain some information about the dynamical mass and the phase structure. The attempt here is largely new, though the weak field expansion has been discussed briefly in Reference [18].

In above, we have listed papers of the direct relevance to our aim, but there are, of course, many more papers on the NJL model. For those papers, we refer to the review papers [6, 7].

Now for the SS part. Aharony *et al.* have introduced finite temperature in the SS model in the paper [22] and we adopt their setup. The most important result of the paper for us is the existence of the chiral symmetry breaking in the deconfined phase. We will see that the NJL model has direct counterparts to the chiral behaviors of the SS model in the deconfined phase. The constituent mass of the holographic theories was first discussed by Casero *et al.* in Reference [23] for slightly different model from the SS model but exactly the same idea applies to SS and this is pointed out and examined in References [22, 24].

The references listed thus far deal with the single external parameter, temperature. The introduction of the chemical potential in the SS model was first discussed by Horigome and Tanii in Reference [25]. Even though the way we introduce the chemical potential is slightly different from theirs, we essentially follow and reproduce their work as a special case.

The SS model under the influence of the constant background electromagnetic field has been extensively studied by the group in Haifa [26, 27, 28] and by others [29, 30, 31]. Reference [26] obtains the E - T and B - T chiral phase diagrams and Reference [29] works out the B - T phase diagram and the response of the dynamical quark mass (m^*) with respect to the B field. In addition to reproducing these results, we also produce μ - T , B - μ chiral phase diagrams and T - m^* , E - m^* graphs. In other words, we work out all the properties that have counterpart in the NJL model.

The juxtaposition of the NJL and SS models is the aim of this paper and this comparative study is the main novelty of this work.

Finally, the table of contents is a good guidance to the structure of this article.

2 NJL Model

We start with the NJL model. Good review papers on this model are References [6, 7], but the following discussions will be self-contained for our purposes. As mentioned in the introduction, we consider the NJL model with one flavor in large N_c limit and some parts of the discussion are specialized for this case. We also note that throughout this work we use the Euclidean sign convention, including the γ matrices.

The NJL Lagrangian is

$$\mathcal{L} = \bar{q}i\not{\partial}q + \frac{g^2}{2N_c\Lambda^2} [(\bar{q}q)^2 + (\bar{q}i\gamma_5q)^2], \quad (1)$$

where we introduced the dimensionless coupling g and an arbitrary momentum scale Λ , which we will take to be the cutoff scale of this nonrenormalizable theory.¹ We have abbreviated the summation over the color indices and explicitly, for instance, we have

$$(\bar{q}q)^2 := \left(\sum_{a=1}^{N_c} \bar{q}^a q^a \right)^2. \quad (2)$$

We emphasize that g is the (effective) four-fermion coupling and it does not correspond to the usual “strong coupling” of AdS/CFT. Comparing to the standard NJL Lagrangian, our Lagrangian lacks the flavor structure, because we are concentrating on the one-flavor case.

This Lagrangian has the $U(1)_L \times U(1)_R$ symmetry, that is, it is invariant under the transformations

$$q_{L,R} \rightarrow e^{i\theta_{L,R}/2} q_{L,R}, \quad \bar{q}_{L,R} \rightarrow e^{-i\theta_{L,R}/2} \bar{q}_{L,R}, \quad (3)$$

where $\theta_{L,R}$ are arbitrary real numbers and we have defined

$$q_{L,R} := \frac{1}{2}(1 \mp \gamma_5)q, \quad \bar{q}_{L,R} := \bar{q}\frac{1}{2}(1 \pm \gamma_5), \quad (4)$$

with the convention $\gamma_5^2 = 1$. With those definitions, we have

$$\bar{q}q = \bar{q}_R q_L + \bar{q}_L q_R, \quad \bar{q}i\gamma_5q = -i(\bar{q}_R q_L - \bar{q}_L q_R), \quad (5)$$

and above relations make it clear that the invariance is achieved only when we have *both* quartic interactions of Equation (1); each quartic interaction is not chirally invariant.

For the special case where we have $\theta_V := \theta_L \equiv \theta_R$, the symmetry is the diagonal vector part $U(1)_V$ and the corresponding transformation is

$$q \rightarrow e^{i\theta_V/2} q, \quad \bar{q} \rightarrow \bar{q} e^{-i\theta_V/2}, \quad (6)$$

which leads to the quark number conservation. On the other hand, when $\theta_A := -\theta_L \equiv \theta_R$, we have the $U(1)_A$ transformation

$$q \rightarrow e^{-i\theta_A\gamma_5/2} q, \quad \bar{q} \rightarrow \bar{q} e^{-i\theta_A\gamma_5/2}. \quad (7)$$

¹ Commonly, the coupling of the four-quark interaction is defined to be $G = g^2\Lambda^{-2}/2$. We find it more convenient to introduce the dimensionless coupling g with the cutoff scale. We will adopt the worldline formalism, so Λ will be the “proptime cutoff” scale, as opposed to the three- or four- momentum cutoff, and this choice is a part of the definition of the theory.

This invariance, if exists, gives the axial current conservation.

We now want to introduce the background abelian gauge field and its interaction with the quarks, with respect to the $U(1)_V$ symmetry. This means that we include the kinetic term of the gauge field in Equation (1), though it is not dynamical, and replace the ordinary derivative with the covariant derivative

$$D_\mu = \partial_\mu + iA_\mu , \quad (8)$$

where we absorbed the coupling constant in the gauge field. We then have the Lagrangian

$$\mathcal{L} = \bar{q}i\not{D}q + \frac{1}{4}(F_{\mu\nu})^2 + \frac{g^2}{2N_c\Lambda^2}[(\bar{q}q)^2 + (\bar{q}i\gamma_5q)^2] . \quad (9)$$

Note that the sign of the F^2 term is for the Euclidean signature which we are adopting. The explicit expression of F is given in Appendix B and we investigate the cases with *constant* electric and magnetic fields.

It will be convenient to introduce the auxiliary fields σ and π so that the Lagrangian appears as

$$\mathcal{L} = \bar{q}(i\not{D} + g\sigma + g\pi i\gamma_5)q + \frac{1}{4}(F_{\mu\nu})^2 - \frac{1}{2}N_c\Lambda^2(\sigma^2 + \pi^2) . \quad (10)$$

Upon path-integration with respect to the fields σ and π , we recover the original Lagrangian and we have the relations

$$\sigma = \frac{g}{N_c\Lambda^2}(\bar{q}q) \quad \text{and} \quad \pi = \frac{g}{N_c\Lambda^2}(\bar{q}i\gamma_5q) . \quad (11)$$

2.1 Axial Anomaly

The key feature of the NJL model is the dynamical breakdown of the chiral symmetry, and for our simplified one-flavor model, the corresponding symmetry should be $U(1)_A$. However, since we have included the gauge fields, this symmetry does not exist in general.² In fact, the divergence of the axial current is proportional to $F\tilde{F}$, where \tilde{F} is the dual field strength tensor as defined explicitly in Appendix B. Therefore, our model is meaningful only when

$$F\tilde{F} \propto \vec{E} \cdot \vec{B} = 0 , \quad (12)$$

where \vec{E} and \vec{B} are the background electric and magnetic fields, respectively.

When we carry out the actual numerical evaluation, we concentrate on this case. However, up until then, we discuss the model in generality, because it is easy to generalize to the case with $N_f > 1$ and for the sake of the comparison with the SS model.

To see what would be the order parameter of the $U(1)_A$ breaking, we note that the bilinears $\bar{q}q$ and $\bar{q}i\gamma_5q$ transform under (7) as

$$\bar{q}q \rightarrow \cos\theta_A\bar{q}q - \sin\theta_A\bar{q}i\gamma_5q \quad \text{and} \quad \bar{q}i\gamma_5q \rightarrow \sin\theta_A\bar{q}q + \cos\theta_A\bar{q}i\gamma_5q . \quad (13)$$

We thus see that both σ and π are good order parameters, but what we will do is to use the symmetry to rotate away π and consider (the expectation value of) σ as the order parameter of the dynamical $U(1)_A$ breaking.

² The large N_c does not cure this problem, because the gauge fields in focus are not the color gauge fields.

2.2 Effective Action

Given a theory, all the physical information can be conveniently extracted from its effective action and this is especially powerful in determining the groundstate of the theory. We derive the effective action for our NJL model up to the one-loop order, which is exact in the large N_c limit. There are several ways to construct the effective action, but we closely follow the classic paper by Coleman and Weinberg [32] (see also Reference [16]). Provided that we avoid the anomalous case, the effective action, of course, is invariant under the full $U(1)_L \times U(1)_R$ symmetry. That is, it depends only on $(\sigma^2 + \pi^2)$, therefore, as mentioned at the end of the previous subsection, we set $\pi = 0$ and derive the effective action with respect to the classical value of σ .

We first quickly review how the effective action can determine the groundstate of the theory. Define the connected (Euclidean) Green's functional $W[J]$ by the relation

$$Z = e^{-W[J]} = \int \mathcal{D}q \mathcal{D}\bar{q} \mathcal{D}\sigma \exp\left[- \int dx^4 (\mathcal{L} + J\sigma)\right], \quad (14)$$

where \mathcal{L} is given in Equation (10), without the π field, and the function $J(x)$ is the source for the field $\sigma(x)$. Since we are interested in a constant background electromagnetic field, we have omitted the path integral over A_μ . We then have

$$\frac{\delta W[J]}{\delta J(x)} = - \frac{\delta \ln Z}{\delta J(x)} = \langle \Omega | \sigma(x) | \Omega \rangle_J, \quad (15)$$

where $|\Omega\rangle_J$ is the groundstate in the presence of the source J . This implies that we have the classical field $\sigma_{\text{cl}}(x)$

$$\sigma_{\text{cl}}(x) := \frac{\delta W[J]}{\delta J(x)}. \quad (16)$$

We can think of this σ_{cl} as the conjugate of J . Hence we change the variable of the connected Green's function by the functional Legendre transformation

$$\begin{aligned} \Gamma[\sigma_{\text{cl}}] &= W[J] - \int dy^4 \sigma_{\text{cl}}(y) J(y) \\ &= - \ln \int \mathcal{D}q \mathcal{D}\bar{q} \mathcal{D}\sigma \exp\left[- \int dx^4 \{\mathcal{L} + J(\sigma - \sigma_{\text{cl}})\}\right]. \end{aligned} \quad (17)$$

This functional, Γ , satisfies

$$\begin{aligned} \frac{\delta \Gamma[\sigma_{\text{cl}}]}{\delta \sigma_{\text{cl}}(x)} &= \frac{\delta W[J]}{\delta \sigma_{\text{cl}}(x)} - \int dy^4 \frac{\delta J(y)}{\delta \sigma_{\text{cl}}(x)} \sigma_{\text{cl}}(y) - J(x) \\ &= \int dy^4 \frac{\delta J(y)}{\delta \sigma_{\text{cl}}(x)} \frac{\delta W[J]}{\delta J(y)} - \int dy^4 \frac{\delta J(y)}{\delta \sigma_{\text{cl}}(x)} \sigma_{\text{cl}}(y) - J(x) \\ &= - J(x). \end{aligned} \quad (18)$$

Therefore, as we turn off the source J , we obtain

$$\frac{\delta \Gamma[\sigma_{\text{cl}}]}{\delta \sigma_{\text{cl}}(x)} = 0, \quad (19)$$

and this implies that the groundstate of the theory can be obtained by extremizing the functional Γ with respect to the classical field σ_{cl} . This can, in turn, be thought to determine the classical field σ_{cl} in the groundstate.

Now our task is to compute the effective action (17) and we do this to the one-loop order. Note that the path integral over the quark fields are quadratic and can be carried out exactly, yielding the factor

$$\ln \det(i\mathcal{D} + g\sigma) = \frac{1}{2} \ln \det[(\mathcal{D})^2 + g^2\sigma^2] , \quad (20)$$

where we used the usual “ γ_5 -trick”. Now, since we have $\gamma_\mu\gamma_\nu = \delta_{\mu\nu} + [\gamma_\mu, \gamma_\nu]/2$, we get

$$\begin{aligned} (\mathcal{D})^2 &= D^2 + \frac{1}{2}[\gamma_\mu, \gamma_\nu]D_\mu D_\nu = D^2 + \frac{1}{2}\gamma_\mu\gamma_\nu[D_\mu, D_\nu] \\ &= D^2 + \frac{i}{2}\gamma_\mu\gamma_\nu F_{\mu\nu} , \end{aligned} \quad (21)$$

where we used the fact that $[D_\mu, D_\nu] = iF_{\mu\nu}$. Using this relation to Equation (20), we end up with the expression for the effective action

$$\begin{aligned} \Gamma[\sigma_{\text{cl}}(x)] &= - \ln \int \mathcal{D}\sigma \exp \left[- \int dx^4 \left\{ \frac{1}{4}(F_{\mu\nu})^2 - \frac{1}{2}N_c\Lambda^2\sigma^2 \right. \right. \\ &\quad \left. \left. + \frac{1}{2} \text{tr} \ln [D^2 + \frac{i}{2}\gamma_\mu\gamma_\nu F_{\mu\nu} + g^2\sigma^2] + J(\sigma - \sigma_{\text{cl}}) \right\} \right] , \end{aligned} \quad (22)$$

where tr is over the Clifford algebra representation space, the color space and the spacetime momentum. Notice that the extra minus sign from the fermion loop makes the sign in front of the “trace-log” plus.

Now as N_c becomes large, the path integral above is more dominated by the saddle point value at

$$\sigma = \sigma_{\text{cl}} . \quad (23)$$

This statement becomes exact at $N_c = \infty$, on which case we are focusing. In general, we need to perform the derivative expansion at this stage with respect to $\sigma_{\text{cl}}(x)$, as is done in the paper by Coleman and Weinberg [32]. However, since we are interested in the dynamical quark mass, we only need the leading order in the expansion, *i.e.*, the constant σ_{cl} . In other words, we only look for the translationally invariant groundstate. The effective action Γ now is a function with respect to the c -number σ_{cl} and to this end, the spacetime integral in the effective action becomes trivial. Thus, it is common to define the effective potential *via* the relation

$$\Gamma[\sigma_{\text{cl}}] = - \int d^4x V_{\text{eff}}(\sigma_{\text{cl}}) , \quad (24)$$

yielding

$$V_{\text{eff}}(\sigma_{\text{cl}}) = -\frac{1}{4}(F_{\mu\nu})^2 + \frac{1}{2}N_c\Lambda^2\sigma_{\text{cl}}^2 - \frac{1}{2} \text{tr} \ln [D^2 + \frac{i}{2}\gamma_\mu\gamma_\nu F_{\mu\nu} + g^2\sigma_{\text{cl}}^2] . \quad (25)$$

Then the functional relation (19) reduces to a simple differential equation

$$\frac{dV_{\text{eff}}}{d\sigma_{\text{cl}}} = 0 . \quad (26)$$

Figure 1: The tadpole cancellation condition. The dotted and solid lines represent the s and the quark fields, respectively. The second term on the left-hand side comes from the “vertex” $N_c \Lambda^2 \sigma_{\text{cl}}(x)$.

Another way to obtain the effective potential is to utilize the background field method, by shifting the field as $\sigma(x) \rightarrow s(x) + \sigma_{\text{cl}}$ and integrating out the quark field. Then it is clear that Equation (26) is precisely the tadpole cancellation condition as shown in Figure 1. In what follows, we refer this condition as the “tadpole condition”.

2.3 Worldline Formalism

We would like to evaluate the last term in the effective potential (25) and for the convenience, we redefine this term as

$$\hat{V}(m) := \frac{1}{2} \text{tr} \ln [D^2 + \frac{i}{2} \gamma_\mu \gamma_\nu F_{\mu\nu} + m^2], \quad (27)$$

where we recall that the trace is over the color, Dirac and loop momentum spaces, and we have defined the mass parameter

$$m := g\sigma_{\text{cl}}. \quad (28)$$

To evaluate the effective potential, we utilize the worldline formalism that goes along the ideas of string theory [8].

To begin with, we express the function \hat{V} in Schwinger’s proptime [15]. By using the relation³

$$\ln X = - \int_0^\infty \frac{e^{-Xs}}{s} ds, \quad (29)$$

we can write

$$\begin{aligned} \hat{V}(m) &= - \frac{1}{2} \int_0^\infty \frac{ds}{s} \text{tr} \exp[-s(D^2 + \frac{i}{2} \gamma_\mu \gamma_\nu F_{\mu\nu} + m^2)] \\ &= - \frac{1}{2} N_c \int_0^\infty \frac{ds}{s} e^{-m^2 s} \text{tr} \langle x | \exp[-s(D^2 + \frac{i}{2} \gamma_\mu \gamma_\nu F_{\mu\nu})] | x \rangle, \end{aligned} \quad (30)$$

where the operator tr now is only over the representation space of Clifford algebra and the factor N_c came out of the trace over the color space.

Now in the worldline formalism, we want to regard x_μ as fields in the one-dimensional space of circular worldline, parametrized by, say, τ , and express the effective potential in terms of the path integral over the fields $x_\mu(\tau)$. The proper length of the circle’s circumference is the parameter s , which is called “modulus” in the string literature, and the factor $1/s$ in \hat{V} removes the redundancy from the translation and reversal of the worldline coordinate. In order to deal with the last trace over the Clifford representation space, we need

³ This is the analytically continued version of the proptime and is the “imaginary proptime”. Later, we will come back to this point concerning the real and imaginary proptime. We note that this is essentially different from the analytic continuation of the spacetime coordinate.

one more ingredient. What we need to do is very similar to the treatment of worldsheet fermions in superstring theory. We introduce constant Grassmann fields ψ_μ that satisfy

$$\{\psi_\mu, \psi_\nu\} = \delta_{\mu\nu} , \quad (31)$$

and introduce a basis of the Clifford representation space $|\alpha\rangle$ so that

$$\psi_\mu|\alpha\rangle = \frac{1}{\sqrt{2}}(\gamma_\mu)_{\alpha\beta}|\beta\rangle . \quad (32)$$

We then can write

$$\begin{aligned} \hat{V}(m) &= -\frac{1}{2}N_c \int_0^\infty \frac{ds}{s} e^{-m^2 s} \langle \alpha, x | \exp[-s(D^2 + i\psi_\mu \psi_\nu F_{\mu\nu})] | \alpha, x \rangle \\ &= -\frac{1}{2}N_c \int_0^\infty \frac{ds}{s} e^{-m^2 s} \mathcal{N} \int_P \mathcal{D}x(\tau) \int_A \mathcal{D}\psi(\tau) \exp\left[-\int_0^s d\tau (\mathcal{L}_x + \mathcal{L}_\psi)\right] , \end{aligned} \quad (33)$$

with

$$\mathcal{L}_x := \frac{1}{2e'} \dot{x}^2 + iA \cdot \dot{x} \quad \text{and} \quad \mathcal{L}_\psi := \frac{1}{2} \psi \cdot \dot{\psi} - i \frac{e'}{2} \psi \cdot F \cdot \psi . \quad (34)$$

Here the dots on the fields denote the derivative with respect to τ and e' is the einbein of the worldline circle, which can be an arbitrary fixed number because we have decided to encode the moduli in the parameter s (see, for example, Chapter 5 of Polchinski [33]). Hence from now on, we set $e' \equiv 2$, which is the common choice in the literature. As usual, the factor \mathcal{N} arises from the integration over the conjugate momenta to obtain the path integral in the Lagrangian form, and it satisfies the relation

$$\mathcal{N} \int_P \mathcal{D}x \exp\left[-\int_0^s d\tau \frac{1}{4} \dot{x}^2\right] = (4\pi s)^{-d/2} , \quad (35)$$

where d is the spacetime dimension, *i.e.*, 4 in our case. Finally, the subscripts P and A on the path integral symbols imply the boundary conditions of the fields

$$x(0) = x(s) \quad \text{and} \quad \psi(0) = -\psi(s) , \quad (36)$$

for all the components.

Before we proceed further, we discuss the treatment of finite temperature in the context of the worldline formalism.

2.4 Finite Temperature and Chemical Potential

As we have adopted the Euclidean signature, we use the imaginary time formalism to handle finite temperature. This means that the time direction in the spacetime is compactified with the circumference β , and a worldline can wind around this direction. Thus, the path integral should be carried out in each winding sector, and then they must be summed with appropriate statistical factor [34] (see also Refs. [35, 36]). This can be written as

$$P_{xx}^\beta = \sum_{n=-\infty}^{\infty} (-1)^n P_{x(x_0+n\beta, x_i)}^\infty , \quad (37)$$

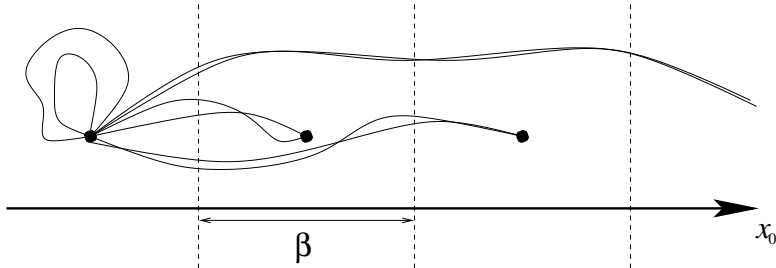


Figure 2: Conceptual picture of the path integral at finite temperature. The left-most loop paths corresponds to $n = 0$, *i.e.*, the $T = 0$ contribution.

where P_{xy} represents the path integral over the paths from a spacetime point x to y and P^∞ means the path integral in \mathbb{R}^4 , *i.e.* without the topological condition. We emphasize that the alternating sign $(-1)^n$ comes from the *spacetime* fermions q , and they should not be confused with the worldline fields. See Figure 2 for a conceptual picture of the path integral.

Let us look at the path integral of $x(\tau)$ in Equation (33). We have the Lagrangian \mathcal{L}_x as shown in Equation (34) and this does not appear to be quadratic in the field $x_\mu(\tau)$. At this point, it is very common that a specific gauge, called the Schwinger-Fock gauge:

$$A_\mu = -\frac{1}{2}F_{\mu\nu}x_\nu, \quad (38)$$

is adopted to bring the Lagrangian into the quadratic form. However, one immediately realizes the problem with this gauge at finite temperature by re-examining Schwinger's original paper [15]. There, the holonomy factor,

$$\Phi(x, y) = \exp \left[i \int_x^y dx_\mu A_\mu(x) \right], \quad (39)$$

appears in the two-point Green's function, while in the gauge (38) this factor is absent. This factor has no relevance if one is interested in the effective potential where $x = y$, and *if the spacetime is topologically trivial*. In the imaginary time formalism of the theory at finite temperature, the latter condition is false. In the geometrical language, the transition function defined as a map from the S^1 time circle to the $U(1)$ gauge group is non-trivial and classified by $\pi_1[U(1)] = \mathbb{Z}$. This in turn implies that the gauge transformation is severely restricted to a certain class and one must be very careful with the gauge fixing. In other words, the consequence of the time circle is (geometrically) exactly the same as the charge quantization of the Dirac monopole and the Aharonov-Bohm effect (see for instance Reference [37]). As in those cases, the parallel transport of the wavefunction around the time circle, *i.e.*, the Polyakov loop, obtains a non-trivial physical significance. As we will see below, this automatically introduces the chemical potential into the system.

Gies [12] appears to be the first one to pointed out this subtlety and he generalized Schwinger's proper-time formalism to finite temperature with the careful treatment of the holonomy factor. We are going to show how this works in the worldline formalism.

To take advantage of the Schwinger-Fock gauge, we split the Lagrangian into the Schwinger-Fock gauge part and the rest

$$\mathcal{L}_x = \frac{1}{4}\dot{x}^2 + i\dot{x} \cdot \left(A + \frac{1}{2}F \cdot x - \frac{1}{2}F \cdot x \right) = \left(\frac{1}{4}\dot{x}^2 - \frac{i}{2}\dot{x} \cdot F \cdot x \right) + i\dot{x} \cdot \left(A + \frac{1}{2}F \cdot x \right). \quad (40)$$

Now the important point is that

$$d\left(A + \frac{1}{2}F \cdot x\right) = 0, \quad (41)$$

and this implies that *within a homotopy class*, the integral

$$\int_0^s d\tau \dot{x} \cdot \left(A + \frac{1}{2}F \cdot x\right) = \int_{x(0)}^{x(s)} dx \cdot \left(A + \frac{1}{2}F \cdot x\right) \quad (42)$$

is independent of the path. Therefore, this factors out of the path-integral. Furthermore, without loss of generality, we may evaluate the x integral of Equation (42) along the straight line in x_0 -direction. In this case, the integral over $F \cdot x$ vanishes due to the anti-symmetry of F and we are left with the integral of A_0 . In what follows, we are going to consider the case with constant A_0 and we define a real number

$$\mu := iA_0. \quad (43)$$

Then we can write

$$\begin{aligned} \hat{V}(m) = & -\frac{1}{2}N_c \int_0^\infty \frac{ds}{s} e^{-m^2 s} \sum_{n=-\infty}^{\infty} (-1)^n e^{-n\beta\mu} \\ & \times \mathcal{N} \int_{x(0)}^{x(s)} \mathcal{D}x(\tau) \int_A \mathcal{D}\psi(\tau) \exp\left\{-\int_0^s d\tau (\mathcal{L}_{xSF} + \mathcal{L}_\psi)\right\}, \end{aligned} \quad (44)$$

with

$$\mathcal{L}_{xSF} := \frac{1}{4}\dot{x}^2 - \frac{i}{2}\dot{x} \cdot F \cdot x \quad \text{and} \quad \mathcal{L}_\psi := \frac{1}{2}\psi \cdot \dot{\psi} - i\psi \cdot F \cdot \psi. \quad (45)$$

The subscript ‘‘SF’’ of the bosonic Lagrangian signifies the form in the Schwinger-Fock gauge. The integer n is the winding number in the x_0 direction and it is also implicitly in $x(s) = x(0) + n\beta\hat{x}_0$, where \hat{x}_0 is the unit vector in the time direction.

2.5 The Effective Potential

In this subsection, we derive the expression for the effective potential that is ready for the numerical evaluation.

In Equation (44), we are interested in the constant F , *i.e.*, it is independent of the paths $x(\tau)$. Thus we can separately calculate the path integrals for the worldline bosonic and fermionic parts,

$$\begin{aligned} I_B & := \mathcal{N} \int_{x(0)}^{x(s)} \mathcal{D}x(\tau) \exp\left(-\int_0^s d\tau \mathcal{L}_{xSF}\right) \\ I_F & := \int_A \mathcal{D}\psi(\tau) \exp\left(-\int_0^s d\tau \mathcal{L}_\psi\right), \end{aligned} \quad (46)$$

where the factor \mathcal{N} naturally comes with the bosonic part because of the relation (35). The evaluation of them is rather lengthy and is given in Appendix A. The results are

$$\begin{aligned} I_B & = (4\pi s)^{-2} \exp\left[-(n\beta/2)^2 \{F \cot(Fs)\}_{00}\right] \left(\det_L \left[\frac{\sin(Fs)}{Fs}\right]\right)^{-1/2} \\ I_F & = 4(\det_L[\cos(Fs)])^{1/2}, \end{aligned} \quad (47)$$

where the functions of the matrix F_μ^ν are defined through the formal power series and \det_L implies the determinant with respect to the matrices with the components in the Lorentz indices. We notice that the Lorentz invariance is explicitly broken in I_B , due to the finite temperature.

At this point, \hat{V} has the form

$$\begin{aligned} \hat{V}(m) = & -\frac{N_c}{8\pi^2} \int_0^\infty ds s^{-3} e^{-m^2 s} (\det_L[\cos(Fs)])^{1/2} \left(\det_L \left[\frac{\sin(Fs)}{Fs} \right] \right)^{-1/2} \\ & \times \sum_{n=-\infty}^{\infty} (-1)^n e^{-n\beta\mu} \exp \left[- (n\beta/2)^2 \{F \cot(Fs)\}_{00} \right]. \end{aligned} \quad (48)$$

In this form, the physical interpretation of the parameter μ is still not clear. Moreover, it turns out that this form is not suitable for the numerical evaluation in a certain range of parameters. Thus, we use the Poisson (re)summation formula

$$\sum_{n=-\infty}^{\infty} \exp(-\pi a n^2 + 2\pi i b n) = a^{-1/2} \sum_{n=-\infty}^{\infty} \exp \left[-\frac{\pi}{a} (n-b)^2 \right], \quad (49)$$

to convert the above expression to

$$\begin{aligned} \hat{V}(m)/N_c = & -\frac{T}{4\pi^{3/2}} \int_0^\infty ds s^{-5/2} \{ (Fs) \cot(Fs) \}_{00}^{-1/2} \{ \det_L [(Fs) \cot(Fs)] \}^{1/2} \\ & \times \sum_{l \in \mathbb{Z}_{1/2}} \exp \left[- \{ (Fs) \cot(Fs) \}_{00}^{-1} (2\pi T l - i\mu)^2 s - m^2 s \right], \end{aligned} \quad (50)$$

where $T := 1/\beta$ and l runs over the half integers $\mathbb{Z}_{1/2} := \{n + 1/2 : n \in \mathbb{Z}\}$. In this form, we see that the parameter μ is the chemical potential, as advertised before. In the standard method, the chemical potential is included from the beginning as a part of the grand partition function (in the end, this amounts to the shift $p_0 \rightarrow p_0 - i\mu$). Contrast to this, the automatic inclusion of the chemical potential we see here is rather remarkable.

We now have to evaluate the terms involving the matrix F . The determinant can be calculated relatively easily by using Schwinger's method [15], but $\{ (Fs) \cot(Fs) \}_{00}$ is not straightforward and for this, we adopt the method of Reference [38] (see also [39]). They are computed in Appendix B and the results are

$$\left\{ \det_L [(Fs) \cot(Fs)] \right\}^{1/2} = s^2 \left| \mathcal{G} \coth \left(s \sqrt{\mathcal{F} + \sqrt{\mathcal{F}^2 + \mathcal{G}^2}} \right) \cot \left(s \sqrt{-\mathcal{F} + \sqrt{\mathcal{F}^2 + \mathcal{G}^2}} \right) \right|, \quad (51)$$

and

$$\begin{aligned} \{ (Fs) \cot(Fs) \}_{00} = & \frac{1}{2\sqrt{\mathcal{F}^2 + \mathcal{G}^2}} \left[\right. \\ & \left\{ -\frac{1}{2}(\vec{B}^2 + \vec{E}^2) + \sqrt{\mathcal{F}^2 + \mathcal{G}^2} \right\} \sqrt{\mathcal{F} + \sqrt{\mathcal{F}^2 + \mathcal{G}^2}} \coth \left(s \sqrt{\mathcal{F} + \sqrt{\mathcal{F}^2 + \mathcal{G}^2}} \right) \\ & + \left\{ \frac{1}{2}(\vec{B}^2 + \vec{E}^2) + \sqrt{\mathcal{F}^2 + \mathcal{G}^2} \right\} \sqrt{-\mathcal{F} + \sqrt{\mathcal{F}^2 + \mathcal{G}^2}} \cot \left(s \sqrt{-\mathcal{F} + \sqrt{\mathcal{F}^2 + \mathcal{G}^2}} \right) \left. \right], \end{aligned} \quad (52)$$

where the Lorentz invariants are defined as

$$\mathcal{F} := -\frac{1}{4}F_{\mu\nu}F_{\mu\nu} = \frac{1}{2}(\vec{B}^2 - \vec{E}^2) \quad \text{and} \quad \mathcal{G} := -\frac{i}{4}F_{\mu\nu}\tilde{F}_{\mu\nu} = \vec{E} \cdot \vec{B}. \quad (53)$$

Those expressions are very clumsy, so we consider a few special cases. As discussed in Section 2.1, our $N_f = 1$ model does not make sense unless $\mathcal{G} = 0$ due to the $U(1)_A$ anomaly. The case with $\mathcal{G} \neq 0$ is of interest when $N_f > 1$, but in what follows, we concentrate on the non-anomalous case.

At zero temperature, the Lorentz invariance should be recovered and we expect the expression for the effective potential becomes considerably simple. In fact, we can go back to Equation (48) and simply set $n = 0$.⁴ We then have

$$\hat{V}(m) = -\frac{N_c}{8\pi^2} \int_0^\infty ds s^{-3} e^{-m^2 s} \{s\sqrt{2\mathcal{F}} \coth(s\sqrt{2\mathcal{F}})\}. \quad (54)$$

From this, we see that for the cases with $|\vec{B}| > |\vec{E}|$ and $|\vec{B}| < |\vec{E}|$, the system behaves as if there is only B -field and E -field, respectively. Also as is well-known, the pure E -field case can be obtained from the pure B -field case just by sending $B \rightarrow iE$, and *vice versa*.

When we turn on the temperature, all those features are lost. Examining Equation (52), one sees that the response of the system for the cases $|\vec{B}| \leq |\vec{E}|$ is not as simple as the zero temperature case. Moreover, the pure B and E background systems are not related through $B \rightarrow iE$. These are all due to the lack of the Lorentz invariance at finite temperature. Because of this complexity, we find it best to handle the finite temperature system with only B and E fields separately.

2.5.1 Pure B Background

We have for this case

$$\{\det_L[(Fs) \cot(Fs)]\}^{1/2} \rightarrow s|\vec{B}| \coth(s|\vec{B}|) \quad \text{and} \quad \{(Fs) \cot(Fs)\}_{00} \rightarrow 1, \quad (55)$$

which lead to the expression of the effective potential

$$V_{\text{eff}}(m) = \frac{1}{2}\vec{B}^2 + \frac{1}{2}N_c\Lambda^2 g^{-2}m^2 + \frac{N_c T}{4\pi^{3/2}} \int_0^\infty ds s^{-5/2} \{s|\vec{B}| \coth(s|\vec{B}|)\} \\ \times \sum_{l \in \mathbb{Z}_{1/2}} \exp[-s\{(2\pi Tl - i\mu)^2 + m^2\}]. \quad (56)$$

First, notice that the first term on the right-hand side is N_c -suppressed, therefore, we drop this term from now on. Next, observe that the s integral is ill-defined at $s = 0$ and we regulate this by introducing the proper time cutoff $s = 1/\Lambda^2$ for the lower bound of the integral.⁵ (Up to this point, the scale Λ has been an arbitrary momentum scale but now it

⁴ At zero temperature, the dependence on the chemical potential drops out, as the time direction is noncompact, and introduction of the chemical potential at zero temperature requires the standard method mentioned previously. We will generally consider the zero temperature case without chemical potential.

⁵ Reference [21] assumes that the cutoff Λ can depend on the parameter m . This assumption requires another equation, in addition to the tadpole condition (26). For this, they derive a consistency condition, which corresponds to Equation (18) in our path-integral treatment of Section 2.2. However, the large N_c makes the classical path totally dominant in the path integration as discussed around Equation (23). This results in the fact that the effective action is independent of the source J and the relation (18) gives nothing other than the tadpole condition (26), still lacking an equation that determines the function $\Lambda(m)$. It seems that the consistency condition of Reference [21] comes out of the lack of the proper change of variable *via* the Legendre transformation, in order to obtain the energy of the system.

is taken to be the proptime cutoff scale.) We would like to measure all the quantities in the units of the cutoff scale Λ . This means that we rescale all the dimensionful parameters with Λ , for instance, $s \rightarrow s\Lambda^2$ and $B \rightarrow B/\Lambda^2$. Then defining the dimensionless quantity \hat{V}_{eff} , we have

$$\begin{aligned} \hat{V}_{\text{eff}}(m) &:= \frac{V_{\text{eff}}(m)}{N_c \Lambda^4} \\ &= \frac{m^2}{2g^2} + \frac{|\vec{B}|T}{4\pi^{3/2}} \int_1^\infty ds s^{-3/2} \coth(s|\vec{B}|) \sum_{l \in \mathbb{Z}_{1/2}} \exp[-s\{(2\pi Tl - i\mu)^2 + m^2\}], \end{aligned} \quad (57)$$

where all the parameters are now dimensionless.

Though we have regulated the lower end of the s integral, it is finite at the upper end, only when

$$\text{Re}[(2\pi Tl - i\mu)^2 + m^2] = (2\pi Tl)^2 - \mu^2 + m^2 > 0. \quad (58)$$

This condition crucially depends on the value of the chemical potential. It is well-known that the chemical potential of free (complex) scalar field theory may not exceed the mass of the particle, because the chemical potential effectively acts as a negative mass squared. One might naively think that the similar situation is occurring in our theory when the chemical potential is too large. However, this is false. We must recall that we have been adopting the analytically continued ‘‘imaginary proptime’’ in Equation (29). We have just found that this analytic continuation is appropriate only when the condition (58) is met. If we consider Equation (29) as the continuation to the *positive* imaginary axis, there is nothing that prevents us to continue to the *negative* imaginary axis to make the proptime integral well-defined. In other words, when the condition (58) is violated, we must analytically continue to negative s .

This is the idea of treating the case with a large chemical potential, but there are complications due to the existence of the cutoff, the cut in the complex s -plane from the factor of $s^{-3/2}$ and the poles from the hyperbolic cotangent along the imaginary s -axis. We work out the details in Appendix C. The result is

$$\begin{aligned} \hat{V}_{\text{eff}} &= \\ &\frac{m^2}{2g^2} + \frac{T}{2\pi^{3/2}} \text{Re} \left[\int_1^\infty ds (sB) \coth(sB) s^{-5/2} \sum_{l > \bar{l}} \exp[-s\{(2\pi Tl - i\mu)^2 + m^2\}] \right. \\ &+ i \int_1^\infty ds (sB) \coth(sB) s^{-5/2} \sum_{l=1/2}^{\bar{l}} \exp[s\{(2\pi Tl - i\mu)^2 + m^2\}] \\ &+ i \int_0^\pi d\phi (e^{i\phi} B) \coth(e^{i\phi} B) e^{-\frac{3}{2}i\phi} \sum_{l=1/2}^{\bar{l}} \exp[-e^{i\phi}\{(2\pi Tl - i\mu)^2 + m^2\}] \\ &\left. + (2\pi i) \sum_{l=1/2}^{\bar{l}} \sum_{k=1}^\infty e^{-\frac{3}{4}\pi i} \left(\frac{B}{k\pi}\right)^{3/2} \exp[-ik\frac{\pi}{B}\{(2\pi Tl - i\mu)^2 + m^2\}] \right], \end{aligned} \quad (59)$$

where $B := |\vec{B}|$ and we have the condition $B < \pi$, indicating that B may not exceed the cutoff scale squared Λ^2 too much. The parameter \bar{l} is defined to be

$$\bar{l} := [(2\pi T)^{-1} \theta(\mu - m) \sqrt{\mu^2 - m^2}]_G, \quad (60)$$

where without loss of generality μ and m are assumed to be greater than or equal to zero, $\theta(x)$ is the Heaviside theta and the symbol $[x]_G$ is the half-integer version of the Gauss symbol, *i.e.*, it is the largest half integer less than or equal to x . Obtaining Equation (59) involves contour integrations, and referring to Figure 42, the first line is the contribution from the positive horizontal axis, the second line is from the negative horizontal axis, third one is from the small circular contour (coming from the existence of the cutoff) and the last term is the contribution from the poles mentioned above. One can see that the last term is oscillatory and we will see that this part gives rise to the well-known de Haas-van Alphen effect [17] and it complicates the phase structure.

The effective potential obtained above contains all the necessary information and is ready for the numerical evaluation. Regarding \hat{V}_{eff} as a function of m^2 , the tadpole condition (26) becomes

$$0 = \frac{d\hat{V}_{\text{eff}}}{d\sigma_{\text{cl}}} = \frac{d(m^2)}{d\sigma_{\text{cl}}} \frac{d\hat{V}_{\text{eff}}}{d(m^2)} = 2g^2\sigma_{\text{cl}} \frac{d\hat{V}_{\text{eff}}}{d(m^2)}, \quad (61)$$

where we used the definition (28). We denote the solution to the tadpole condition by m^* . We see that $m^* = 0$ is always a solution and the solution other than this satisfy

$$\left. \frac{d\hat{V}_{\text{eff}}}{d(m^2)} \right|_{m=m^*} = 0. \quad (62)$$

When there are more than one solution, energetically preferred one must be chosen by consulting with \hat{V}_{eff} . In this way, we can determine the dynamical mass and the phase structure of the theory.

2.5.2 Pure E Background

We have for this case

$$\begin{aligned} \{\det_L[(Fs)\cot(Fs)]\}^{1/2} &\rightarrow s|\vec{E}| |\cot(s|\vec{E}|)| \\ \{(Fs)\cot(Fs)\}_{00} &\rightarrow s|\vec{E}| \cot(s|\vec{E}|), \end{aligned} \quad (63)$$

which lead to the expression of the effective potential

$$\begin{aligned} \hat{V}_{\text{eff}}(m) &= \frac{m^2}{2g^2} + \frac{T}{4\pi^{3/2}} \int_1^\infty ds s^{-5/2} \sqrt{sE \cot(sE)} \\ &\times \sum_{l \in \mathbb{Z}_{1/2}} \exp[-s\{(sE \cot(sE))^{-1}(2\pi Tl - i\mu)^2 + m^2\}], \end{aligned} \quad (64)$$

where as in the previous subsection, \hat{V}_{eff} and all the parameters are made dimensionless with respect to the cutoff Λ and we redefined $E := |\vec{E}|$. Because of the cotangent in the exponent, we have essential singularities and this makes the examination of this case notoriously difficult. In the following, we make two attempts: $T \rightarrow 0$ limit and weak E -field expansion.

Zero Temperature

In the zero temperature limit, instead of summing over l , we should *integrate* Equation (64) with respect to the combination l . This yields

$$\hat{V}_{\text{eff}} = \frac{m^2}{2g^2} + \frac{1}{8\pi^2} \int_1^\infty ds s^{-3} \{(sE) \cot(sE)\} e^{-m^2 s}. \quad (65)$$

As noted in the footnote near Equation (54), the chemical potential drops out and we consider the system without it. We find that only the simple poles of the cotangent are present. Thus, it is commonly evaluated through the convention

$$\cot(sE) \rightarrow \text{P. V.} \cot(sE) + \frac{i\pi}{E} \sum_{n=1}^{\infty} \delta(s - \pi n/E), \quad (66)$$

where P.V. denotes the principal value.

The principal value gives the real part of the effective potential and this has been evaluated in the literature. We quote the result from Reference [21],

$$\text{Re} [\hat{V}_{\text{eff}}] = \frac{m^2}{2g^2} + \frac{1}{8\pi^2} \left\{ \text{Re}[Q] - a_E + E_3(m^2) - \frac{1}{3} E^2 E_1(m^2) \right\}, \quad (67)$$

where

$$Q := m^4 \left\{ -\frac{1}{4} - \frac{1}{3} \left(\frac{E}{m^2} \right)^2 + \frac{1}{2} \left(1 - \frac{1}{z} + \frac{1}{6z^2} \right) \ln z - \frac{1}{z^2} \partial_x \zeta(x, z) \Big|_{x=-1} \right\}, \quad (68)$$

with $z := im^2/(2E)$,

$$a_E := \int_0^1 ds s^{-3} e^{-m^2 s} \{(sE) \cot(sE) - 1 + (sE)^2/3\}, \quad (69)$$

and the functions $E_n(x)$ are the exponential integrals defined as

$$E_n(x) := \int_1^\infty \frac{dt}{t^n} e^{-xt}. \quad (70)$$

Using the real part of the effective potential, Klevansky and Lemmer [21] examines the dynamical mass and the phase structure of the system under the stress of the constant electric field. (We will reproduce their results in the next subsection.)

The second term in the replacement (66) yields the imaginary part of the effective potential

$$\text{Im} [\hat{V}_{\text{eff}}] = \frac{1}{8\pi} \sum_{n=1}^{\infty} \left(\frac{E}{n\pi} \right)^2 e^{-\frac{n\pi}{E} m^2}. \quad (71)$$

The imaginary part is interpreted as the pair creation rate of the quarks in Reference [15]. The pair creation inevitably implies the instability of the groundstate and in our system, this occurs at any finite value of E . Therefore, the conclusions about the mass and the phase structure drawn from the real part may not have any physical significance. However, as long as the imaginary part is small compared to the real part, we can assume that the

instability sets in slowly, compared to the dynamical mass m^* , and we can still obtain the physical insights. In the numerical evaluation, therefore, we will simultaneously examine the real and the imaginary parts of the effective potential.

Weak E-Field Expansion

We attempt to circumvent the essential singularities in Equation (64) by expanding in small E . This, of course, is a very dangerous thing to do. However, we extract some qualitative conclusions by comparing it to the zero temperature case and also we check if the higher order terms in the expansion give less contributions to the effective potential.

The expansion itself is straightforward and we have

$$\begin{aligned} \hat{V}_{\text{eff}}(m) &= \frac{m^2}{2g^2} + \frac{T}{4\pi^{3/2}} \int_1^\infty ds s^{-5/2} \sum_{l \in \mathbb{Z}_{1/2}} \exp[-s\{(2\pi Tl - i\mu)^2 + m^2\}] \\ &\quad - \frac{E^2 T}{24\pi^{3/2}} \int_1^\infty ds s^{-1/2} \sum_{l \in \mathbb{Z}_{1/2}} \{1 + 2s(2\pi Tl - i\mu)^2\} \exp[-s\{(2\pi Tl - i\mu)^2 + m^2\}] \\ &\quad + \mathcal{O}(E^4). \end{aligned} \tag{72}$$

One can easily go up to higher orders as desired. We must evaluate the sum and the integral term by term in the expansion as in Appendix C. However, assuming that the parameter $|l|$ is large enough to satisfy the convergence condition (58), one can carry out the integral before the sum and obtain a closed form. As discussed in the appendix, one can then analytically continue the integral beyond the validity range of the parameter l to the whole half integers and this considerably eases the practical evaluation.⁶ Thus in practice, one should exchange the order of the integral and the sum in Equation (72), without worrying about the convergence condition (58).⁷

2.6 Numerical Evaluation

We are interested in the dynamical mass m^* and the effective potential V_{eff} in the five-dimensional parameter space (T, μ, B, E, g) . It is, of course, not practical to cover entire space at once, so we examine slices of the parameter space. As a warm up and to illustrate the general behavior of the NJL model, we first investigate the slice of $B = 0 = E$. We then turn on those parameters one at a time.

2.6.1 General Observation without Electromagnetic Fields

We learn in this section that the temperature and the chemical potential both behave as the “destabilizer” of the quark boundstate, and that when the condition (58) is violated and the analytic continuation is required, the effective potential shows more complicated behavior than when the condition is satisfied. Those are the generic properties of the model and remain essentially the same when we turn on the external electromagnetic fields.

⁶ For the pure B background, we have not been able to obtain the closed form of the s integral, so needed to evaluate the very complicated expression in Equation (59).

⁷ Also it is practically convenient to realize that the negative l is exactly the complex conjugate of the positive counterpart.

The tadpole condition (26) for this case can be written as

$$\frac{\pi^{3/2}}{g^2} = T \operatorname{Re} \left[\sum_{l>0} \int_1^\infty ds s^{-3/2} \exp \left[-s \{ (2\pi T l - i\mu)^2 + m^{*2} \} \right] \right]. \quad (73)$$

We have indicated that the integral should be done before the sum. This is because the integral for this case is simple enough to yield a closed form, and as discussed in Appendix C and Section 2.5.2, we can then analytically continue the integral to the values of l that violates the condition (58).

We first plot the right-hand side of the tadpole condition (73) in Figure 3. These plots

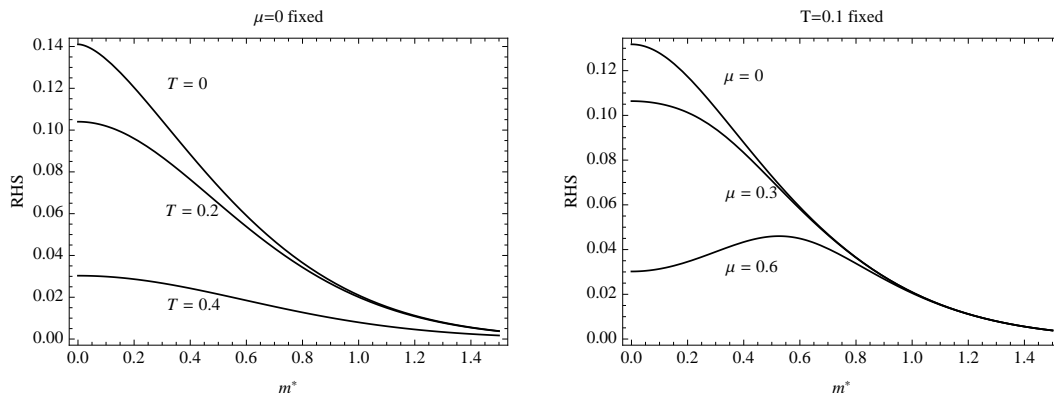


Figure 3: The right-hand side of Equation (73), *i.e.*, $\pi^{3/2}/g^2$, against m^* . For $T = 0 = \mu$ the value of RHS at $m^* = 0$ is $1/4\pi^{1/2} \approx 0.141$ and this corresponds to the famous critical coupling $g_c = 2\pi$. Note the different behavior appearing for $(\pi T)^2 - \mu^2 < 0$, which is the case for $T = 0.1$ and $\mu = 0.6$. In this case, there can be two solutions with $m^* \neq 0$.

show that there is a critical value of the coupling g , below which the solution to the equation does not exist (and the only solution to the tadpole condition is $m^* = 0$), and the system is in the chirally symmetric phase. The critical coupling is plotted against the temperature in Figure 4. In particular, the critical coupling for $T = 0 = \mu$ is the famous $g_c = 2\pi$

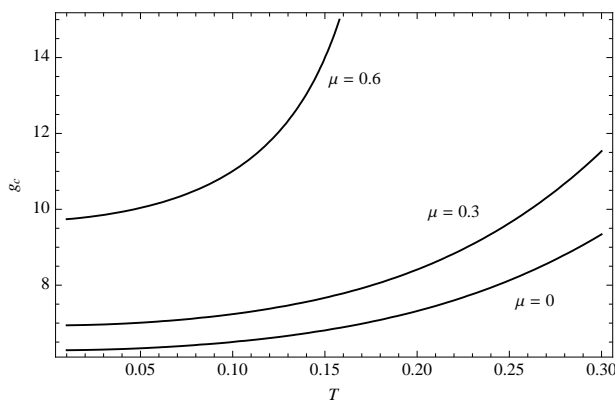


Figure 4: The critical coupling g_c is defined to be the value, below which the solution to the tadpole condition does not exist. Note that for small T and large μ , $g = g_c$ does not imply $m^* = 0$, as shown in the right panel of Figure 3. The plots show that the larger T and μ require the larger coupling.

$(\pi^{3/2}/g_c^2 \approx 0.141)$ of the original work [1]. We observe that both the temperature and chemical potential tend to destroy the quark boundstate, as these parameters necessitate stronger coupling.

In the right panel of Figure 3, we notice the difference between the low and high values of the chemical potential. For the parameters given in the diagram, we have $(\pi T)^2 - \mu^2 > 0$ for $(T, \mu) = (0.1, 0.3)$ and negative for $(0.1, 0.6)$. Thus, when the chemical potential is large enough (and the temperature is low enough) to require the analytic continuation, the system respond in a more complicated way and in particular, there can be multiple solutions to the tadpole condition for a given value of the coupling. One manifestation of such complication is the order of the chiral phase transition. In Figure 5, the effective potentials are plotted against the parameter m for the low T , high μ region and for the high T , low μ . The reference point of the potential is taken to be the value at $m = 0$, which is

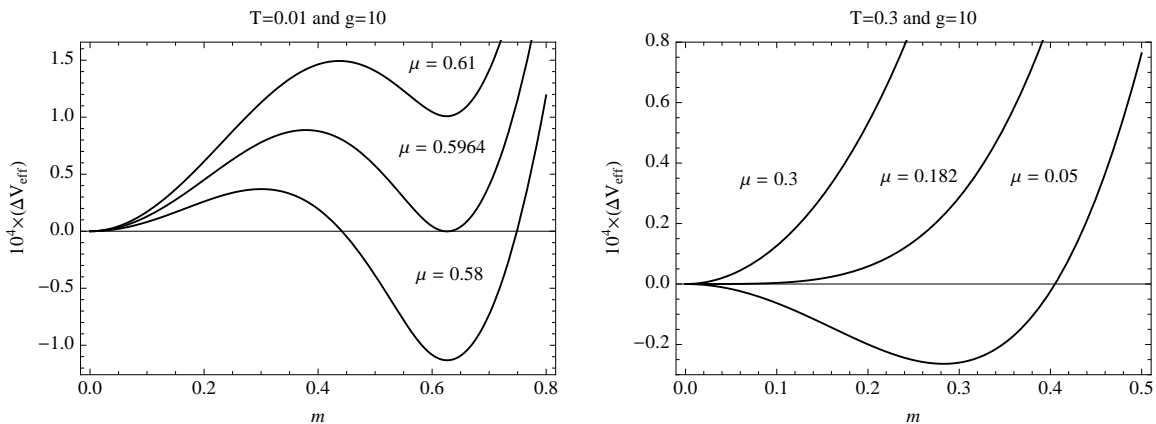


Figure 5: The plot of $\Delta V_{\text{eff}} := V_{\text{eff}}(m) - V_{\text{eff}}(0)$. The left panel shows the first order phase transition with respect to the chemical potential in the low T , high μ region and the right panel shows the second order transition in the high T , low μ region.

always a minimum, and this base value defines the difference potential ΔV_{eff} . Notice that the low T , high μ diagram on the left has a large range of m where $(\pi T)^2 - \mu^2 + m^2 < 0$, and this leads to the extra structure, the potential barrier, that causes the first order chiral phase transition. Meanwhile, the high T , low μ diagram of the right panel has $(\pi T)^2 - \mu^2 > 0$ for all the values of μ plotted. For this case, the analytic continuation does not occur and V_{eff} is relatively simple, leading to the second order phase transition. The complication due to the analytic continuation discussed briefly here is the generic phenomenon and we will see the further consequences in the next subsection.

Finally in the absence of the electromagnetic background, we show the response of m^* with respect to the coupling g in Figure 6. As expected, the dynamical mass generally increases with the coupling. Diagram (b) zooms into the near critical coupling g_c , and shows the relation $m^* \sim \sqrt{g}$ in this region. This response of the dynamical mass with respect to g will be contrasted to the dynamical mass of the SS model with respect to the probe brane separation L .

2.6.2 Pure B Background

We now turn on the B field (and $E = 0$) and the effective potential for this case is given in Equation (59).

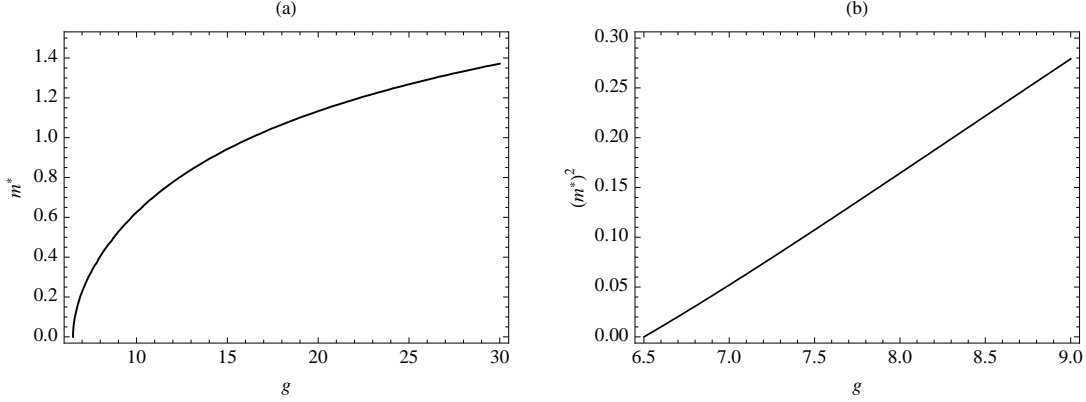


Figure 6: These are plotted for $T = 0.1$ and $\mu = 0$. Diagram (b) is m^{*2} against the region of g near the critical value and shows the relation $m^* \sim \sqrt{g}$. The linear behavior of (b) fails in the larger values of g . The graph for $T = 0$ is nearly identical, except that the critical value is $g_c = 2\pi$ and the graph is slightly shifted to the left.

The salient feature of this effective potential is the last term in the equation, the oscillation term. When the condition (58) is violated, this term comes in effect, leading to the oscillatory behavior of the effective potential with respect to the various parameters.

Figure 7 is the plot of the effective potential with respect to the parameter B and the other parameters fixed. We clearly see the oscillation, known as the de Haas-van Alphen effect, and this is caused by the crossings of the fermi sphere through the Landau levels. This effect leads to the multiple solutions to the tadpole condition (26) and complicates the model in the low T , high μ region of the parameter space.

From Equation (59), it is easy to work out the tadpole condition (26) and it can be written in the form $\pi^{3/2}/g^2 = \text{RHS}$, similar to Equation (73). The right-hand side (RHS) is plotted for various parameters in Figure 8. The plots of the left panel show the behavior of RHS similar to Figure 3 without the B field. One important difference, though, is the case with $T = 0$ where the presence of the B field makes the critical coupling 0, *i.e.*, the magnetic field stabilizes the quark boundstate and any finite coupling breaks the chiral symmetry. For this reason, the magnetic field is sometimes called the “catalysis” of the chiral symmetry breaking [19]. However, even with the B field, any finite temperature brings the critical coupling nonzero. Figure 9 shows the plots of critical coupling against the magnetic field at $\mu = 0$. In the figure, we see the competing effects of B as the stabilizer and T as the destabilizer of the quark boundstate.

Now, the right panel of Figure 8 is plotted for the parameters that satisfy $(\pi T)^2 - \mu^2 + m^{*2} < 0$ for $m^* < 0.5$. We can observe the effect of the oscillation, and for a certain range of the coupling and B (*e.g.*, $B = 0.1$ and $\pi^{3/2}/g^2 \approx 0.07$ at $g^2 = 80$), there are four $m^* \neq 0$ solutions to the tadpole condition. We must consult with the effective potential to decide which solution is the stable and energetically preferred one. Figure 10 is the plot of the potential. We indeed observe four peaks and troughs. The top plot is at the critical value of the chemical potential and above this value, the mass sharply drops to zero and the system goes through the chiral phase transition to the symmetric phase. Curiously, the bottom two curves show that there is another first order phase transition that is different from the chiral phase transition. During this transition, the mass sharply drops to a lower value but not to zero. This is the extra structure introduced by the oscillation.

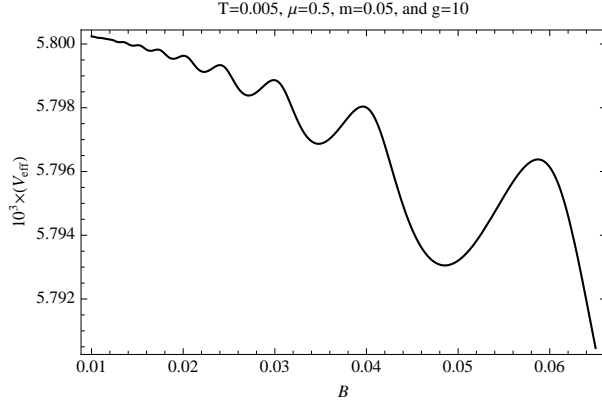


Figure 7: The plot of the effective potential with respect to B , illustrating the de Haas-van Alphen effect.

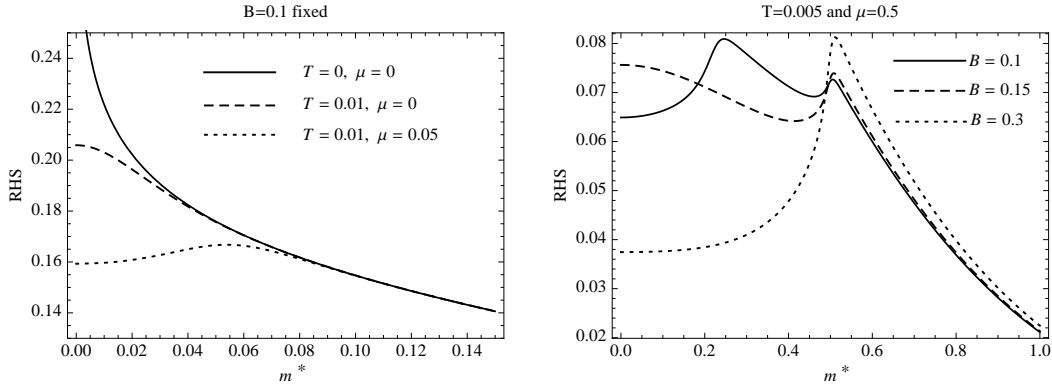


Figure 8: The right-hand side (RHS) of the tadpole condition similar to Equation (73) is plotted as a function of m^* . On the left panel with $T = 0$, the graph blows up to infinity as $m^* \rightarrow 0$, indicating $g_c = 0$. Finite T brings g_c finite. The right panel is plotted for the parameters that satisfy $(\pi T)^2 - \mu^2 + m^{*2} < 0$ for $m^* < 0.5$. Notice the effect of the oscillation that leads to multiple solutions to the tadpole condition for a certain range of g .

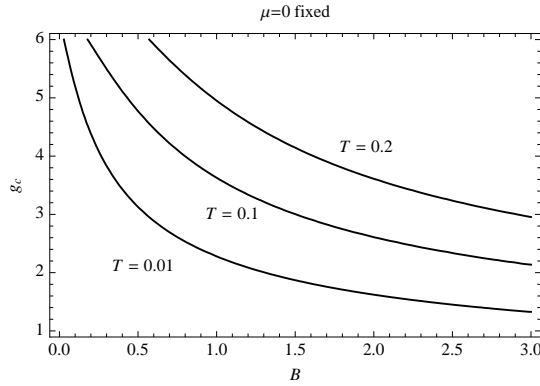


Figure 9: The plots show that the B field is the stabilizer of the boundstate, as it requires smaller value of the coupling at high B , and as discussed previously, the temperature is the destabilizer.

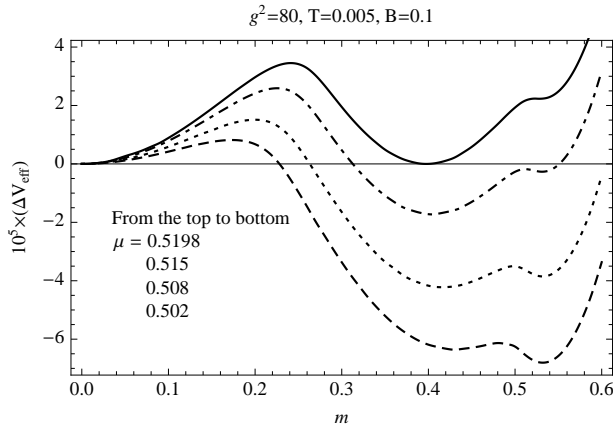


Figure 10: The plot of the effective potential for nonzero B -field and in the low T , high μ region of parameters. In addition to the potential barrier that causes the first order chiral phase transition, we have extra structure due to the de Haas-van Alphen oscillation that causes another first order transition, different from the chiral phase transition (the bottom two plots).

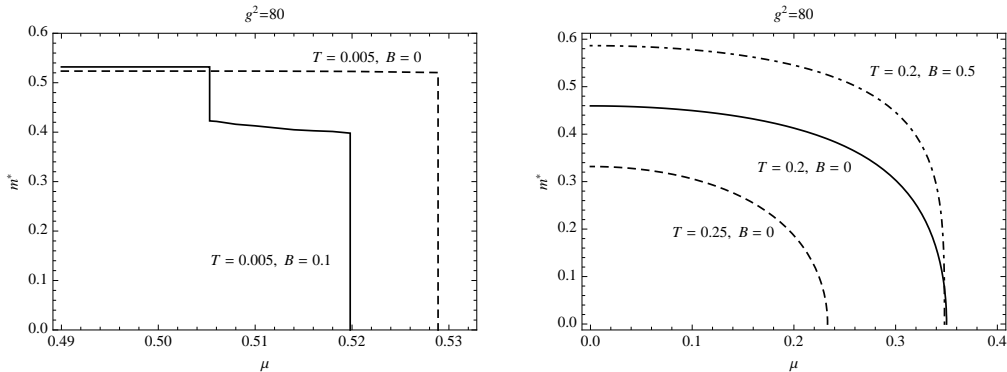


Figure 11: The plot of the dynamical mass against the chemical potential μ . The left panel shows the region of low T , high μ , where the mass goes to zero abruptly, corresponding to the first order phase transition. For the nonzero B -field, we have an additional structure due to the de Haas-van Alphen oscillation and the system goes through a sequence of first order phase transitions. The right panel shows the region of high T , low μ , where the mass goes to zero smoothly as the chemical potential is increased. This corresponds to the second order chiral phase transition.

Figure 11 of the μ - m^* graphs clearly summarize the discussions made so far. On the left, the graph in the solid line directly corresponds to the behavior of the effective potential shown in Figure 10 and reveals the existence of the two first order phase transitions. In the same diagram, the dashed graph is plotted for $B = 0$, indicating that there is only one first order chiral phase transition (see the left diagram in Figure 5). Therefore, the extra first order phase transition is visibly due to the de Haas-van Alphen effect at $B \neq 0$.⁸ On the right panel, we have plotted the μ - m^* graph for the higher temperature so that the condition (58) is always satisfied. For this case, the mass smoothly goes down to zero and this is the second order chiral phase transition, similar to the one shown in the right panel

⁸ We remark that the sharp first order phase transitions shown here is slightly different from rather smooth transitions in Reference [20]. The smoothness is most likely due to the higher temperature in their setup.

of Figure 5. Notice also the role of B and T as the stabilizer and destabilizer, respectively.

We now discuss the response of the dynamical mass with respect to the B field. First, Figure 12 shows the simpler case with $\mu = 0$. For this value of the chemical potential,

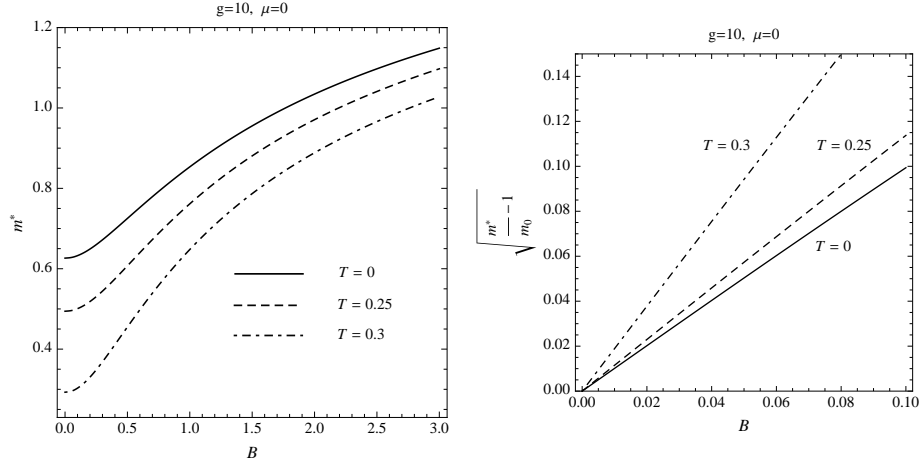


Figure 12: The plot of the dynamical mass with respect to B at $\mu = 0$ fixed. The temperature here is low enough so that the chiral symmetry is broken at $B = 0$. The right panel shows the relation $m^* \sim B^2$ for the region of small B . The parameter m_0 is defined as $m_0 := m^*(B = 0)$.

the mass responds intuitively; it increases monotonically as the external magnetic field (the stabilizer) increases. Notice that for this plot, we have chosen the low enough temperature so that the chiral symmetry is broken even at $B = 0$. The right panel of the figure shows that the mass increases quadratically with respect to B in the region of small B . Also the diagram shows that the tangent of the graphs increases as the temperature is raised.

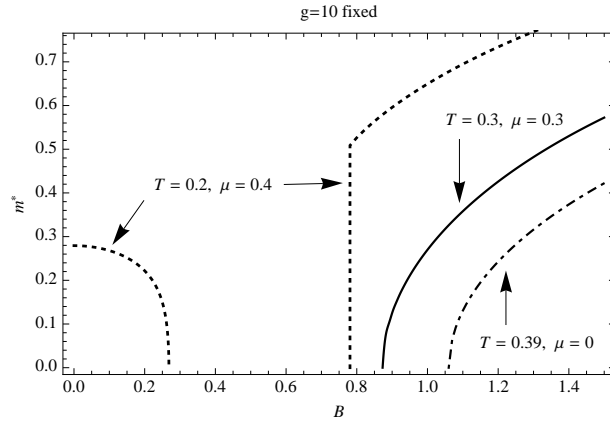


Figure 13: The plot of the dynamical masses with respect to B . For $(T, \mu) = (0.3, 0.3)$ and $(0.39, 0)$, the masses continuously rise from zero as B increases, corresponding to the second order phase transitions. For $(T, \mu) = (0.2, 0.4)$, the mass goes smoothly goes to zero in the region of small B and rises abruptly in the region of large B . They correspond to the second and first order phase transitions (see the left panel of Figure 14). We note that for a certain range of parameters, the left part of the dotted graph can exhibit a sequence of first order phase transitions similar to the one shown in m^* - μ diagram of Figure 11.

The B - m^* graph with nonzero chemical potential is shown in Figure 13. Let us first observe the dotted curves for $T = 0.2$ and $\mu = 0.4$. The response of the mass against B

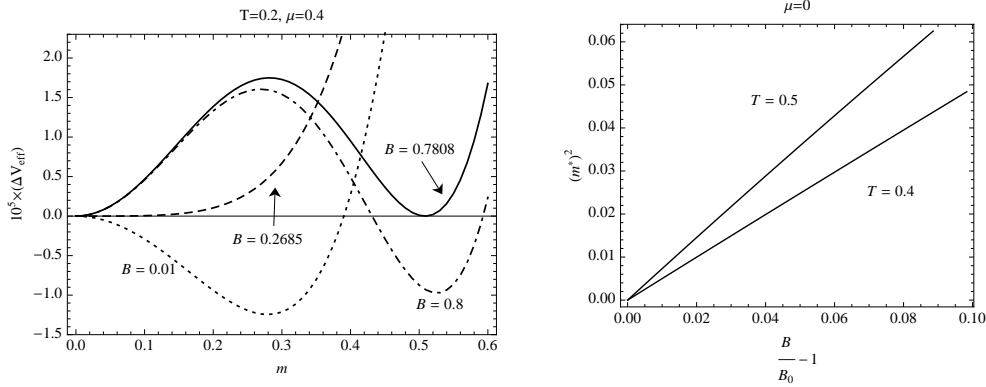


Figure 14: The left panel shows the behavior of the effective potential for $(T, \mu) = (0.2, 0.4)$, exhibiting the first and second order phase transitions (see Figure 13). The right panel is plotted for the high enough temperatures, concentrating on the values near $B = B_0$ of the second order phase transition points. The plots reveal the relation $m^* \sim \sqrt{B}$ near $B = B_0$ and the coefficient increases as temperature goes up.

is highly counter-intuitive for lower B : the mass *decreases* as the magnetic field is dialed up. Moreover, this curve in the low B region can exhibit a sequence of first order phase transitions that are different from the chiral transition, due to the de Haas-van Alphen oscillation. (We have omitted this very complicated graph.) The further increase in the B field leads to the second order chiral phase transition around $B \approx 0.27$. But approximately at 0.78, the system comes back to the broken phase through the first order transition and the mass increases as B is raised. The left panel of Figure 14 shows the series of action in terms of the effective potential.

The complicated behavior here requires a digression. As argued in Reference [19], the stabilizing effect of the B field directly comes from the dominance of the lowest Landau level (LLL). In Figure 12, we have plotted for $\mu = 0$ and the system is always in the LLL, leading to the stabilization effect. When μ is large and T is relatively small, we have a reasonably well-defined fermi sphere (smeared due to the temperature) and the fermi energy can be much larger than the Landau level spacing. If this is the situation of the system, the effect from the LLL is not significant and we do not expect the stabilizing effect of the magnetic field. Even though the finite temperature and the interaction effects prevent the precise estimate here, this in fact is roughly the case for the low B region of the dotted curve in Figure 13. Here we observe that the B field acts as a *destabilizer* of the quark boundstate. As the magnetic field becomes large enough, the Landau level spacing becomes also large and the stabilizing effect from the LLL takes place. To summarize the digression, we can conclude that the oscillation effect and the destabilization effect of B are in general caused by the existence of the fermi sphere and its relation to the Landau levels.

Let us now turn to the other plots in Figure 13. These are the cases where the temperatures are high and the chemical potentials are low enough so that the system is in the symmetric phase in the region of low B . The masses rise continuously from zero at critical values B_{0s} , indicating the second order chiral phase transition, and increases monotonically with B . The right panel of Figure 14 shows that the mass rises from zero as \sqrt{B} and the coefficient increases as the temperature.

The mass depends also on the temperature and the T - m^* diagram is shown in Figure 15. Here we see that as long as $\mu = 0$, or when it is small enough, the mass continuously goes

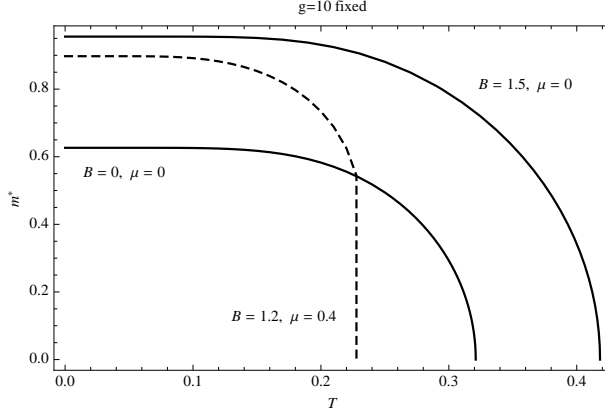


Figure 15: The plot of the dynamical mass as a function of the temperature. We see that the larger values of B lead to the larger mass, *i.e.*, B is the stabilizer. For $\mu = 0$, the mass smoothly becomes zero as the temperature is increased, indicating the second order chiral phase transition. Meanwhile, for $\mu = 0.4$, the mass drops abruptly to zero at a critical temperature, indicating the first order phase transition.

to zero as the temperature is increased, indicating the second order chiral phase transition. We can also observe that the larger the B field is, the larger the mass is, *i.e.*, B acts as the stabilizer of the quark boundstate. When the chemical potential is high, such as $\mu = 0.4$, the first order phase transition occurs, as shown as the dashed curve in the diagram.

We now proceed to discuss the phase diagrams. Though we have seen that there are more than one kind of phase transition, here, we focus on the chiral phase diagrams.

The B - T phase diagram is shown in Figure 16. The top two curves for $\mu = 0$ and 0.3

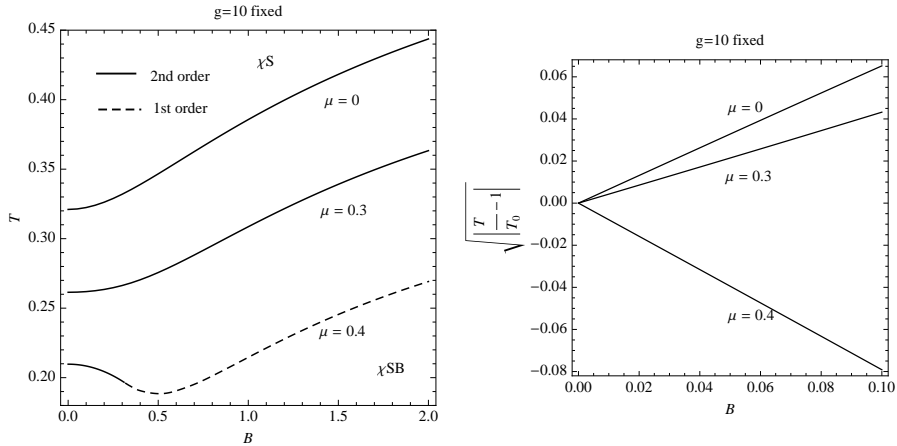


Figure 16: The B - T chiral phase diagram. The upper temperature regions are the chiral symmetric phase. The dotted curve shown on the left panel indicates the first order phase transition and the solid ones are second order. The right panel plots the small B region against $(|T/T_0 - 1|)^{1/2}$ where T_0 is the phase transition temperature at $B = 0$, showing the relation $T \sim \pm B^2$.

shape in expected way as T being the destabilizer and B as the stabilizer. However, the small B region of the bottom curve for the large chemical potential $\mu = 0.4$ is rather surprising. The critical temperature *decreases* as B is increased, indicating that the magnetic field is acting as the *destabilizer* in that region of B . When B is further dialed up, the first order

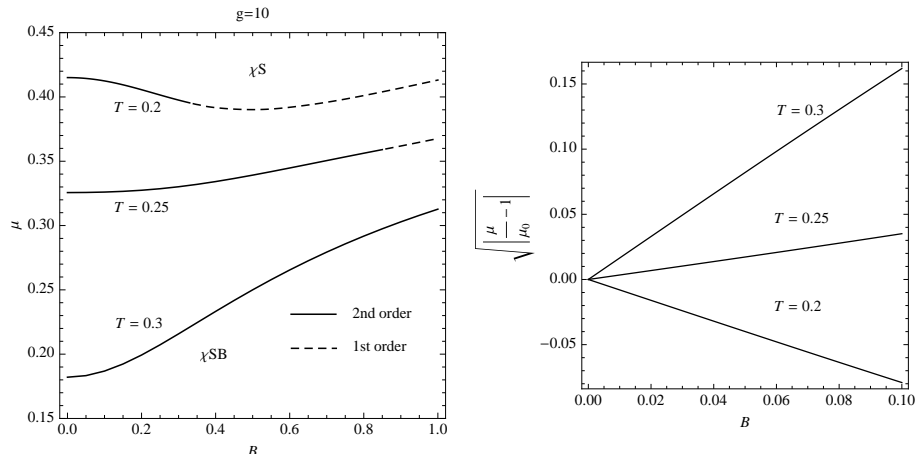


Figure 17: The B - μ phase diagram. For sufficiently large B , the transition becomes first order. The right panel is plotted for the small- B region. The parameter μ_0 is the critical value of μ when $B = 0$.

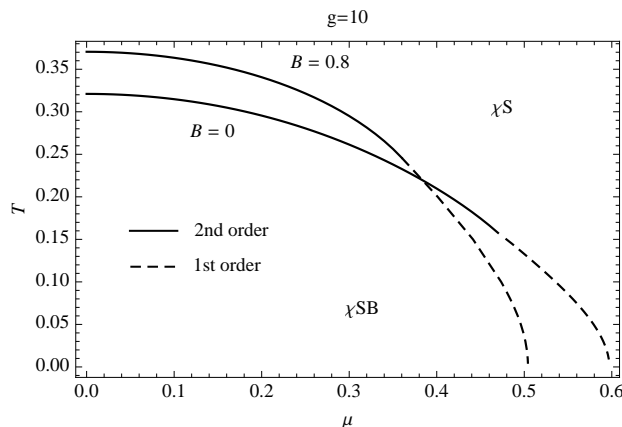


Figure 18: The μ - T phase diagram. In the low temperature region, the order of the transition becomes first order. It is counter-intuitive that the critical value of the chemical potential in the low temperature region is smaller for large value of B , and this is due to the suppression of the LLL effect.

transition is triggered and then B starts acting as the stabilizer. We have seen the similar phenomenon when we discussed the B - m^* diagram of Figure 13 and noted that this is caused by the existence of the fermi sphere and the small Landau level spacing. This effect, in the B - T diagram, appears as the “dent” in the chiral phase transition curve. The right diagram of Figure 16 zooms into the region of small B and shows the relation $T \sim \pm B^2$. Note that the slopes of the plots decrease as the chemical potential increases.

The “dent” observed in the B - T phase diagram can also be observed in the B - μ phase diagram of Figure 17. This phase diagram appears to be similar to the B - T graph, because as we recall, μ acts as the destabilizer of the boundstate just as T does. The right panel also shows the relation $\mu \sim \pm B^2$ in the region of small B and the slopes of the plots increase as the temperature increases.

Let us look into the B - μ phase diagram a little further. When the temperature is high, say, $T = 0.3$, we have the relation of the critical values of the chemical potential, $\mu_c(B = 0) < \mu_c(B = 0.8)$. In the low temperature regime, say, $T = 0.2$, we have $\mu_c(B =$

$0) > \mu_c(B = 0.8)$. This implies that the μ - T phase diagram, plotted for $B = 0$ and 0.8 must cross somewhere between $0.2 < T < 0.3$, that is, the peculiar phenomenon due to the fermi sphere must appear as a “cross” in the μ - T phase diagram. Indeed, the “cross” is observed in the μ - T phase diagram shown in Figure 18. In the low temperature region, we observe that the critical chemical potential for the lower B is *higher* and the higher B in this region of temperature is giving smaller critical μ . This counters the intuition that B and μ are the stabilizer and the destabilizer of the quark boundstate, respectively. So we learn that when the LLL is not dominant due to the fermi sphere, this intuition is false.

2.6.3 Pure E Background

In this subsection, we examine the constant electric field background. As remarked in Section 2.5.2, the essential singularities in the effective potential (64) prevent us from evaluating this as it appears. Therefore, we resorted to two approaches, one is the zero temperature limit and the other is the weak E expansion. We discuss those in turn.

Zero Temperature

The effective potential of this case (without the chemical potential) is given in Equation (65) and we recall that this is always complex for any $E \neq 0$. The general idea is that we extract the dynamical mass from the real part of the effective potential (67) and check if the imaginary part (71) is not too large compared to the real part.

It is straightforward to obtain the tadpole condition (26) for the real part of the effective potential (67) and numerically solve for the dynamical mass m^* for a given E . The result is presented in Figure 19 for $g = 10$ and 20 . The diagram indicates that the E field,

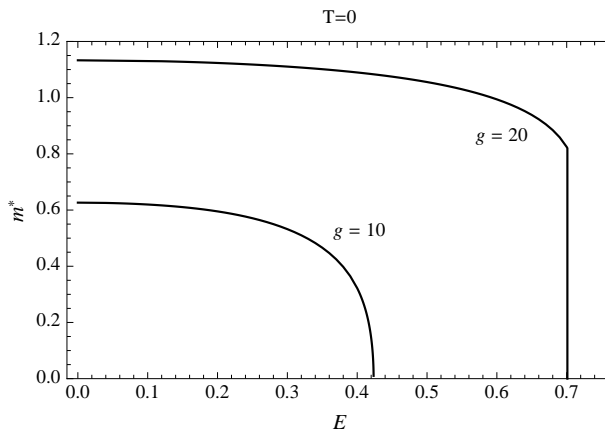


Figure 19: The plot of the dynamical mass with respect to the E field at $T = 0$. For the coupling $g = 10$ and 20 , we have the second and first order phase transitions, respectively.

in general, acts as the destabilizer of the quark boundstate, just as the temperature and the chemical potential (*c.f.*, the pure B background T - m^* diagram of Figure 15 and μ - m^* diagram of Figure 11). When the coupling is not too large (but above the critical coupling g_c which is finite), the mass continuously goes down to zero, indicating the second order phase transition. This second order phase transition was discovered in Reference [21].

What has not been noticed is the existence of the first order phase transition at a large coupling constant, as shown in the figure for $g = 20$. The behavior of the effective potential

is very similar to that of Figure 5, where the role of the chemical potential in that figure is replaced with the E field (and of course $T = 0$ for the current discussion). For this reason, we can expect the very similar result when we include the chemical potential to this zero temperature system.

We now must check if the results drawn from the real part of the effective potential above have any physical significance, by examining the imaginary part of the potential. Figure 20 shows the on-shell values of the effective potential, that is, it is evaluated at $m = m^*$, with respect to the E field. The figure shows that the real part dominates when the E field is

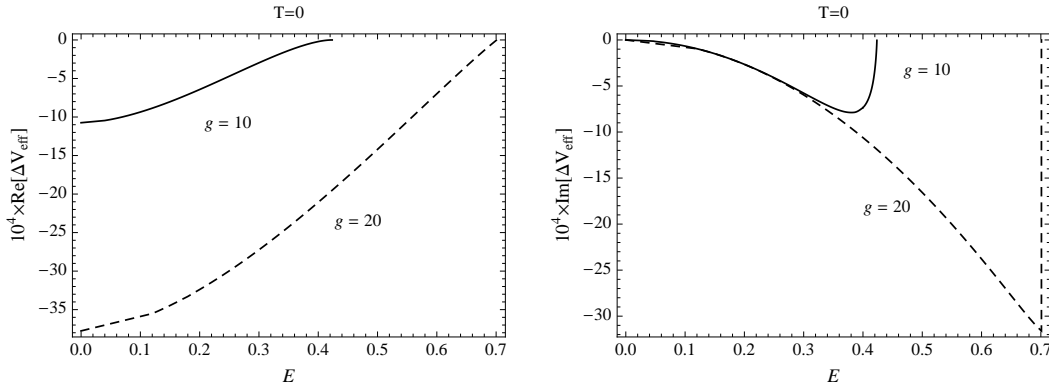


Figure 20: The plots of the real and imaginary parts of the difference action at $T = 0$ and $m = m^*$. The curves terminate at the phase transition point. Near the phase transition points, the imaginary part strongly dominates over the real part.

small and away from the critical value. However, when the electric field is near the critical value, the imaginary part strongly dominates over the real part. This could indicate that the information about the phase transition points is not reliable, due to the breakdown of the stable background by the pair creation.

To obtain further insight into this issue, we recall that Schwinger has worked out the rate of the pair creation in Reference [15] and it is roughly given by $\exp[-\pi m^2/E]$. This means that the results from the real part is reliable when $m^2 \gtrsim E$. Again, this condition is not so well satisfied around the point of the phase transitions. Therefore, though there are good indications of the first and second order phase transitions, it is not safe to conclude so. Most certainly, the values of the critical electric field cannot be trusted.

As in Reference [21], the imaginary part of the effective potential has not been paid much attention, probably due to the NJL model's lack of the confinement. The confinement may fix the problem, but then we are dealing with different model and the conclusions from the real part still does not seem to correspond to the real world. Nonetheless, we have carried out the analysis for both the real and imaginary parts, because we can compare the results to the deconfined phase of the SS model.

Weak E Expansion

We now discuss the weak E expansion of the $T > 0$ effective potential (72). The expansion completely washes out the singularities and the potential is real. One can easily obtain the tadpole condition (26) from the potential (72) and solve numerically for the dynamical mass. Figure 21 shows the result for $g = 10$, $T = 0.3$ and up to $\mathcal{O}(E^6)$. We observe fairly good convergence of the higher terms and the result may be trusted. In particular, the

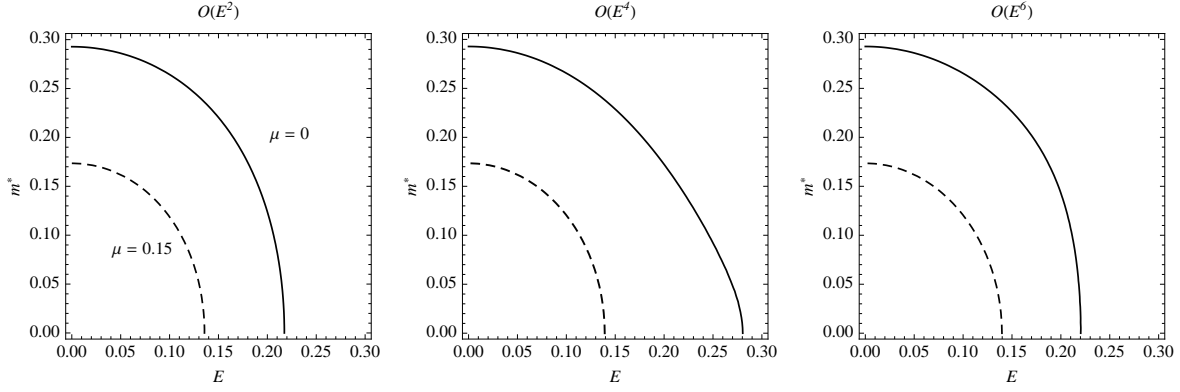


Figure 21: The plot of the dynamical mass against E for $T = 0.3$ and $g = 10$. From the left $\mathcal{O}(E^2)$, $\mathcal{O}(E^4)$ and $\mathcal{O}(E^6)$. They show that the higher order in the weak E expansion is converging. We also observe the general tendency of μ as the destabilizer.

second order phase transition observed at $T = 0$ appears to persist at finite temperature.

It is of interest to see if the first order transition at the zero temperature can also be observed at finite temperature. Figure 22 shows the plot of the effective potential at $g = 20$ and $T = 0.3$. The $\mathcal{O}(E^2)$ effective potential shows the first order phase transition, but the

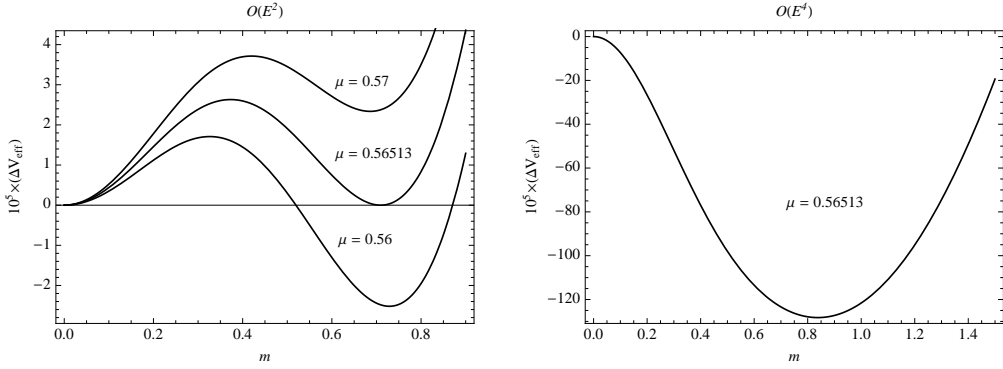


Figure 22: The effective potential at $T = 0.3$ and $g = 20$. The $\mathcal{O}(E^2)$ on the left shows the first order phase transition consistent with the $T = 0$ result, however, the inclusion of the higher order terms [shown on the right is up to $\mathcal{O}(E^4)$] destroys this behavior.

examination of the higher order terms imply that this may not be trusted. On the right panel, the effective potential up to $\mathcal{O}(E^4)$ is shown. We see that the higher order terms are not converging and invalidates the result of $\mathcal{O}(E^2)$. Therefore, we cannot conclude if the first order phase transition at $g = 20$ and $T = 0$ persist in finite temperature.

When the temperature is lower, the convergence of the higher order terms gets worse. In all cases, the potential up to $\mathcal{O}(E^2)$ shows all the expected behavior (as in the previous paragraph), but one finds that the higher order terms are behaving completely unphysical way. We have expanded the $T = 0$ effective potential with respect to small E and found similar defects in the higher order terms, so the expansion at low temperature is not valid. For this reason, we do not attempt to draw the E - T phase diagram.

3 Sakai-Sugimoto Model

We analyze the SS model in this section. We specifically deal with the one-flavor case, but the generalization to more than one flavor is straightforward. We first discuss the general features of the model, including the chiral phase transition and the dynamically generated mass of the model. Then, after setting up the model with external parameters, it is further examined separately for the confined and deconfined phases. Finally we present the results of the numerical evaluation.

3.1 Chiral Phase Transition and Dynamical Mass

The SS model is defined on the IIA background geometry of D4 branes in the near horizon form,

$$\begin{aligned} ds^2 &= (U/R)^{3/2} \{ f_t dX_0^2 + (dX_i)^2 + f_4 (dX_4)^2 \} + (R/U)^{3/2} (f^{-1} dU^2 + U^2 d\Omega_4^2) \\ \Phi &= \Phi_0 + \frac{3}{4} \ln(U/R) \\ C_{(3)} &= -3g_s^{-1} R^3 \sin^3 \theta_1 \sin^2 \theta_2 \cos \theta_3 d\theta_1 \wedge d\theta_2 \wedge d\theta_4, \end{aligned} \quad (74)$$

where $d\Omega_4$ is the metric for the four-sphere with the coordinates θ_i , Φ is the dilaton and $C_{(3)}$ is the RR potential to which the D4-branes couple magnetically. We also have

$$g_s := \exp(\Phi_0), \quad R^3 := \pi g_s N_c l_s^3, \quad (75)$$

and the “blackening factors” are

$$\begin{aligned} f_t = f &= 1 - (U_T/U)^3 \text{ and } f_4 = 1 \text{ for the high temperature deconfined phase} \\ f_4 = f &= 1 - (U_{\text{KK}}/U)^3 \text{ and } f_t = 1 \text{ for the low temperature confined phase.} \end{aligned} \quad (76)$$

The X_4 direction is compactified and at finite temperature, the Euclidean X_0 direction is also compactified as well. To avoid the conical singularity from the compactifications, we must have the circumference of X_4 -direction, β_4 as

$$\beta_4 = \frac{4\pi}{3} \left(\frac{R^3}{U_{\text{KK}}} \right)^{1/2}, \quad (77)$$

in the low temperature confined phase and the circumference of X_0 -direction, β as

$$\beta = \frac{4\pi}{3} \left(\frac{R^3}{U_T} \right)^{1/2}, \quad (78)$$

in the high temperature deconfined phase.

The system with the *non-compact* X_4 direction is of interest as well. In this case, the system is always in the deconfined phase and this allows us to discuss the low temperature behavior of the model in the deconfined phase. In fact, when we discuss the deconfined phase below, we will be cavalier about the confinement/deconfinement critical temperature.

Chiral Phase Transition

The model has the well-known three phases [22] shown in Figure 23. The thin lines in

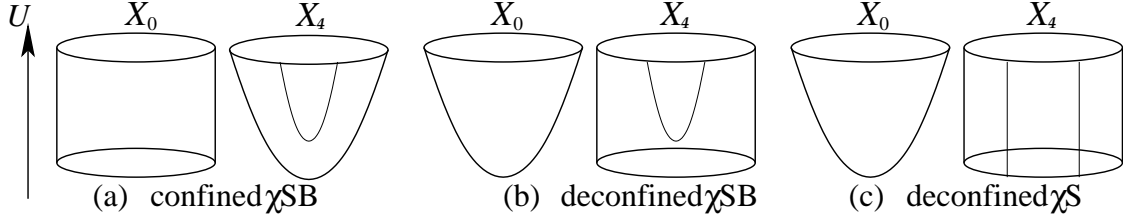


Figure 23: Three phases of the SS model. The coordinate U is the radial coordinate transverse to the D4 branes. The thin lines shown in the X_4 circles represent the probe D8 branes. The diagram (a) represents the low temperature confined phase with broken the chiral symmetry (χ SB), (c) is the high temperature deconfined phase with the restored chiral symmetry (χ S) and (b) is the intermediate deconfined phase with χ SB.

the X_4 circles are the probe D8-branes. The confinement [Diagram (a)] and deconfinement [Diagrams (b,c)] phases are determined only through the D4 background, independent of the probe D8, and the phase transition occurs at $\beta = \beta_4$ [22].

The U-shape configurations of D8 shown in Diagrams (a,b) represent the chiral symmetry breaking in this model. There is a range of temperature and asymptotic separation of the D8 branes, denoted by L , so that the background is in the deconfined phase and the chiral symmetry is broken, as shown in the diagram (b) of Figure 23. Aharony *et al.* [22] have shown that this intermediate phase exists when $L < L_c \approx 0.97(\beta_4/2\pi)$ in the deconfined phase. When $L > L_c$, the intermediate phase does not exist and the chiral phase transition and the confinement/deconfinement phase transition occurs simultaneously. The chiral phase transition in the deconfined phase is determined by comparing the values of the D8 probe action in U- and ||-configurations for a given set of parameters. Since the probe configuration jumps from one to the other at the phase transition point, this is always a first order phase transition.

String Endpoint Mass (SEP)

The model in the U-shape configuration exhibits various spectra which are similar to low energy QCD, such as mesons. For instance, the fluctuations of the embedding map from D8 to the spacetime represent the scalar mesons and the D8 worldvolume gauge fields (of non-zero modes in a certain mode expansion) correspond to the vector mesons. Moreover, the higher spin mesons are described by the spinning open string of the following configuration [23]. The endpoints of the string are both attached to the tip of the U-shaped D8-brane, in the different locations of the field theory directions, and they are rotating around each other in those directions. The body of the string is draped all the way down to the wall and lying there. Figure 24 represents a slice of the string configuration and the field theory directions are coming out of the diagram. The “wall” is the tip of the “ X_4 cigar” in the confined phase and the horizon in the deconfined phase (see Figure 23).

The energy of the string segment in the U direction (the vertical segment in Figure 24) is given by

$$m^* = \frac{1}{2\pi\alpha'} \int_{\bar{U}}^{U_0} \sqrt{g_{00}g_{UU}} dU = \frac{1}{2\pi\alpha'} \int_{\bar{U}}^{U_0} \sqrt{f_t f^{-1}} dU, \quad (79)$$

where $\bar{U} = U_{KK}$ and U_T for the confined and deconfined phases, respectively. It is argued quite generally in Reference [23] that m^* represents the dynamically generated mass of the

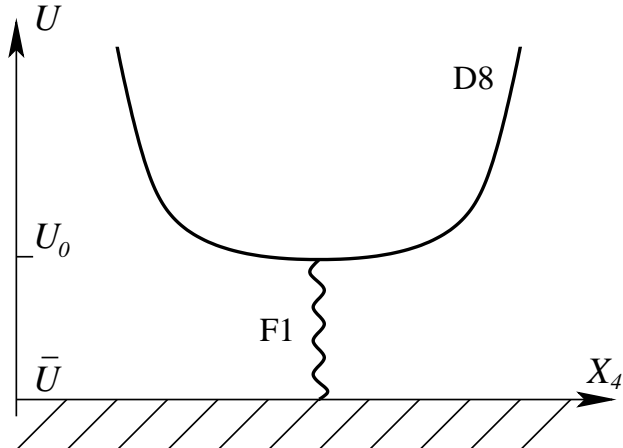


Figure 24: A slice of the string configuration describing the high spin mesons. The location $U = U_0$ is the tip of the U-shaped D8 and $\bar{U} = U_{\text{KK}}$ for the confined phase and $\bar{U} = U_T$ in the deconfined phase. The string is also stretching out of the figure into the field theory directions and coming back up again to the D8 tip.

quarks.⁹ One evidence shown in the reference is that the masses of the massive pseudo-scalar and vector mesons increase monotonically with the energy of the vertical segment and when the vertical part is long enough, the masses increase linearly. Also it is pointed out that the model (without a tachyon potential) is believed to describe a QCD-like system with zero current quark mass, because the pions are massless. This leaves the only candidate, the dynamically generated quark mass. This mass, however, is different from the constituent mass and is called “string endpoint mass (SEP)”.¹⁰ The difference mainly comes from the energy of the string segment that is horizontal to the wall. For this reason, we refer this mass as the dynamical mass or SEP.

One might argue that the meson spectrum and the dynamical mass would not make sense in the deconfined phase. However, we have the fact that the SS model exhibits the chiral phase transition in the deconfined phase, and moreover, there are evidences from the lattice simulations that indicate the existence of the quark boundstate in QCD, significantly above the deconfinement temperature [40]. See Reference [24] for the holographic study of mesons in the deconfined phase.

In what follows, we will be interested in the dynamical mass described here and we examine it for both in the confined and deconfined phases.

3.2 External Parameters

Constant NSNS Field

The aim of this section is to investigate the chiral phase transitions and the dynamical masses under the influence of external parameters, such as temperature. One of the external parameters in which we are interested is the background constant electromagnetic field and

⁹ The arguments made in Reference [23] is especially reliable for a very high spin mass, because the semi-classical treatment of the string is good in this regime. However, the analysis of the Regge trajectory carried out in the reference indicates that the description of the mass is fairly good even for the low spin mesons.

¹⁰ Private communication with J. Sonnenschein.

we would like to introduce this into the SS model. The most natural thing to do is to introduce the background gauge field of diagonal $U(1)_V$ that comes from $U(1) \times U(1)$ of D8 and $\overline{D8}$ probes. This, in fact, behaves exactly like the electromagnetic field for our one-flavor model.¹¹ Now, recall that the gauge invariant quantity in the D-brane action is not the field strength tensor of the gauge field, but the combination of that with the NSNS B -field (B_{NS}), pulled back on the brane with respect to the embedding map of the D-brane. Therefore, we can freely trade the background gauge field to B_{NS} , up to the embedding map and the factor of $2\pi\alpha'$. As we will describe momentarily, we will choose the standard simple embedding map of the D8 brane so that the introduction of the constant background electromagnetic field is equivalent to the constant B_{NS} in the IIA supergravity background. Notice that the constant B_{NS} does not affect the supergravity background.

Let us then consider which components of B_{NS} we should turn on. We are interested in the fields that have direct interpretation in the dual field theory. This implies that we should have at least one component in the field theory direction. We also avoid turning on $(B_{\text{NS}})_{iu}$, because according to the general holographic dictionary, they source the boundary currents in X_i -direction and we do not have such counterpart in the NJL model. [We will discuss the exceptional case $(B_{\text{NS}})_{0U}$ in a moment.] There are interesting possibilities to turn on $(B_{\text{NS}})_{\mu 4}$ and $(B_{\text{NS}})_{4U}$. However, these terms complicates the probe action and more importantly, the field theory interpretation of those quantities are not clear, so in the present work, we will not discuss these possibilities. We are then left with

$$E_i := (B_{\text{NS}})_{0i} \quad \text{and} \quad B_i := \epsilon_{ijk}(B_{\text{NS}})_{jk} , \quad (80)$$

where $\epsilon_{123} = +1$ for the convention and we deal with these background fields in the following.

Before setting out for the further analysis, we must mention the topological constraints imposed on the constant B_{NS} . As can be seen in Figure 23, the SS model possesses the degenerate point in the background geometry, and any constant tensor (of rank > 0) cannot make sense as a field at the degenerate point. This severely restricts the possible constant B_{NS} and the situation is summarized in Table 1, together with the excluded cases for the completeness. In particular, notice that the electric fields E_i are not at all allowed in the

$B_{\text{NS}(A,B)}$	$(0, i)$	$(0, 4)$	$(0, U)$	(i, j)	$(i, 4)$	(i, U)	$(4, U)$
conf.	✓	×	✓	✓	×	✓	×
deconf.	×	×	×	✓	✓	✓	✓

Table 1: The topological constraints on the constant B_{NS} -field. The top row is the components of B_{NS} -field.

deconfined phase. As we will see, the free energy of the system in this case is always imaginary for any nonzero constant electric field and this is precisely due to the violation of the topological constraint. The reader who looked at the previous section for the NJL model would recall the same imaginary behavior in the effective potential. There, we carried out the analysis observing the real and imaginary parts separately. Thus, we do here the same for the sake of the comparison and we assume that the imaginary part has the same physical interpretation as in NJL, namely, the instability due to the pair creation of the quark pair.¹²

¹¹ As remarked in Reference [26], the quarks have different couplings to the electromagnetic field for $N_f > 1$, but even in this case, we should expect that the $U(1)_V$ gauge field acts similar to the real background electromagnetic field.

¹² We do not induce the current *a la* Karch and O'Bannon [41], because we do not have such counterpart in the NJL model. See Reference [26] for the treatment with the current.

Chemical Potential

In addition to the constant electromagnetic field, we include the quark chemical potential and see how the system respond to this. For this, let us consider the $(0, U)$ -component of the B_{NS} field. The AdS/CFT dictionary tells us that this sources the charge density of the boundary theory. Recall that a chemical potential can be thought to be the time-component of the gauge field that minimally couples to the conjugate charge density. Thus, this component of B_{NS} -field should be directly related to the quark chemical potential of our interest. In fact, on the probe D8-brane, this is equivalent to the same component of the field strength tensor, indicating that $(B_{\text{NS}})_{0U}$ is the U -derivative of the chemical potential. The treatment of the chemical potential in Reference [25] actually starts by including the time component of the worldvolume gauge field and we have just argued that this is equivalent to the introduction of $(B_{\text{NS}})_{0U}$. Thus, in addition to the components (80), we include

$$E_U(U) := B_{\text{NS}0U}(U) , \tag{81}$$

where following Reference [25], we assume the dependence of this component on U and this function must be determined by solving the equations of motion that follow from the probe action. Finally, notice that since

$$d[E_U(U)dX_0 \wedge dU] = 0 , \tag{82}$$

this does not affect the supergravity background.

3.3 Probe Action and Equations of Motion

Embedding Map

Writing down a D-brane action requires the information on how to embed the D-brane in the spacetime. We adopt the standard embedding map of the original paper [5]. To straighten out the notations and conventions, we explicitly write out the map.

Let the spacetime coordinates be

$$\text{spacetime: } X_\mu, \quad \mu = 0, 1, 2, 3, 4, u, \theta_1, \theta_2, \theta_3, \theta_4 , \tag{83}$$

and let the D8 worldvolume coordinates be

$$\text{D8: } x_\alpha, \quad \alpha = 0, 1, 2, 3, u, \theta_1, \theta_2, \theta_3, \theta_4 . \tag{84}$$

Note that $\alpha = 4$ is missing. With the slight abuse of notation, let X denote the embedding map

$$X : \text{D8} \rightarrow \text{spacetime} , \tag{85}$$

and following the standard practice, this is the identity map, except

$$X_4(x_\alpha) = x_4(x_u) , \tag{86}$$

where $x_4(x_u)$ is the profile function.

We define the metric on the D8-brane as the pullback of the spacetime metric two-tensor, with respect to the embedding map,

$$g_{\text{D8}} := X^* g_{\text{st}} , \tag{87}$$

and this yields

$$ds_{\text{D8}}^2 = \left(\frac{u}{R}\right)^{3/2} \left[f_t dx_0^2 + (dx_i)^2 + \left\{ x_4'^2 f_4 + \left(\frac{R}{u}\right)^3 f^{-1} \right\} du^2 \right] + \left(\frac{R}{u}\right)^{3/2} u^2 d\Omega_4^2, \quad (88)$$

where we have renamed as $x_u \rightarrow u$ and $x_4' := dx_4/du$. Parenthetically, we also have

$$\begin{aligned} f_t = f = 1 - (u_T/u)^3 \text{ and } f_4 = 1 \text{ for the high temperature deconfined phase} \\ f_4 = f = 1 - (u_{\text{KK}}/u)^3 \text{ and } f_t = 1 \text{ for the low temperature confined phase,} \end{aligned} \quad (89)$$

where the spacetime coordinate U in Equations (76) is changed to the worldvolume coordinate u . In addition, we pullback B_{NS} onto the D8 worldvolume, $\tilde{B}_{\text{NS}} := X^* B_{\text{NS}}$ and we have

$$\tilde{B}_{\text{NS}} = \begin{pmatrix} 0 & iE_1 & 0 & 0 & iE_u(u) \\ -iE_1 & 0 & B_3 & 0 & 0 \\ 0 & -B_3 & 0 & B_1 & 0 \\ 0 & 0 & -B_1 & 0 & 0 \\ -iE_u(u) & 0 & 0 & 0 & 0 \end{pmatrix}, \quad (90)$$

where we have dropped $E_{2,3}$ and B_2 , because we will be interested in the system with \vec{B} (\perp or \parallel) \vec{E} and for this purpose, the components above are sufficient. We have also extracted the factor of i and redefined the real $E_{1,u}$.

Probe Action

For our background $C_{(3)}$ and B_{NS} , we do not have the Chern-Simons coupling of the D8-brane, so the probe action consists only of the DBI part

$$S_{\text{DBI}} = 2T_8 \int d^9 x e^{-\Phi} \sqrt{\det(g_{\text{D8}} + \tilde{B}_{\text{NS}})}, \quad (91)$$

where T_8 is the brane tension and the factor of 2 comes from the D8 and $\overline{\text{D8}}$ contributions. We define the ‘‘Lagrangian’’ \mathcal{L} through the relation

$$e^{-\Phi} \sqrt{\det(g_{\text{D8}} + \tilde{B}_{\text{NS}})} = g_s^{-1} \mathcal{L} |\Omega_4|, \quad (92)$$

where

$$|\Omega_4| := \sin^3 \theta_1 \sin^2 \theta_2 \sin \theta_3. \quad (93)$$

According to the discussion made in Section 2.1, the cases $\vec{B} \parallel \vec{E}$ ($B_3 = 0$) and $\vec{B} \perp \vec{E}$ ($B_1 = 0$) correspond to the $U(1)_A$ anomalous and non-anomalous boundary theory, respectively. Though we are interested in the non-anomalous case at the end, we carry out the analysis for both cases up until the numerical evaluation, because it is easy to generalize to $N_f > 1$ and we can observe some general similarities and dissimilarities to the NJL model. Examining separately for those cases, we obtain for the anomalous case

$$\mathcal{L}_{\text{Anom}} = u^4 \left[\left\{ (R/u)^3 f_4^{-1} + f x_4'^2 \right\} \mathcal{B}_1 \mathcal{E}_1 - (R/u)^3 \mathcal{B}_1 E_u^2 \right]^{1/2}, \quad (94)$$

and for the non-anomalous case

$$\mathcal{L}_{\text{NAnom}} = u^4 \left[\{ (R/u)^3 f_4^{-1} + f x_4'^2 \} \mathcal{A} - (R/u)^3 \mathcal{B}_3 E_u^2 \right]^{1/2}, \quad (95)$$

where we have defined

$$\begin{aligned} \mathcal{B}_i &:= 1 + (R/u)^3 B_i^2, \quad \mathcal{E}_1 := 1 - (R/u)^3 f_t^{-1} E_1^2 \\ \text{and } \mathcal{A} &:= 1 + (R/u)^3 (B_3^2 - f_t^{-1} E_1^2). \end{aligned} \quad (96)$$

We see that \mathcal{L} s depend only on the coordinate u , so the action can be written as

$$S_{\text{DBI}} = 2\omega_4 V_3 T_8 g_s^{-1} \beta \int du \mathcal{L}, \quad (97)$$

where β is the integration of Euclidean time,

$$\omega_4 := \int d\theta_1 d\theta_2 d\theta_3 d\theta_4 |\Omega_4|, \quad \text{and} \quad V_3 = \int d^3 x_i. \quad (98)$$

Equations of Motion

The degrees of freedom in the action appears to be $x_4(u)$ and $E_u(u)$. In the D8 worldvolume, however, it is more natural to trade \tilde{B}_{NS} to $2\pi\alpha'F$, that is, we identify $(\tilde{B}_{\text{NS}})_{0u} = E_u(u)$ as the u derivative of the worldvolume gauge field A_0 , and treat the gauge field as the degrees of freedom in the action (see Reference [25]). Thus, we replace as

$$E_u(u) \rightarrow \mu(u)' := 2\pi\alpha' \partial_u A_0(u) = 2\pi \left(\frac{l_s}{R} \right)^2 \frac{\partial(A_0 R)}{\partial(u/R)}, \quad (99)$$

where we have emphasized that everything is measured in the units of the scale R and μ is dimensionless that involves the factor of $(l_s/R)^2$ in its definition.

Identifying the degrees of freedom, the equations of motion that follow from the action are

$$\frac{\partial \mathcal{L}}{\partial x_4'} = c_1 \quad \text{and} \quad \frac{\partial \mathcal{L}}{\partial \mu'} = -c_2, \quad (100)$$

where $c_{1,2}$ are the constants of motion and the minus sign on c_2 is inserted for the later convenience. For $\mathcal{L}_{\text{NAnom}}$ of Equation (95), they lead to

$$\begin{aligned} c_1 &= u^4 f \mathcal{A} x_4' \left[\{ (R/u)^3 f_4^{-1} + f x_4'^2 \} \mathcal{A} - (R/u)^3 \mathcal{B}_3 \mu'^2 \right]^{-1/2} \\ c_2 &= u^4 \mathcal{B}_3 (R/u)^3 \mu' \left[\{ (R/u)^3 f_4^{-1} + f x_4'^2 \} \mathcal{A} - (R/u)^3 \mathcal{B}_3 \mu'^2 \right]^{-1/2}. \end{aligned} \quad (101)$$

The equations of motion for $\mathcal{L}_{\text{Anom}}$ of Equation (94) can be obtained by the replacements $\mathcal{A} \rightarrow \mathcal{B}_1 \mathcal{E}_1$ and $\mathcal{B}_3 \rightarrow \mathcal{B}_1$.

3.4 Confined Phase

We now specialize the discussion to the confined phase. We will concentrate on the $\vec{B} \perp \vec{E}$ non-anomalous case, Equation (95), because the anomalous case, Equation (94), can be obtained by the replacement just mentioned. For the clarity of expressions, we set $B := B_3$ and $E := E_1$, accordingly, we have $\mathcal{A} = 1 + (R/u)^3(B^2 - E^2)$ and $\mathcal{B} := 1 + (R/u)^3B^2$. Also we remember that in this phase, $f_t = 1$ and $f_4 = f = 1 - (u_{\text{KK}}/u)^3$.

The U-Shape Solution and the Free Energy

The x_4 direction is degenerate at $u = u_{\text{KK}}$ in this phase (see Figure 23) and the D8 and $\overline{\text{D8}}$ probes must join somewhere. Following the common practice, we assume that the probes join smoothly at $u = u_0$, forming a U shape, and this results in the condition

$$x'_4(u_0) = \infty . \quad (102)$$

The equations of motion (101) can be solved for x'_4 and μ' , then we can use the condition (102) to eliminate the constant c_1 in favor of u_0 . By resetting $c := c_2$, we obtain

$$\begin{aligned} x_4'^2 &= \frac{(R/u)^6 f_0(\mathcal{A}_0/\mathcal{B}_0) \{u_0^8 \mathcal{B}_0 + c^2 (u_0/R)^3\}}{f^2 [(R/u)^3 (u^8 f \mathcal{A} - u_0^8 f_0 \mathcal{A}_0) + (c^2/u^3) \{u^3 f(\mathcal{A}/\mathcal{B}) - u_0^3 f_0(\mathcal{A}_0/\mathcal{B}_0)\}]} \\ \mu'^2 &= \frac{(\mathcal{A}/\mathcal{B})^2 c^2}{(R/u)^3 (u^8 f \mathcal{A} - u_0^8 f_0 \mathcal{A}_0) + (c^2/u^3) \{u^3 f(\mathcal{A}/\mathcal{B}) - u_0^3 f_0(\mathcal{A}_0/\mathcal{B}_0)\}} , \end{aligned} \quad (103)$$

where the quantities X_0 are meant to be $X(u_0)$.

It is clear in the equation of μ' that this blows up at $u = u_0$ leading to a singular B_{NS} . To avoid the singularity, we must set

$$c = 0 , \quad (104)$$

for this U-shape solution and the solution boils down to

$$x_4'^2 = f^{-2} \left(\frac{R}{u} \right)^3 \left(\frac{u^8 f \mathcal{A}}{u_0^8 f_0 \mathcal{A}_0} - 1 \right)^{-1} \quad \text{and} \quad \mu' \equiv 0 . \quad (105)$$

The condition (104) has the drastic consequence that the system is completely independent of the chemical potential μ and in particular, the dynamical mass will be insensitive to the chemical potential.

Consulting with Equation (97), we define the (dimensionless) free energy of the system by

$$\hat{F} := R^{-5} \int_{u_0}^{\infty} du \mathcal{L} , \quad (106)$$

and we are going to evaluate the free energy for the solution derived above. Plugging the solution (105) in the Lagrangian (95), we obtain the on-shell expression

$$\mathcal{L} = u^4 \left(\frac{R}{u} \right)^{3/2} f^{-1/2} \mathcal{A}^{1/2} \left(1 - \frac{u_0^8 f_0 \mathcal{A}_0}{u^8 f \mathcal{A}} \right)^{-1/2} . \quad (107)$$

Following Reference [22], we measure the quantities in the units of u_0 by introducing¹³

$$y := u/u_0, \quad y_R := R/u_0, \quad \text{and} \quad y_{\text{KK}} := u_{\text{KK}}/u_0. \quad (108)$$

Again, following the same reference, we further set $z = y^{-3}$, yielding

$$\hat{F} = \frac{1}{3} y_R^{-7/2} \int_0^1 dz z^{-13/6} f^{-1/2} \mathcal{A}^{1/2} \left(1 - z^{8/3} \frac{f_0 \mathcal{A}_0}{f \mathcal{A}} \right)^{-1/2}. \quad (109)$$

From the relation (77), we have

$$y_R = a^{-1} \hat{\beta}_4^2 y_{\text{KK}} \quad \text{with} \quad a := \left(\frac{4\pi}{3} \right)^2 \quad \text{and} \quad \hat{\beta}_4 := \beta_4/R, \quad (110)$$

and we can eliminate y_R in favor of y_{KK} . We then have

$$\begin{aligned} \hat{F} &= \frac{1}{3} (a^{-1} \hat{\beta}_4^2)^{-7/2} y_{\text{KK}}^{-7/2} \int_0^1 dz z^{-13/6} f^{-1/2} \mathcal{A}^{1/2} \left(1 - z^{8/3} \frac{f_0 \mathcal{A}_0}{f \mathcal{A}} \right)^{-1/2} \\ f &= 1 - y_{\text{KK}}^3 z, \quad \mathcal{A} = 1 + z \hat{\beta}_4^6 y_{\text{KK}}^3 (\bar{B}^2 - \bar{E}^2), \\ f_0 &= 1 - y_{\text{KK}}^3, \quad \mathcal{A}_0 = 1 + \hat{\beta}_4^6 y_{\text{KK}}^3 (\bar{B}^2 - \bar{E}^2), \end{aligned} \quad (111)$$

where we set $\bar{B} := a^{-3/2} B$ and $\bar{E} := a^{-3/2} E$. We again note that the anomalous case with the Lagrangian (94) can be obtained by the replacement $\mathcal{A} \rightarrow \mathcal{B}_1 \mathcal{E}_1$.

The free energy obtained above actually is ill-defined, for it diverges at $z = 0$, and currently it is not known how to regulate this. Still, we can draw general conclusions from the free energy. Consider the case with $B = 0$. Then we see that the electric field may not exceed the critical value

$$E^2 < \left(\frac{u_0}{R} \right)^3. \quad (112)$$

This is the curved space version of the upper limit on the electric field in string theory. Beyond this value, the free energy becomes imaginary, indicating the instability of the system. Thus, the electric field acts as a sort of “destabilizer” in the system. On the contrary, we note that the B field behaves exactly the opposite; it is the “stabilizer” for the $\vec{B} \perp \vec{E}$ non-anomalous case. In particular, those effects exactly cancel when $B = E$ and the system is completely the same as the one without the external electromagnetic fields. For the anomalous $\vec{B} \parallel \vec{E}$ case, those external fields do not interfere each other and they behave more or less independently. Later, we will compare these behaviors to those of the NJL model.

Inter-Brane Distance and SEP

The SS model has another parameter L which is the asymptotic separation of the D8 and $\overline{\text{D8}}$. This is related to the parameter $y_{\text{KK}} := u_{\text{KK}}/u_0$ and we prefer L to y_{KK} as the fundamental parameter of the theory.

¹³ This scaling by u_0 is a temporary prescription and as mentioned earlier, we will measure all physical quantities in the units of R at the end.

For the relation between those parameters, we start with the equation

$$L = \int dx_4 = 2 \int_{u_0}^{\infty} x_4' du, \quad (113)$$

where the factor of 2 accounts for D8 and $\overline{\text{D8}}$. Using the solution (105) and carrying out the changes of variables $u \rightarrow y \rightarrow z$ as before, we obtain

$$\begin{aligned} \ell &:= \hat{L}/\hat{\beta}_4 \\ &= \frac{2}{3} a^{-1/2} y_{\text{KK}}^{1/2} \int_0^1 dz f^{-1} \left(z^{-1} \frac{f\mathcal{A}}{f_0\mathcal{A}_0} - z^{5/3} \right)^{-1/2}, \end{aligned} \quad (114)$$

where we have defined $\hat{L} := L/R$ and ℓ has the range $0 < \ell \leq 1/2$.

Now the dynamical mass (SEP) discussed in Section 3.1 can be written as

$$m^* R = \frac{R^2}{2\pi\alpha'} (u_0/R) \int_{y_{\text{KK}}}^1 f(y)^{-1/2} dy. \quad (115)$$

We notice that the mass is totally independent of the temperature and the chemical potential. It turns out that the y integral can be carried out to yield a closed form as a function of y_{KK} . Trading the parameter u_0/R to $\hat{\beta}_4$ and y_{KK} using the relation (110), we get

$$\begin{aligned} \hat{m}^* &:= 2\pi \left(\frac{l_s}{R} \right)^2 (m^* R) \\ &= a \hat{\beta}_4^{-2} \left\{ -\sqrt{\pi} \Gamma(2/3)/\Gamma(1/6) + y_{\text{KK}}^{-1} {}_2F_1(-1/3, 1/2, 2/3, y_{\text{KK}}^3) \right\}. \end{aligned} \quad (116)$$

This dimensionless mass \hat{m}^* together with Equation (114) is ready for the numerical evaluation.

3.5 Deconfined Phase

We now proceed to examine the deconfined phase. Strictly speaking, the discussion here would make sense only above the confinement/deconfinement critical temperature. However as mentioned earlier, we can always consider a very large β_4 or even the non-compact x_4 model, so we will freely discuss the low temperature behavior of this phase without worrying about the critical temperature. Like in the confined case, we will concentrate on the $\vec{B} \perp \vec{E}$ non-anomalous case with the Lagrangian (95). For the clarity of expressions, we set $B := B_3$ and $E := E_1$, accordingly we have $\mathcal{A} = 1 + (R/u)^3 (B^2 - f^{-1} E^2)$ and $\mathcal{B} := 1 + (R/u)^3 B^2$. Also we remember that in this phase, $f_4 = 1$ and $f_t = f = 1 - (u_T/u)^3$.

The U- and ||-Shape Solutions

In the deconfined phase, the x_0 direction is degenerate at $u = u_T$ but the x_4 direction is not (see Figure 23). Therefore, the D8 and $\overline{\text{D8}}$ probes can either join smoothly in the U shape or go straight down to the horizon, forming the || shape. Those configurations correspond to the broken and unbroken chiral symmetry phases, respectively.

The derivation of the U-shape solution from the equations of motion (101) is nearly identical to the confined case and we have

$$x_4'^2 = f^{-1} \left(\frac{R}{u} \right)^3 \left(\frac{u^8 f \mathcal{A}}{u_0^8 f_0 \mathcal{A}_0} - 1 \right)^{-1} \quad \text{and} \quad \mu' \equiv 0. \quad (117)$$

Again, the system in the U shape is completely independent of the chemical potential μ and in particular, the dynamical mass will be insensitive to the chemical potential.

For the ||-shape configuration, we have $x'_4(u) \equiv 0$. Thus, the equations of motion (101) yield the || solution

$$x'_4 \equiv 0 \quad \text{and} \quad \mu'^2 = \frac{\mathcal{A}c^2}{\mathcal{B}\{u^8(R/u)^3\mathcal{B} + c^2\}}, \quad (118)$$

where we set $c := c_2$. The anomalous $\vec{B} \parallel \vec{E}$ solution can be obtained by the replacements $\mathcal{A} \rightarrow \mathcal{B}_1\mathcal{E}_1$ and $\mathcal{B} \rightarrow \mathcal{B}_1$.

We notice that for any finite E , there is a factor $f^{-1}E^2$ inside \mathcal{A} (or \mathcal{E}) and this diverges at $u = u_T$. To avoid this, we must conclude that we need $c = 0$, *i.e.*, $\mu' = 0$ for any $E \neq 0$. Moreover, since μ must vanish at the horizon, we get $\mu \equiv 0$. This strong conclusion has a clear physical interpretation. In the deconfined and chirally symmetric phase, quarks and anti-quarks are not bound together and the chemical potential causes the unbalance in the charge density. Thus, application of the external electric field immediately triggers the instability. Note that the key factor in this instability is $f^{-1}E^2$, which is the direct consequence from the violation of the topological constraint discussed in Section 3.2.

The Difference Action

Given the two solutions, we must determine the energetically preferred configuration for a set of external parameters. For this purpose, we compute the difference action with respect to the solutions. As before, we define the dimensionless free energy

$$\hat{F} := R^{-5} \int du \mathcal{L}, \quad (119)$$

where \mathcal{L} is given in Equation (95). Evaluating the Lagrangian for the solutions (117) and (118), we get

$$\begin{aligned} \mathcal{L}_U &= u^4 \left(\frac{R}{u}\right)^{3/2} \mathcal{A}^{1/2} \left(1 - \frac{u_0^8 f_0 \mathcal{A}_0}{u^8 f \mathcal{A}}\right)^{-1/2} \\ \mathcal{L}_{\parallel} &= u^4 \left(\frac{R}{u}\right)^{3/2} \mathcal{A}^{1/2} \left(1 + \frac{c^2}{u^8 (R/u)^3 \mathcal{B}}\right)^{-1/2}. \end{aligned} \quad (120)$$

Now the difference of the free energies is

$$\Delta \hat{F} = R^{-5} \int_{u_0}^{\infty} du \mathcal{L}_U - R^{-5} \int_{u_T}^{\infty} du \mathcal{L}_{\parallel}, \quad (121)$$

so that when this is negative (resp. positive), the U shape (resp. || shape) is preferred. For the numerical handiness, we rewrite this as

$$\begin{aligned} \Delta \hat{F} &= \int_{u_0}^{\infty} \frac{du}{R} \left(\frac{u}{R}\right)^{5/2} \mathcal{A}^{1/2} \left\{ \left(1 - \frac{u_0^8 f_0 \mathcal{A}_0}{u^8 f \mathcal{A}}\right)^{-1/2} - \left(1 + \frac{c^2}{u^8 (R/u)^3 \mathcal{B}}\right)^{-1/2} \right\} \\ &\quad - \int_{u_T}^{u_0} \frac{du}{R} \left(\frac{u}{R}\right)^{5/2} \mathcal{A}^{1/2} \left(1 + \frac{c^2}{u^8 (R/u)^3 \mathcal{B}}\right)^{-1/2}. \end{aligned} \quad (122)$$

We carry out the sequence of the variable changes, $u \rightarrow y \rightarrow z$, as was done in Section 3.4. Assuming the relation

$$y_R = a^{-1} \hat{\beta}^2 y_T \quad \text{with} \quad a := \left(\frac{4\pi}{3} \right)^2 \quad \text{and} \quad \hat{\beta} := \beta/R, \quad (123)$$

that follows from Equation (78), we have the expression of $\Delta \hat{F}$ in terms of y_T as

$$\begin{aligned} (3y_R^{7/2}) \Delta \hat{F} = & \int_0^1 dz z^{-13/6} \mathcal{A}^{1/2} \left\{ \left(1 - z^{8/3} \frac{f_0 \mathcal{A}_0}{f \mathcal{A}} \right)^{-1/2} - \left(1 + z^{5/3} \frac{C}{y_R^3 \mathcal{B}} \right)^{-1/2} \right\} \\ & - \int_1^{y_T^{-3}} dz z^{-13/6} \mathcal{A}^{1/2} \left(1 + z^{5/3} \frac{C}{y_R^3 \mathcal{B}} \right)^{-1/2}, \end{aligned} \quad (124)$$

where $C := c^2/u_0^8$ and we have

$$f = 1 - y_T^3 z, \quad f_0 = 1 - y_T^3, \quad (125)$$

and setting $\bar{B} := a^{-3/2} B$ and $\bar{E} := a^{-3/2} E$,

$$\begin{aligned} \mathcal{A} = & 1 + z \hat{\beta}^6 y_T^3 (\bar{B}^2 - f^{-1} \bar{E}^2), \quad \mathcal{B} = 1 + z \hat{\beta}^6 y_T^3 \bar{B}^2, \quad \mathcal{E} = 1 - z \hat{\beta}^6 y_T^3 f^{-1} \bar{E}^2, \\ \mathcal{A}_0 = & 1 + \hat{\beta}^6 y_T^3 (\bar{B}^2 - f_0^{-1} \bar{E}^2), \quad \mathcal{B}_0 = 1 + \hat{\beta}^6 y_T^3 \bar{B}^2, \quad \mathcal{E}_0 = 1 - \hat{\beta}^6 y_T^3 f_0^{-1} \bar{E}^2. \end{aligned} \quad (126)$$

As noted before, because of the factor $f^{-1} E^2$ in \mathcal{A} and \mathcal{E} , the integrand of the second line in Equation (124) is divergent at $z = y_T^{-3}$, however, it turns out that the integral is finite. When we consider the pure E background, we find that the difference free energy is complex and the imaginary part comes only from the \parallel configuration. But since we cannot define the action without taking the difference, we treat the complex value as representing the nature of the whole system.

Chemical Potential, Inter-Brane Distance and SEP

The \parallel configuration without the E field has the non-trivial μ' as shown in Equation (118). We would like to set the asymptotic value of μ to $\bar{\mu}$, which should correspond to the chemical potential of the dual field theory. We must also require that $\mu(u_T) = 0$. Therefore,

$$\begin{aligned} \bar{\mu} = & \int_{u_T}^{\infty} du \left[\frac{\mathcal{A} c^2}{\mathcal{B} \{ u^8 (R/u)^3 \mathcal{B} + c^2 \}} \right]^{1/2} \\ = & \frac{1}{3} a \hat{\beta}^{-2} y_T^{-1} \int_0^{y_T^{-3}} dz z^{-1/2} \left[\frac{AC}{\mathcal{B} \{ a^{-3} \hat{\beta}^6 y_T^3 \mathcal{B} + C z^{5/3} \}} \right]^{1/2}. \end{aligned} \quad (127)$$

The asymptotic brane distance for the \parallel -shape configuration is a parameter on which no other parameters depend. That of the U-shape configuration can be worked out in the similar manner as in the confined case and we get

$$\begin{aligned} \hat{L} := & L/R \\ = & \frac{2}{3} \hat{\beta} a^{-1/2} y_T^{1/2} \int_0^1 dz f^{-1/2} \left(z^{-1} \frac{f \mathcal{A}}{f_0 \mathcal{A}_0} - z^{5/3} \right)^{-1/2}. \end{aligned} \quad (128)$$

The dynamical mass is simply proportional to the distance $(u_0 - u_T)$, because we have $\sqrt{g_{00}g_{UU}} = 1$, and we get

$$\begin{aligned}\hat{m}^* &:= 2\pi \left(\frac{l_s}{R}\right)^2 (m^* R) \\ &= a\hat{\beta}^{-2}(y_T^{-1} - 1).\end{aligned}\tag{129}$$

The expressions for $\Delta\hat{F}$, $\hat{\mu}$, \hat{L} and \hat{m}^* obtained in this subsection are ready for the numerical evaluation and they suffice to determine the dynamical mass and the phase structure of the deconfined phase.

Zero Temperature

For the sake of the comparison with the NJL model, it is interesting and important to consider the deconfined phase in the low temperature regime, including at zero temperature. At zero temperature, the parameters of the theory change slightly. We must replace the ‘‘blackening factors’’ as $f, f_0 \rightarrow 1$ and we have the range $0 < u < \infty$ where u_T is no longer the parameter of the theory. We then have

$$\mathcal{A} := 1 + zy_R^3 a^3 (\bar{B}^2 - \bar{E}^2), \quad \mathcal{B} := 1 + zy_R^3 a^3 \bar{B}^2, \quad \mathcal{E} := 1 - zy_R^3 a^3 \bar{E}^2, \tag{130}$$

where we have extracted the factor of a by $B^2 = a^3(a^{-3}B^2) = a^3\bar{B}^2$ and similarly for E , to be consistent with the finite temperature parameters.

The difference free energy shown in Equation (124) does not change, except that the parameter y_R is the parameter of the theory itself and *not* expressed in terms of y_T , and the replacement (130) is assumed. Examination of the difference free energy shows that the U-shape configuration is preferred to the \parallel configuration at zero temperature.

The chemical potential and the inter-brane distance for $T = 0$ take the forms

$$\begin{aligned}\hat{\mu} &= \frac{1}{3}y_R^{-1} \int_0^\infty dz z^{-1/2} \left[\frac{AC}{\mathcal{B}\{y_R^3\mathcal{B} + Cz^{5/3}\}} \right]^{1/2} \\ \hat{L} &= \frac{2}{3}y_R^{1/2} \int_0^1 dz z^{-5/6} \left(z^{-8/3} \frac{\mathcal{A}}{\mathcal{A}_0} - 1 \right)^{-1/2}.\end{aligned}\tag{131}$$

It is also easy to show that the mass becomes

$$\hat{m}^* = 2\pi \left(\frac{l_s}{R}\right)^2 (m^* R) = y_R^{-1}.\tag{132}$$

3.6 Numerical Evaluation

We now present the numerical results, separately for the confined and deconfined phases. In this section, we assume all the quantities are measured in the units of R and we are going to omit the hats (\hat{X}) on the parameters.

3.6.1 Confined Phase

We have seen in Section 3.4 that the system is independent of the temperature and the chemical potential, except that this phase is defined below the critical temperature of the

confinement/deconfinement phase transition. Therefore, the only parameters are the external electromagnetic field and the inter-brane distance. As for the numerical evaluation, the relevant equations are $\ell := L/\beta_4$ of (114) and m^* of (116).

We first examine the properties related to the parameter ℓ without the background electromagnetic field. From Equation (114), we can plot ℓ with respect to y_{KK} and it is shown in Figure 25. Recall that the ranges of ℓ and y_{KK} are $(0, 1/2)$ and $(0, 1)$, respectively,

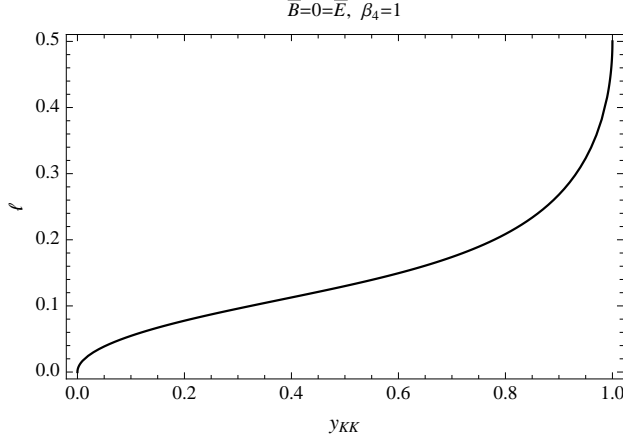


Figure 25: The plot of ℓ with respect to the variable y_{KK} without electromagnetic background and $\beta_4 = 1$. This shows that the location of D8 and $\overline{D8}$ can be anywhere in the x_4 circle.

and the figure shows that the parameter ℓ takes all the possible values. We remark that the lower bound 2 of ℓ^{-1} is the geometrical constraint and not the bound determined by the dynamics (like the NJL coupling g_c). We will further discuss the comparison between ℓ^{-1} and g later in Section 4.

Figure 26 shows the response of SEP with respect to ℓ^{-1} . The left panel shows the

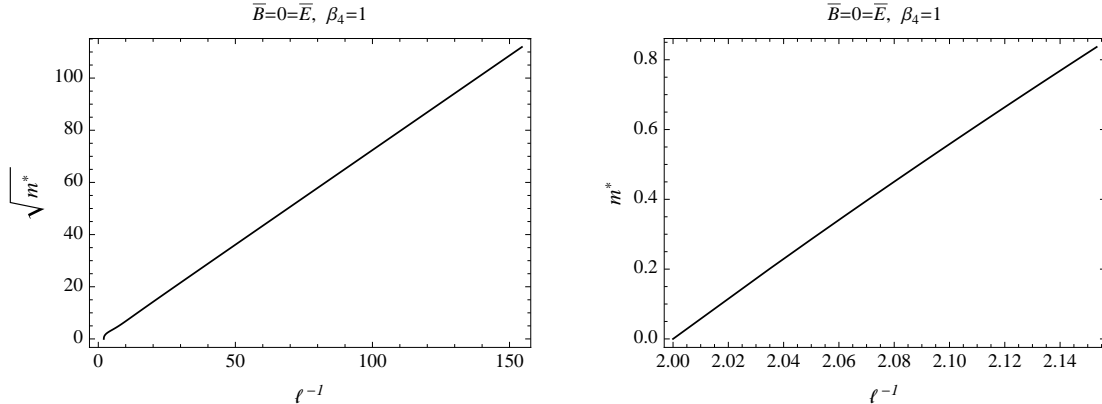


Figure 26: The plots of mass m^* against ℓ^{-1} ($2 \leq \ell^{-1} < \infty$). The left panel implies the relation $m^* \sim (\ell^{-1})^2$ for large values of ℓ^{-1} and the right panel shows that the relation $m^* \sim \ell^{-1}$ is fairly well for small values of ℓ^{-1} .

relation $m^* \sim (\ell^{-1})^2$ for the range of large ℓ^{-1} away from the lower bound and the right panel shows that near the lower bound 2, we have the linear relation $m^* \sim \ell^{-1}$.

Pure B Background

When the B field is turned on, the $y_{\text{KK}}-\ell$ graph appears essentially the same as Figure 25 and the parameter ℓ takes all the possible value $0 < \ell \leq 1/2$. The response of the mass with respect to B is shown in Figure 27. The graph shows the general tendency that B acts

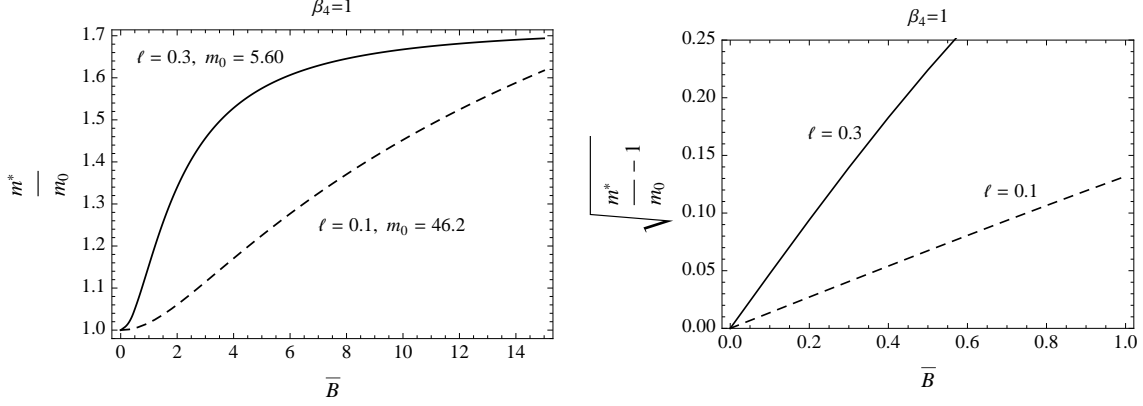


Figure 27: The SEP against the B field. We have defined $m_0 := m^*(\bar{B} = 0)$ and notice that the absolute value m^* is much larger for $\ell = 0.1$. The right panel shows the relation $m^* \sim \bar{B}^2$ for small values of \bar{B}

as the stabilizer of the boundstate. The right diagram reveals the relation $m^* \sim \bar{B}^2$ in the region of small \bar{B} .

Pure E Background

When we turn on the E field, the $y_{\text{KK}}-\ell$ relation becomes more complicated. The left panel

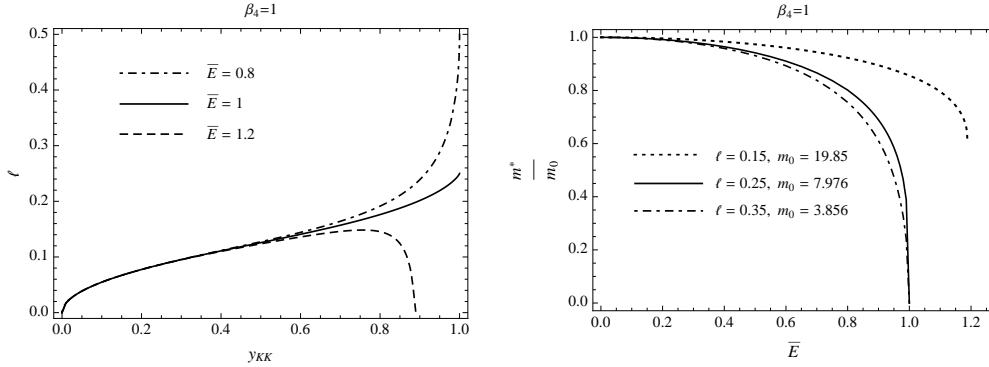


Figure 28: The left panel shows that for $\bar{E} < 1$, ℓ takes all allowed values $0 < \ell < 1/2$, and for $\bar{E} > 1$, ℓ has upper limit, implying that the D8 and $\overline{\text{D8}}$ may not be separated too far. Notice in this case that there are two solutions of y_{KK} for a given ℓ . The critical value $\bar{E} = 1$ shown in this figure depends on the value of β_4 , and in general, the critical value is given at $(\beta_4^3 \bar{E}) = 1$. At this value, the curve approaches the point $(y_{\text{KK}}, \ell) = (1, 1/4)$. The right panel shows the response of the dynamical masses with respect to \bar{E} . The parameter m_0 is the value of m^* at $\bar{E} = 0$. For $1/4 \leq \ell < 1/2$, the dynamical mass goes smoothly to zero at $\bar{E} = 1$ and beyond which the system becomes unstable. For $\ell < 1/4$, the system becomes unstable before the mass becomes zero.

of Figure 28 shows that there is a critical value $(\beta_4^3 \bar{E}) = 1$, above which ℓ takes all possible values and below, there is an upper limit which is lower than $1/2$. Therefore, for sufficiently large value of $(\beta_4^3 \bar{E})$, the D8 probe system becomes ill-defined. Since the supergravity background is in the confined phase, the physical implication of this instability is unclear.

Notice that when the E field is below the critical value, there can be two solutions of y_{KK} for a given ℓ . One can show along the analysis of Reference [5] that the lower y_{KK} solution is the stable configuration and the other is unstable. Hence, we always pick the lower y_{KK} solutions to obtain the dynamical masses. The right panel of Figure 28 shows how the dynamical mass respond to the E field. As expected, the graph shows the general tendency of E as the destabilizer. As discussed in the previous paragraph, there is a critical value of \bar{E} and the curves in the diagram terminate there.

3.6.2 Deconfined Phase

As mentioned in Section 3.5, we will be cavalier about the confinement/deconfinement phase transition temperature and discuss this phase in all temperature range, including zero temperature.

Let us first examine the range of parameter L without the electromagnetic background. Unlike the confined phase, L in the deconfined phase depends on the temperature, as shown in Equation (128) and the zero temperature case is given in Equation (131). Figure 29 shows the plots of L for different temperatures. The left panel of the zero temperature plot shows

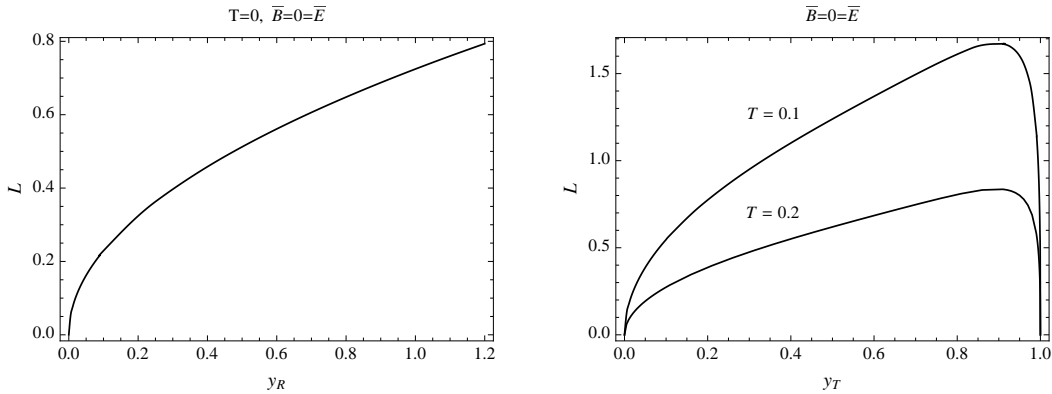


Figure 29: The plots of the inter-brane distance L in the U-shape configuration. The left panel is for $T = 0$ and this case is assumed to be the non-compact model. There is no upper limit on L and it increases as $\sqrt{y_R}$. The right panel is plotted for finite temperatures. Any finite temperature induces the upper limit on L , *i.e.*, D8- $\bar{D}8$ inter-distance may not be too large to form the U shape.

that there is no upper limit on L and it increases as $\sqrt{y_R}$. This is a manifestation of the fact that at zero temperature, the U-shape configuration is always preferred to the parallel one, as mentioned in Section 3.5. The right panel shows that finite temperature introduces the upper limit on L . For a fixed value of L , a sufficiently high temperature yields no solution for y_T (*e.g.*, at $L = 1.0$ and $T = 0.2$ of the diagram), implying that the system is actually in the chirally symmetric \parallel -shape configuration. Here again, the temperature plays the role of the destabilizer of the quark boundstate. Meanwhile, a sufficiently low temperature yields two solutions for y_T (*e.g.*, at $L = 1.0$ and $T = 0.1$ of the diagram). As discussed in Section 3.6.1, the smaller solution is the stable configuration and we will always pick this one in what follows.

Before introducing the background electromagnetic field, we would like to examine the response of SEP with respect to L^{-1} . One can obtain the mass as a function of L^{-1} from Equations (131,132) for $T = 0$, and for finite temperature, from Equations (128,129). The

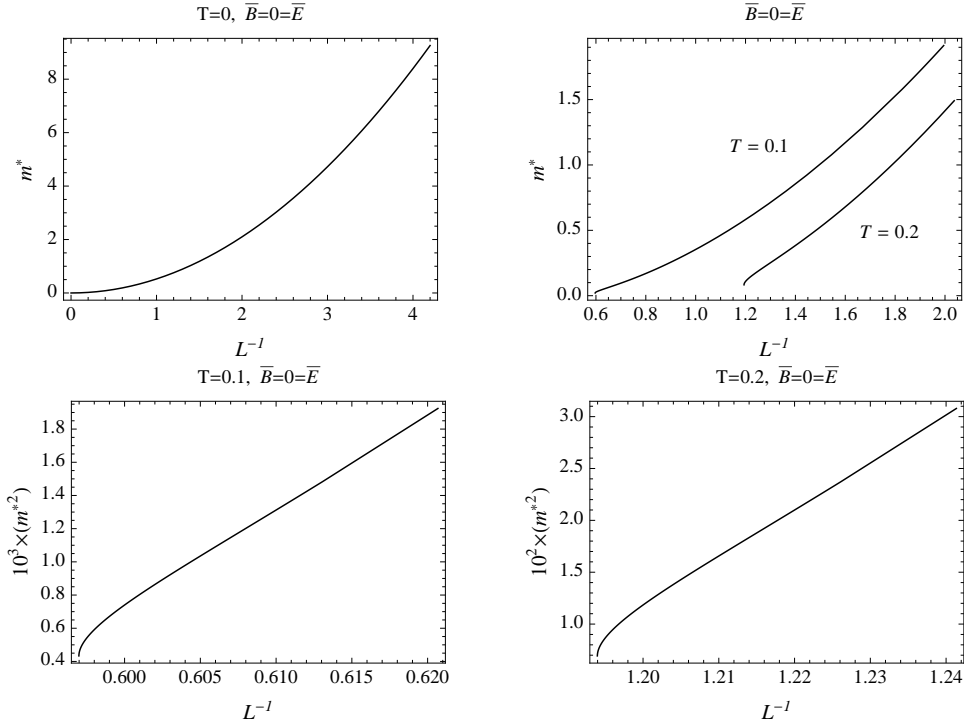


Figure 30: The plots of m^* against L^{-1} . For $T = 0$ (upper left corner), the relation $m^* \sim (L^{-1})^2$ holds for all values of L^{-1} . At finite temperature, the relation is more complicated as shown in the upper right corner. The bottom two indicate the relation $m^* \sim (L^{-1})^{1/2}$ in the region of small L^{-1} , but slightly away from the critical values.

results are shown in Figure 30. The upper left panel of the figure shows the $T = 0$ case and one can show analytically for this case that m^* increases quadratically with respect to L^{-1} . The upper right panel shows the finite temperature cases and these are more complicated than the zero temperature. We have observed in Figure 29 that there is an upper bound on L for a given temperature. This translates to the lower bound on L^{-1} and the plots of the upper right panel terminates at those critical values of L^{-1} . The diagrams of the bottom row are plotted for the region near the critical values of L^{-1} and show the fairly good relation $m^* \sim \sqrt{L^{-1}}$ slightly away from the critical values.

Pure B Background

We now consider the effects of the constant background B field. At $T = 0$ without the B field, we have seen that there is no upper limit on L , and finite B -field does not change this conclusion. Neither does it change the general observation that finite temperature introduces an upper limit on L . In short, L behaves similar to Figure 29, except that the larger B allows the larger separation L for a given $y_{R,T}$. This, of course, implies that the B field acts as the stabilizer of the quark boundstate.

In the deconfined phase, the system exhibits the chiral phase transition from the U-shape to the ||-shape configuration, which cannot take place in the confined phase. Unlike the way we presented the NJL results, we first show the phase diagram before the response of the dynamical mass with respect to the external parameters. This is because we must consult with the chiral phase diagrams to determine exactly where the mass drops to zero

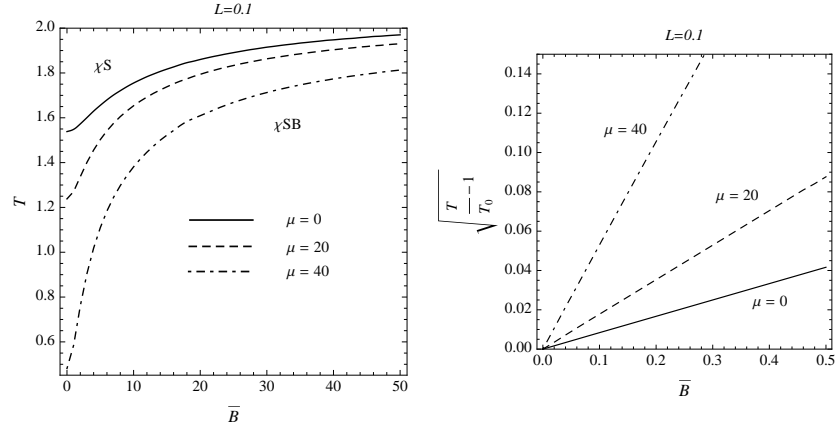


Figure 31: The B - T phase diagram at $L = 0.1$. The right panel shows the region of small \bar{B} and the parameter T_0 is the critical temperature at $\bar{B} = 0$. It shows the relation $T \sim \bar{B}^2$ in the region of small \bar{B} .

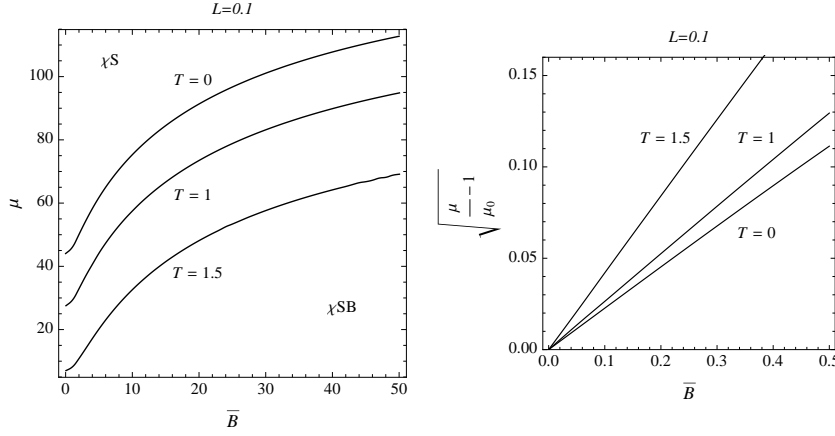


Figure 32: The B - μ phase diagram at $L = 0.1$. The right panel shows the region of small \bar{B} and the parameter μ_0 is the critical value of the chemical potential at $\bar{B} = 0$. It shows the relation $\mu \sim \bar{B}^2$ in the region of small \bar{B} .

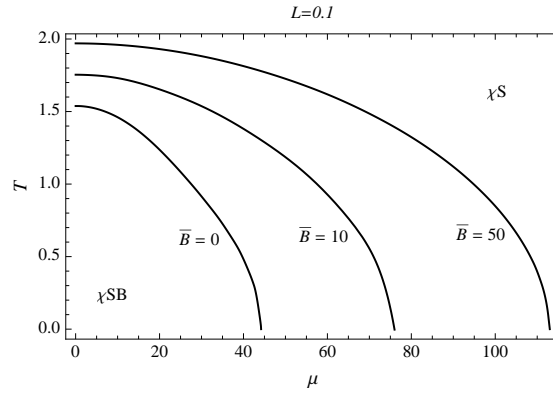


Figure 33: The μ - T phase diagram at $L = 0.1$. The case with $\bar{B} = 0$ reproduces the result of Reference [25] (the reference plots TL against μL^2).

at the phase transition point.

The phase diagrams can be all worked out from Equations (124,127,128) and Figures 31, 32 and 33 show the B - T , B - μ and μ - T phase diagrams, respectively. The transitions are all first order as the configuration “jumps” from U- to ||-shape. We observe the general trend that B acts as the stabilizer and T , μ as the destabilizer. This fact appears as the general similarity in the B - T and B - μ graphs.

Let us now investigate the response of the dynamical mass with respect to the external parameters. Figure 34 shows the B - m^* graph. As expected, the mass increases as \bar{B} is

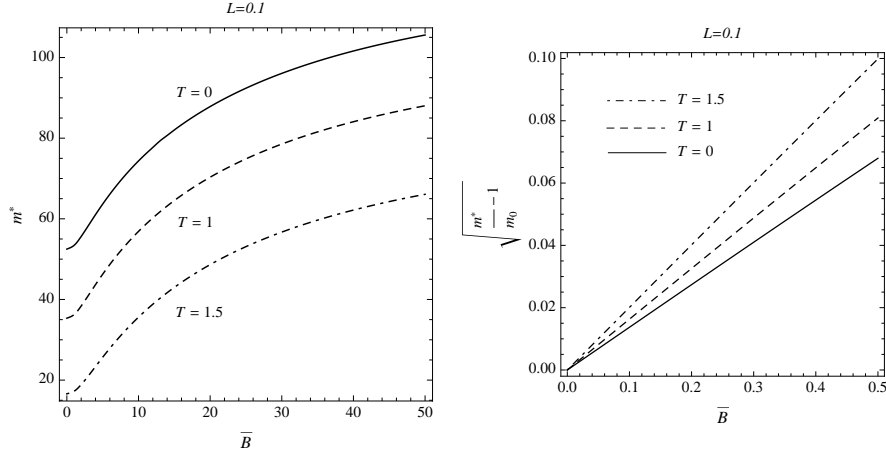


Figure 34: The SEP plotted against B -field. The right panel exhibits the small \bar{B} region and the parameter m_0 is defined as the mass at $\bar{B} = 0$. The diagram shows the relation $m^* \sim \bar{B}^2$ in the region of small \bar{B} . Typically at high temperature, the lower B region of these curves may sharply drop to zero as the chiral phase transition sets in and the point of the drop depends on the temperature and the chemical potential.

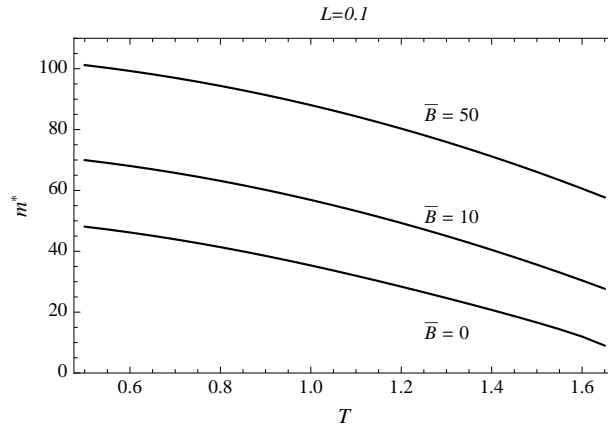


Figure 35: The plot of mass against temperature. One must be aware that the low temperature region is subject to the confinement/deconfinement phase transition, unless β_4 is large enough, and the high temperature region typically drops to the zero mass sharply due to the chiral phase transition. The point of the chiral phase transition depends on the chemical potential as well.

raised and higher temperature results in the smaller mass. It appears that the dependence on the chemical potential is missing, but one must be aware that the chiral phase transition can occur when \bar{B} is small. For instance at $T = 1$ and $\mu = 20$, the phase diagrams tell

us that there is no chiral phase transition for all values of \bar{B} , so the dashed curve of the diagram is not modified. However at $T = 1$ and $\mu = 40$, the chiral phase transition sets in at $\bar{B} \approx 4$ and the dashed curve for $T = 1$ in the diagram must be truncated below this value and m^* sharply drops down to zero at that point. Therefore, the B - m^* diagram depends on μ implicitly and μ determines where the mass drops to zero.

Figure 35 shows the T - m^* diagram. The lower temperature region of the diagram is subject to the truncation by the confinement/deconfinement phase transition at $\beta = \beta_4$. Thus, for example, if we have $\beta_4 = 1$, then the diagram must end at $T = 1$. The higher temperature region can end with the chiral phase transition, by dropping sharply to the zero mass. The chiral phase diagrams tell us, for example, that the $\bar{B} = 10$ curve must be truncated at $T = 1$ for $\mu \approx 57.6$ and at $T = 1.5$ for $\mu \approx 32.5$. So again, the truncation point depends on the value of the chemical potential.

Pure E Background

We now discuss the constant E background. As mentioned in Section 3.5, the introduction of the chemical potential is not allowed for this case. Moreover, the difference free energy ΔF in Equation (124) is complex and we follow what we have done for the NJL model: we treat the real and imaginary parts of the free energy separately. We extract the information about the phase diagram from the real part, and we make crude estimate on whether such information can be reliable, by checking if the imaginary part is subdominant. We are mainly interested in the zero temperature limit, since in the NJL counterpart, we had most information at zero temperature.

From Equations (131,132) for $T = 0$, we can obtain the dynamical mass as a function of E , and the result is shown in Figure 36. We see that E generally is a destabilizer of

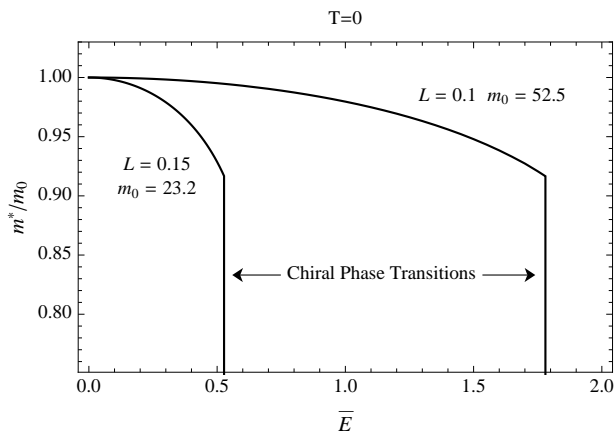


Figure 36: The SEP as a function of the E field at $T = 0$. The parameter m_0 is the m^* at $\bar{E} = 0$. The curves at higher value of \bar{E} is terminated at the chiral phase transition points.

the boundstate, as expected, and also the curves always terminate at the first order chiral phase transitions. Figure 37 shows the corresponding plots of the free energy in real and imaginary parts. This figure shows that the imaginary part is always comparable to the real part, especially near the phase transition points. Hence there is a doubt on the validity of the masses and the phase transitions shown in Figure 36. However, notice that m^{*2} is considerably larger than E . Recall that in the NJL counterpart, we also estimated the stability of the system by considering Schwinger's pair creation rate formula. The rate is

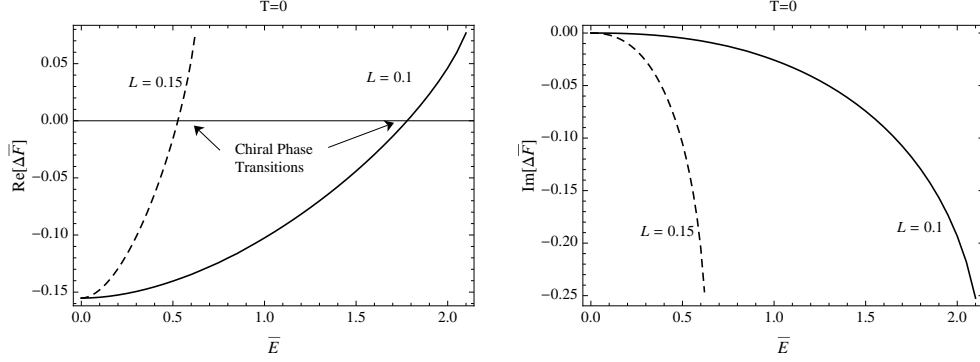


Figure 37: The free energy plotted separately for the real and the imaginary parts. The quantity \bar{F} is the right-hand side of Equation (124) where the factor of $(3y_R^{7/2})$ is omitted from the free energy.

exponentially suppressed by the factor m^{*2}/E and this indicates that the system of the SS model may have very slow pair creation rate. Therefore, it is reasonable to assume that the instability takes place slowly and the information about the mass and the phase transition can be meaningful.

The system at a finite temperature behaves as expected and it acts as a destabilizer. The masses at a certain value of \bar{E} is smaller at finite temperature than the zero temperature case and the first order chiral phase transition sets in at a smaller value of \bar{E} . The E - T phase diagram extracted from the real part of the difference free energy is plotted in Figure 38.

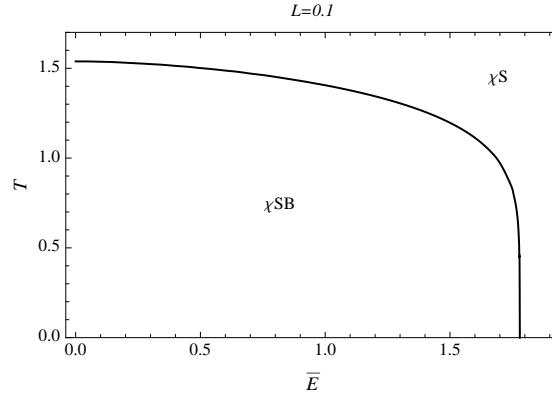


Figure 38: The E - T chiral phase diagram obtained from the real part of the free energy.

4 Comparison

We now have the data for the comparison between the NJL and SS models. In this section, we summarize the results by putting the NJL and SS data side by side.

4.1 General Observation

We first make general observations which are not specialized to purely B or E backgrounds.

Let us compare the NJL effective potential (54) and the probe action of the SS model in the confined phase with the Lagrangian (107). Both expressions are specific for the non-anomalous $\vec{B} \perp \vec{E}$ background configuration. The former is the expression for $T = 0$ and the latter is independent of the temperature, as long as the system is in the confined phase. We have already remarked under Equation (54) that for the cases with $|\vec{B}| > |\vec{E}|$ and $|\vec{B}| < |\vec{E}|$, the NJL system behaves as if there is only B - and E -field, respectively. The case with $|\vec{B}| = |\vec{E}|$ is special and the system is equivalent to the one without the electromagnetic background. Also the pure E -field case can be obtained from the pure B -field case just by sending $B \rightarrow iE$, and *vice versa*. As we can see clearly in Equation (107) that the same is true for the SS model probe action. A short inspection reveals that the zero temperature limit of the SS deconfined phase discussed near the end of Section 3.5 also shows the same behavior. (One must recall that $\mu = 0$ for $E \neq 0$.)

The finite temperature NJL effective potential (50) shows that the lack of Lorentz invariance destroys the features mentioned above. Also the probe Lagrangians of the SS model in the deconfined phase (120) lack the properties of the previous paragraph, because of the general appearance of the factor $f^{-1}E^2$ in \mathcal{A} .

Therefore, we see that even though the actions of the theories are very different, the effects of Lorentz invariance (at $T = 0$) and non-invariance (at $T \neq 0$) appear the same for both theories in a very general sense. However, we remark that for the anomalous case $\vec{B} \parallel \vec{E}$, apparent similarity is not observed.

We now look into the relation between the NJL coupling g and the inter-brane distance L of the SS model. The possible ranges of those parameters are shown in Figure 3 for the NJL coupling (plotted for $\pi^{3/2}/g^2$), Figure 25 for $\ell := L/\beta_4$ of the SS model in the confined phase and Figure 29 for $\hat{L} := L/R$ of the SS model in the deconfined phase. In the absence of B -field, the NJL model always has the lower limit on the coupling and below this critical coupling, the system is in the chirally symmetric phase. For example, the critical coupling for the zero temperature and zero chemical potential is 2π . The SS model in the confined phase also has a lower limit on ℓ^{-1} , namely, $\ell^{-1} = 2$. However, this lower limit is different in nature: it is the geometrical constraint rather than dynamical, and furthermore, at the critical point the chiral symmetry is still broken (the configuration is in the U shape) and the region $\ell^{-1} < 2$ is not defined, of course. The SS model in the deconfined phase at zero temperature does not have a lower limit on \hat{L}^{-1} and the chiral symmetry is always broken. However at finite temperature, there is a lower limit on \hat{L}^{-1} and below this critical value, the system is in the symmetric phase. So it seems that the NJL coupling g and ℓ^{-1} of the SS model in the confined phase behave rather differently, and g and \hat{L}^{-1} of the SS deconfined phase have general similarity at finite temperature.

To investigate further into the relation among those parameters, we have shown the response of the dynamical mass with respect to the parameters. Figure 6 is the plot for the NJL model and Figure 26 is the SS model in the confined phase and Figure 30 is the SS model in the deconfined phase. In general, the mass respond very differently, except that the higher g or L^{-1} gives the higher mass. However, examination into the region near the critical points of these parameters shows that there is a good similarity between g and \hat{L}^{-1} of the SS model in the deconfined phase at finite temperature. In those cases, the mass grows as square-root of the parameters.

The conclusion out of this comparison is that the parameter g of the NJL model and \hat{L}^{-1} of the SS model in deconfined phase at finite temperature correspond to each other fairly

well, especially near the critical values, and in all cases, the increase in the parameters result in the higher masses. However we observed that they are not in one-to-one correspondence and especially at zero temperature, they show the qualitative differences.

In what follows, we focus on the comparison between the NJL model and the SS model *in the deconfined phase*. This is because we have already seen that the correspondence is rather poor for the SS confined phase. Moreover, the confined phase does not have the dependence on the temperature nor on the chemical potential, and it does not even have the chiral phase transition. These facts make the confined phase rather meaningless in the comparison with the NJL model.

4.2 Pure B Background

When we turn on the B field at $T = 0$, the lower limit of the NJL coupling becomes zero and any finite temperature brings this to a finite value. (See Figure 8). This makes the correspondence of the parameter g of NJL and \hat{L}^{-1} of SS even better.

Let us proceed to consider the dynamical mass in the presence of the background B field. Compare the B - m^* diagram of the NJL model at $\mu = 0$ in Figure 12 and that of the deconfined SS model in Figure 34. We see the striking similarity in how the masses respond to the B field between the models. In the small B region, they both show the relation $m^* \sim B^2$ and this fact is more than just the general tendency of B as the stabilizer of the boundstate. The figures also show that the ways the masses in the models respond to the temperature are also similar.

We have, however, only looked at the $\mu = 0$ case so far. The finite chemical potential reveals the glaring differences between the models. The NJL model exhibits a very complicated behavior at finite chemical potential due to the de Haas-van Alphen oscillation and the destabilizing effect of B at large μ , as shown in Figure 13 (see also Figure 14). In contrast, the Figure 34 of the SS model does not change the shape at finite chemical potential, except that the lower B part of the curves can be truncated to zero mass as the chiral phase transition sets in. The dynamical mass of the SS model, SEP, is independent of the chemical potential (except at the chiral phase transition point), and this is why the μ - m^* diagram of Figure 11 for the NJL model does not have the counterpart in the SS model.

We can also see the similarities and dissimilarities due to the chemical potential in the phase diagrams. For example, we can look at the B - T phase diagrams of Figure 16 for the NJL model and Figure 31 for the SS model. When the value of the chemical potential is small, the NJL diagram appears very similar to the SS diagram. However, the “dent” in Figure 16 of NJL is due to the destabilization effect of B at large μ and this is not observed in the NJL diagram in Figure 31. Accordingly, the “cross” of the T - μ phase diagram in Figure 18 does not have the counterpart in the SS diagram in Figure 33.

Therefore, the models in the background B field behave very similar to each other when the chemical potential is zero or small, but as soon as the chemical potential becomes large enough to trigger the oscillation and the B -field destabilization, the models behave differently.

We also point out that the order of the chiral phase transition in the SS model is, by definition, all first order, because it is defined to be the point where the configuration jumps from U to \parallel or the other way around. Meanwhile in the NJL model, the transition is in general second order, as long as the chemical potential is low enough. When the chemical

potential becomes large, there is a mixture of the first and second order phase transitions in the phase diagrams.

4.3 Pure E Background

Turning on the background E field introduces the lower bound for both g and \hat{L}^{-1} even at $T = 0$, and the effect is similar to the finite temperature discussed in Section 4.1. Thus in this case, the qualitative agreement between g and \hat{L}^{-1} is good at all temperature.

Just like the temperature, the background electric field acts as the destabilizer in the both theories and this can be seen in E - m^* graph of Figure 19 for the NJL model and Figure 36 for the SS model. The NJL model shows both first and second order phase transitions depending on the coupling, and the SS model, by definition, shows only the first order transition. We noted that the m^{*2} to E ratio is very large for the SS model and this implies the slow rate of the pair creation. Therefore, the phase diagram of the SS model is more reliable than that of the NJL model.

In both models, the free energy is complex for any finite E , implying that the models are unstable in the E field background. We have seen that the real and imaginary parts are comparable to each other in both models. They are shown in Figure 20 for NJL and Figure 37 for SS.

5 Conclusion

We have seen good agreements between the NJL model and the *deconfined* phase of the SS model. Because the NJL model is nonrenormalizable, the cutoff must be introduced by hand and this makes the energy scale of the model unclear. One popularly advocated interpretation is that the model describes the very low energy regime of QCD and the cutoff is around Λ_{QCD} . Another interpretation is that since the model lacks the confinement, it describes QCD in the deconfined phase, but not too far from the phase transition point. As far as the comparison with the SS model is concerned, our study strongly implies the latter interpretation.

We have also seen the general discrepancy of the phase transition orders, and the most prominent differences between the models are the de Haas-van Alphen effect and the destabilizing effect of B at large μ , observed in NJL but not in SS. The cause of the differences can be reduced to the general fact that the SS model in the U configuration is totally independent of the chemical potential. Physically, if a model exhibits hadrons as boundstates of the quarks, the spectrum should certainly depend on the chemical potential. The SS model of the form we studied in this work does not show this behavior. Moreover, the lack of the de Haas-van Alphen and the destabilizing B effects imply that the SS model fails to incorporate the fermi sphere. Therefore, it appears that we need extra ingredients to the SS model, such as different brane configurations (which corresponds to additional phases) and extra terms in the probe action. Further investigation in this direction would deepen the understanding of the model's universality.

In this work, we have concentrated on the case with $N_f = 1$ and compared the dynamical mass of NJL and SEP of SS. It is of great interest to generalize the comparison to $N_f > 1$ and investigate the hadron spectrum, even quantitatively, and the effects of other features, such as the $U(1)_A$ breaking terms in both models.

Acknowledgments

I would like to thank Shmuel Elitzur, Andy O’Bannon and Jacob Sonnenschein for the useful discussions. This work was supported by the Center of Excellence of the ISF.

A Path Integrals of the Worldline Fields

We are going to evaluate the path integrals I_B and I_F defined in the beginning of Subsection 2.5. The derivation is not original and can be found elsewhere. We largely collect and reproduce the relevant parts of Reference [14] for the completeness, and specialize to the finite temperature system at the end.

We first consider the worldline fermionic part I_F . We split the field ψ into the part that satisfies the equation of motion Ψ (classical part) and the fluctuation part η as

$$\psi_\mu(\tau) = \Psi_\mu(\tau) + \eta_\mu(\tau) , \quad (133)$$

where they both satisfy the anti-periodic condition. The classical part $\Psi(\tau)$ satisfy

$$(\partial_\tau - 2iF)_{\mu\nu} \Psi_\nu(\tau) = 0 . \quad (134)$$

We can easily solve the equations of motion to get

$$\Psi_\mu(\tau) = (e^{2iF\tau})_{\mu\nu} C_\nu , \quad (135)$$

where C_ν are some constants. Since we have

$$\Psi_\mu(0) = C_\mu \quad \text{and} \quad \Psi_\mu(s) = (e^{2iFs})_{\mu\nu} C_\nu , \quad (136)$$

the anti-periodic condition $\Psi(0) = -\Psi(s)$ implies that

$$(\mathbf{1} + e^{2iFs})_{\mu\nu} C_\nu = 0 . \quad (137)$$

Assuming that the first factor is invertible, we get $C_\mu = 0$. Hence, we conclude that¹⁴

$$\Psi_\mu(\tau) = 0 . \quad (138)$$

We are therefore left with

$$\begin{aligned} I_F &= \int_A \mathcal{D}\psi_\mu(\tau) \exp\left[-\frac{1}{2} \int_0^s d\tau \eta \cdot (\partial_\tau - 2iF) \cdot \eta\right] = (\det_A[\partial_\tau - 2iF])^{1/2} \\ &= (\det_A[\partial_\tau])^{1/2} (\det_A[\mathbf{1} - 2iF\partial_\tau^{-1}])^{1/2} , \end{aligned} \quad (139)$$

where the subscript “A” of the determinant reminds us that the field is anti-periodic on the time circle and this accordingly affects the momentum. Notice that since the field $\eta(\tau)$ is

¹⁴ As in Reference [14], the action \mathcal{L}_ψ must be augmented by a surface term in general. However, in our case, the classical part vanishes and the surface term does not affect our discussion, hence omitted from the beginning.

real, the functional determinants have the power of $1/2$. Following Strassler [8], we adopt the normalization

$$(\det_A[\partial_\tau])^{1/2} = \sum_{\alpha=1}^4 \langle \alpha | \alpha \rangle = 4. \quad (140)$$

For the other factor, we quote the result from Reference [14],

$$(\det_A[\mathbf{1} - 2iF\partial_\tau^{-1}])^{1/2} = (\det_L[\cos(Fs)])^{1/2}, \quad (141)$$

where \det_L is the determinant with respect to the Lorentz structure. Putting those results together, we obtain the expression in Equation (47).

Let us now deal with the bosonic part I_B . As it always happens in a finite temperature field theory, the zero winding mode of bosonic sector needs a special care. As shown in Figure 2, this mode has closed paths. Among the paths, there are constant functions $x(\tau) \equiv x_0$ and this makes the functional determinant ill-defined. Therefore, the constants x_0 should be separated from the path integral and they all should be summed (or rather integrated) over. However, this integral is precisely the one extracted in the definition of the effective potential in Equation (24). So in practice, we do not have to worry about these constant paths and we can proceed by assuming that they are absent.

By virtue of the Schwinger-Fock gauge, the Lagrangian \mathcal{L}_{xSF} is quadratic and we rewrite it as

$$I_B = \mathcal{N} \int_{x(0)=\bar{x}}^{x(s)=\bar{y}} \mathcal{D}x(\tau) \exp\left[-\frac{1}{4} \int_0^s d\tau x \cdot (-\partial_\tau^2 + 2ieF\partial_\tau) \cdot x - \frac{1}{4} \{x(s) \cdot \dot{x}(s) - x(0) \cdot \dot{x}(0)\}\right], \quad (142)$$

where we kept the surface terms, because they will have the contribution from the classical paths. We split the field into the classical part $X(\tau)$ and the fluctuation $z(\tau)$ as

$$x(\tau) = X(\tau) + z(\tau), \quad (143)$$

where they satisfy

$$(-\partial_\tau^2 + 2ieF\partial_\tau)_{\mu\nu} X_\nu(\tau) = 0, \quad (144)$$

and

$$X(0) = \bar{x}, \quad X(s) = \bar{y} \quad \text{and} \quad z(0) = 0 = z(s). \quad (145)$$

The equations of motion (144) with the boundary conditions can be easily solved and yield

$$X(\tau) = \bar{x} + \frac{1 - \exp(2ieF\tau)}{1 - \exp(2ieFs)} (\bar{y} - \bar{x}). \quad (146)$$

This gives the contribution to the surface terms of I_B ,

$$-\frac{1}{4} \{x(s) \cdot \dot{x}(s) - x(0) \cdot \dot{x}(0)\} = -\frac{1}{4} (\bar{y} - \bar{x}) \cdot eF \cot(eFs) \cdot (\bar{y} - \bar{x}). \quad (147)$$

The path integral now is over the fluctuation $z(\tau)$ and this gives

$$\begin{aligned} \mathcal{N}(\det'_P[-\partial_\tau^2 + 2ieF\partial_\tau])^{-1/2} &= \mathcal{N}(\det'_P[-\partial_\tau^2]^{-1/2})(\det'_P[\mathbf{1} - 2ieF\partial_\tau^{-1}]^{-1/2}) \\ &= (4\pi s)^{-d/2} \left(\det_L \left[\frac{\sin(eFs)}{eFs} \right] \right)^{-1/2}, \end{aligned} \quad (148)$$

where the prime on the determinant indicates that we omit the constant paths, we have used Equation (35) and the evaluation of the last determinant in the first line is quoted from Reference [14]. We thus have

$$I_B = (4\pi s)^{-d/2} \exp \left[-\frac{1}{4}(\bar{y} - \bar{x}) \cdot eF \cot(eFs) \cdot (\bar{y} - \bar{x}) \right] \left(\det_L \left[\frac{\sin(eFs)}{eFs} \right] \right)^{-1/2}. \quad (149)$$

Now according to the finite temperature prescription (37), we should set

$$\bar{y} = \bar{x} + n\beta\hat{x}_0, \quad (150)$$

where \hat{x}_0 is the unit vector in the time direction. We then have

$$I_B = (4\pi s)^{-d/2} \exp \left[-(n\beta/2)^2 \{eF \cot(eFs)\}_{00} \right] \left(\det_L \left[\frac{\sin(eFs)}{eFs} \right] \right)^{-1/2}. \quad (151)$$

B Computation of the Functions of $F_{\mu\nu}$

In this appendix, we compute $\{\det_L[(Fs) \cot(Fs)]\}^{1/2}$ and $\{(Fs) \cot(Fs)\}_{00}$. The former can be evaluated along the method of Schwinger [15] and the latter is difficult and we adopt the method of Reference [38] (see also [39]). Both discussions are recast to the Euclidean version in below.

We have the Euclidean version of the field strength

$$F_{\mu\nu} = \begin{pmatrix} 0 & -iE_1 & -iE_2 & -iE_3 \\ iE_1 & 0 & B_3 & -B_2 \\ iE_2 & -B_3 & 0 & B_1 \\ iE_3 & B_2 & -B_1 & 0 \end{pmatrix}, \quad (152)$$

and in the four spacetime dimension, we have the dual of the same rank

$$\begin{aligned} \tilde{F}_{\mu\nu} &:= \frac{1}{2} \epsilon_{\mu\nu\alpha\beta} F_{\alpha\beta} \\ &= \begin{pmatrix} 0 & B_1 & B_2 & B_3 \\ -B_1 & 0 & -iE_3 & iE_2 \\ -B_2 & iE_3 & 0 & -iE_1 \\ -B_3 & -iE_2 & iE_1 & 0 \end{pmatrix}, \end{aligned} \quad (153)$$

where we have used the convention $\epsilon_{0123} = +1$. We then have the invariants

$$\mathcal{F} := -\frac{1}{4} F_{\mu\nu} F_{\mu\nu} = \frac{1}{2} (\vec{B}^2 - \vec{E}^2) \quad \text{and} \quad \mathcal{G} := -\frac{i}{4} F_{\mu\nu} \tilde{F}_{\mu\nu} = \vec{E} \cdot \vec{B}. \quad (154)$$

We first calculate the determinant. The important identities are

$$F_{\mu\lambda}F_{\lambda\nu} + \tilde{F}_{\mu\lambda}\tilde{F}_{\lambda\nu} = -2\mathcal{F}\delta_{\mu\nu} , \quad (155)$$

and

$$F_{\mu\lambda}\tilde{F}_{\lambda\nu} = i\mathcal{G}\delta_{\mu\nu} . \quad (156)$$

Using those, we derive the eigenvalues of $F_{\mu\nu}$ in terms of \mathcal{F} and \mathcal{G} . Let ψ_μ and f be the eigenvector and eigenvalue of $F_{\mu\nu}$, respectively. We then have

$$\tilde{F}_{\mu\nu}F_{\nu\lambda}\psi_\lambda = f\tilde{F}_{\mu\nu}\psi_\nu = i\mathcal{G}\psi_\mu , \quad (157)$$

and this implies that

$$\tilde{F}_{\mu\nu}\psi_\nu = if^{-1}\mathcal{G}\psi_\mu . \quad (158)$$

By iteration, we have

$$F_{\mu\nu}F_{\nu\lambda}\psi_\lambda = f^2\psi_\mu \quad \text{and} \quad \tilde{F}_{\mu\nu}\tilde{F}_{\nu\lambda}\psi_\lambda = -f^{-2}\mathcal{G}^2\psi_\mu . \quad (159)$$

Then the identity (155) gives the eigenvalue equation

$$f^4 + 2\mathcal{F}f^2 - \mathcal{G} = 0 , \quad (160)$$

with the solutions $\pm f_\pm$ (signs are arbitrary, *i.e.*, 4 values) where

$$f_\pm = i\sqrt{\mathcal{F} \pm \sqrt{\mathcal{F}^2 + \mathcal{G}^2}} . \quad (161)$$

Note that any function of a matrix, $\Phi(F)$, is defined as the formal power series. Therefore, the argument of a determinant can be diagonalized and the determinant reduces to the product of the functions $\Pi_i\Phi(f_i)$, where f_i are the eigenvalues of F . We thus have

$$\det_L[(Fs) \cot(Fs)] = \{s^2 f_+ f_- \cot(f_+ s) \cot(f_- s)\}^2 . \quad (162)$$

Since we have

$$(f_+ f_-)^2 = -\mathcal{G}^2 , \quad (163)$$

we immediately get the result

$$\begin{aligned} & \{\det_L[(Fs) \cot(Fs)]\}^{1/2} = \\ & = s^2 \left| \mathcal{G} \coth \left(s\sqrt{\mathcal{F} + \sqrt{\mathcal{F}^2 + \mathcal{G}^2}} \right) \cot \left(s\sqrt{-\mathcal{F} + \sqrt{\mathcal{F}^2 + \mathcal{G}^2}} \right) \right| . \end{aligned} \quad (164)$$

We now evaluate $\{(Fs) \cot(Fs)\}_{00}$. We define

$$\begin{aligned} f_1 & := f_+ = i\sqrt{\mathcal{F} + \sqrt{\mathcal{F}^2 + \mathcal{G}^2}} , & \bar{f}_1 & := if_- = -\sqrt{\mathcal{F} - \sqrt{\mathcal{F}^2 + \mathcal{G}^2}} , \\ f_2 & := -f_+ = -i\sqrt{\mathcal{F} + \sqrt{\mathcal{F}^2 + \mathcal{G}^2}} , & \bar{f}_2 & := -if_- = \sqrt{\mathcal{F} - \sqrt{\mathcal{F}^2 + \mathcal{G}^2}} , \\ f_3 & := -f_- = -i\sqrt{\mathcal{F} - \sqrt{\mathcal{F}^2 + \mathcal{G}^2}} , & \bar{f}_3 & := -if_+ = \sqrt{\mathcal{F} + \sqrt{\mathcal{F}^2 + \mathcal{G}^2}} , \\ f_4 & := f_- = i\sqrt{\mathcal{F} - \sqrt{\mathcal{F}^2 + \mathcal{G}^2}} , & \bar{f}_4 & := if_+ = -\sqrt{\mathcal{F} + \sqrt{\mathcal{F}^2 + \mathcal{G}^2}} , \end{aligned}$$

and a sign

$$s := \mathcal{G}/|\mathcal{G}| = |\mathcal{G}|/\mathcal{G}. \quad (165)$$

Then, the matrices

$$A_{(i)\mu\nu} := \frac{1}{2(f_i^2 + \bar{f}_i^2)} (\bar{f}_i^2 \delta_{\mu\nu} + f_i F_{\mu\nu} + F_{\mu\lambda} F_{\lambda\nu} - is \bar{f}_i \tilde{F}_{\mu\nu}) \quad (166)$$

satisfy the relations

$$F_{\mu\lambda} A_{(i)\lambda\nu} = f_i A_{(i)\mu\nu} = A_{(i)\mu\lambda} F_{\lambda\nu} \quad \text{and} \quad \sum_i A_{(i)\mu\nu} = \delta_{\mu\nu}. \quad (167)$$

Using these two relations, we have for a function $\Phi(F)$,

$$\Phi(F)_{\mu\nu} = \sum_i A_{(i)\mu\nu} \Phi(f_i). \quad (168)$$

This is the key point of introducing the matrices $A_{(i)}$. Now, from this relation, we have

$$\{(Fs) \cot(eFs)\}_{00} = \sum_i A_{(i)00} (f_i s) \cot(f_i s). \quad (169)$$

Since

$$F_{00} = 0 = \tilde{F}_{00} \quad \text{and} \quad F_{0\lambda} F_{\lambda 0} = \vec{E}^2 \quad (170)$$

we have

$$A_{(i)00} = \frac{\bar{f}_i^2 + \vec{E}^2}{2(f_i^2 + \bar{f}_i^2)}, \quad (171)$$

and thus

$$\{(Fs) \cot(Fs)\}_{00} = \frac{s}{f_-^2 - f_+^2} \{ (f_-^2 - \vec{E}^2) f_+ \cot(f_+ s) - (f_+^2 - \vec{E}^2) f_- \cot(f_- s) \}. \quad (172)$$

We have

$$f_-^2 - f_+^2 = 2\sqrt{\mathcal{F}^2 + \mathcal{G}^2}. \quad (173)$$

and

$$f_{\pm}^2 - \vec{E}^2 = -\frac{1}{2}(\vec{B}^2 + \vec{E}^2) \mp \sqrt{\mathcal{F}^2 + \mathcal{G}^2}. \quad (174)$$

We also have

$$\begin{aligned} f_+ \cot(f_+ s) &= \sqrt{\mathcal{F} + \sqrt{\mathcal{F}^2 + \mathcal{G}^2}} \coth(s \sqrt{\mathcal{F} + \sqrt{\mathcal{F}^2 + \mathcal{G}^2}}) \\ f_- \cot(f_- s) &= \sqrt{-\mathcal{F} + \sqrt{\mathcal{F}^2 + \mathcal{G}^2}} \cot(s \sqrt{-\mathcal{F} + \sqrt{\mathcal{F}^2 + \mathcal{G}^2}}). \end{aligned} \quad (175)$$

So we get

$$\begin{aligned} \{eF \cot(eFs)\}_{00} &= \frac{1}{2\sqrt{\mathcal{F}^2 + \mathcal{G}^2}} \left[\right. \\ &\left\{ -\frac{1}{2}(\vec{B}^2 + \vec{E}^2) + \sqrt{\mathcal{F}^2 + \mathcal{G}^2} \right\} e \sqrt{\mathcal{F} + \sqrt{\mathcal{F}^2 + \mathcal{G}^2}} \coth \left(es \sqrt{\mathcal{F} + \sqrt{\mathcal{F}^2 + \mathcal{G}^2}} \right) \\ &+ \left\{ \frac{1}{2}(\vec{B}^2 + \vec{E}^2) + \sqrt{\mathcal{F}^2 + \mathcal{G}^2} \right\} e \sqrt{-\mathcal{F} + \sqrt{\mathcal{F}^2 + \mathcal{G}^2}} \cot \left(es \sqrt{-\mathcal{F} + \sqrt{\mathcal{F}^2 + \mathcal{G}^2}} \right) \left. \right]. \end{aligned} \quad (176)$$

C Treatment of Large Chemical Potential

In Section 2.5.1, we have pointed out that a special treatment is necessary when the chemical potential of the system is too large. In this appendix, we give the details of how to handle this case. The discussion here is somewhat similar to Reference [42]. For simplicity, we first consider the system without the constant background field, hence the goal is to evaluate

$$\frac{T}{4\pi^{3/2}} \int_1^\infty ds s^{-5/2} \sum_{l \in \mathbb{Z}_{1/2}} \exp[-s\{(2\pi Tl - i\mu)^2 + m^2\}], \quad (177)$$

for a general value of μ . The inclusion of B -field (and E -field) can be done in relative ease.

We first discuss the analytic continuation of the proptime in general. Recall that we have dealt with the ‘‘Euclidean worldline Lagrangian’’ appearing in Equations (33,34). This stems from our choice of the proptime variable in Equation (29). There, we chose it so that the exponential appears as real, whereas Schwinger chooses in Ref. [15] as

$$\ln X = - \int_0^\infty \frac{e^{-iXt}}{t} dt. \quad (178)$$

This choice leads to the evolution equation of the real proptime. Therefore, we can think of our choice as the analytically continued version, *i.e.*, the *imaginary* proptime s . See Figure 39.

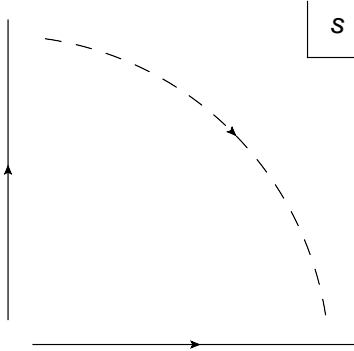


Figure 39: Analytic continuation of real to imaginary proptime. Since our notation is that s is the imaginary proptime, the vertical axis corresponds to the real proptime.

We note that the situation is a little more complicated when we must introduce the cutoff at $s = 1$. In this case, it seems as if we have discrepancy with the real proptime case due to the quarter circle contribution. See Figure 40. However, the cutoff is designed to make the imaginary proptime integral well-defined, and it is nonsensical in the real one. Therefore, we *define* the world of real proptime as the analytic continuation of the imaginary proptime with the cutoff. This implies that the contour C_1 in Figure 40 corresponds to $C_r + C_{p3}$.

Now, we notice that we have choices to analytically continue from the real to imaginary proptime: $t \rightarrow s$ or $t \rightarrow -s$, in other words, it is also possible to analytically continue to the left of Figure 39. The former choice has been made in Equation (29) and we found that this choice is not suitable when the chemical potential is too large. When this is the case,

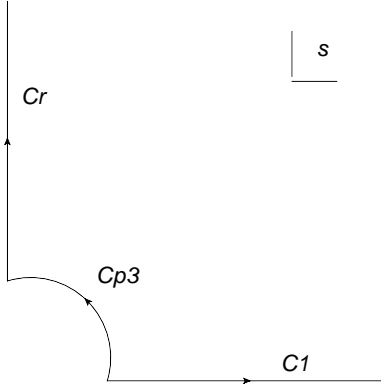


Figure 40: With the introduction of the cutoff, the real and imaginary proptimes have difference due to the quarter circle. We therefore, *define* the real counterpart with the quarter-circle contribution: $C_1 \Leftrightarrow C_r + C_{p3}$.

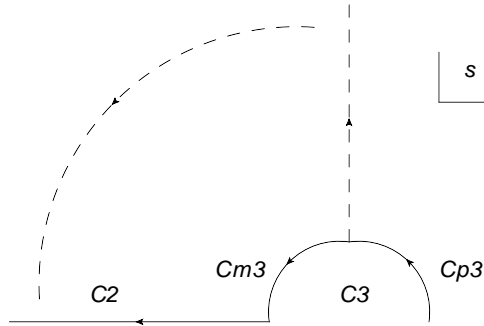


Figure 41: The analytic continuation from positive to negative real axis. The contour C_1 now corresponds to $C_2 + C_3$, where $C_3 := C_{p3} + C_{m3}$.

we must pick the other choice. This amounts to the analytic continuation of the variable s in Equation (177) from the positive to the negative direction as shown in Figure 41.

We must be careful about which way we should close the contour. The imaginary part of the exponential in Equation (177) is $2\pi i \mu T l s$ and this tells us that we should close the contour above when l is positive and below when l is negative, so that the large circles do not contribute to the integral. See Figure 42. Finally, we must be careful with the branch cut that arise from the factor of $s^{-5/2}$ in Equation (177). The contour should not cross the cut and this is possible only when the cut runs along the negative horizontal axis. This causes the ambiguity in choosing the branch of $s^{-5/2}$ on the negative real axis. We take the convention that when we close the contour below, we choose the second branch value. Later, we will show that this is the consistent choice.

When we have the B field, we have poles along the vertical axis in the s -plane and we must pick them up, as they are within the contour. We will deal with this later.

Let us actually evaluate Equation (177). As mentioned in Section 2.5.1, the integral converges only when

$$(2\pi T l)^2 - \mu^2 + m^2 > 0, \quad (179)$$

is satisfied. Without loss of generality, let us assume that $\mu \geq 0$ and $m \geq 0$. When $\mu < m$,

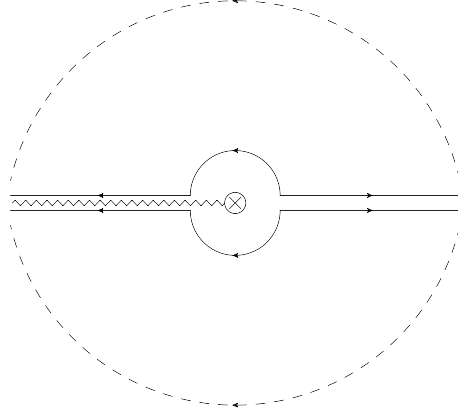


Figure 42: Analytic continuation of the variable s from positive to negative real axis. The upper (resp. lower) contour should be chosen for positive (resp. negative) l . The branch cut comes from the factor of $s^{-5/2}$ in Equation (177). The branch cut must run along the negative real axis to avoid the cross-over with the contours. Our convention is that when we take the lower contour, the value of $s^{-5/2}$ is taken to be on the second branch for the negative real axis.

this condition is satisfied for all l , but when $\mu > m$, it is satisfied only for $|l| > \bar{l}$ with

$$\bar{l} := \left[(2\pi T)^{-1} \theta(\mu - m) \sqrt{\mu^2 - m^2} \right]_G, \quad (180)$$

where $\theta(x)$ is the Heaviside theta and the symbol $[x]_G$ is the half-integer version of the Gauss symbol, *i.e.*, it is the largest half integer less than or equal to x . Notice, in particular, that when $\mu < m$, we have $\bar{l} = -1/2$ and l runs over all half integers. According to the previous discussion, Equation (177) must be split at \bar{l} and for positive and negative l . Thus, we write

$$\begin{aligned} \text{Eqn. (177)} &= \frac{T}{4\pi^{3/2}} \int_{C_1} ds s^{-5/2} \sum_{|l| > \bar{l}} \exp \left[-s \{ (2\pi T l - i\mu)^2 + m^2 \} \right] \\ &+ \frac{T}{4\pi^{3/2}} \int_{(C_2+C_3)_{\text{up}}} ds s^{-5/2} \sum_{l=1/2}^{\bar{l}} \exp \left[-s \{ (2\pi T l - i\mu)^2 + m^2 \} \right] \\ &+ \frac{T}{4\pi^{3/2}} \int_{(C_2+C_3)_{\text{down}}} ds s^{-5/2} \sum_{l=-\bar{l}}^{-1/2} \exp \left[-s \{ (2\pi T l - i\mu)^2 + m^2 \} \right], \quad (181) \end{aligned}$$

where “up” and “down” indicated on the integration contour implies the way the contour is closed as in Figure 42. Consider the integral in the last line. Since the both integral and sum are well-defined now, we may exchange them. Also we send the summation variable l

to $-l$. We then have

$$\begin{aligned}
& \frac{T}{4\pi^{3/2}} \sum_{l=1/2}^{\bar{l}} \int_{(C_2+C_3)\text{down}} ds s^{-5/2} \exp[-s\{(2\pi Tl + i\mu)^2 + m^2\}] \\
&= \frac{T}{4\pi^{3/2}} \sum_{l=1/2}^{\bar{l}} \int_{(C_2)\text{down}} ds s^{-5/2} \exp[-s\{(2\pi Tl + i\mu)^2 + m^2\}] \\
&\quad + \frac{T}{4\pi^{3/2}} \sum_{l=1/2}^{\bar{l}} \int_{(C_3)\text{down}} ds s^{-5/2} \exp[-s\{(2\pi Tl + i\mu)^2 + m^2\}] \\
&= -i \frac{T}{4\pi^{3/2}} \sum_{l=1/2}^{\bar{l}} \int_1^\infty ds s^{-5/2} \exp[s\{(2\pi Tl + i\mu)^2 + m^2\}] \\
&\quad - i \frac{T}{4\pi^{3/2}} \sum_{l=1/2}^{\bar{l}} \int_0^\pi d\phi e^{\frac{3}{2}i\phi} \exp[-e^{-i\phi}\{(2\pi Tl + i\mu)^2 + m^2\}], \tag{182}
\end{aligned}$$

where we have taken the second branch value for the negative real axis as our convention and the sign of the integral variable ϕ was reversed so that now the integration range is $(0, \pi)$ rather than $(0, -\pi)$. A little inspection shows that this is exactly the complex conjugate of the second line in Equation (181).

We can also split the first line in Equation (181) into positive and negative sums and it is easy to see that they are complex conjugate of each other. Therefore, we can write

$$\begin{aligned}
\text{Eqn. (177)} &= \frac{T}{2\pi^{3/2}} \text{Re} \left[\sum_{l>\bar{l}}^\infty \int_1^\infty ds s^{-5/2} \exp[-s\{(2\pi Tl - i\mu)^2 + m^2\}] \right. \\
&\quad + i \sum_{l=1/2}^{\bar{l}} \int_1^\infty ds s^{-5/2} \exp[s\{(2\pi Tl - i\mu)^2 + m^2\}] \\
&\quad \left. + i \sum_{l=1/2}^{\bar{l}} \int_0^\pi d\phi e^{-\frac{3}{2}i\phi} \exp[-e^{i\phi}\{(2\pi Tl - i\mu)^2 + m^2\}] \right]. \tag{183}
\end{aligned}$$

After so much ado, we point out the following. In Equation (177), assuming that $|l| > \bar{l}$, we can, in principle, carry out s -integral before the sum. The result is a function of l and valid only when $|l| > \bar{l}$. *However, we can analytically continue* the integral beyond the validity range of l to cover all half integers, without worrying about the case by case examination that we have done. In fact, one can find a closed form of the s integral in Equation (177) and verify this claim by comparing with the result (183). This in turn implies the validity of the choice of the branch cut for the lower contour discussed before. In practice, when the B field is present, we are not able to find the closed form of s -integral and must resort to the case by case integral. In what follows, we discuss this case more.

As mentioned earlier, the case with the pure B -field has simple poles along the imaginary axis in the s -plane, due to the factor of hyperbolic cosine in Equation (57). Therefore, when we must analytically continue s to the negative horizontal axis, we need to pick up

the poles. The condition for \bar{l} , which determines the point for the analytic continuation, is not affected by the presence of the hyperbolic cosine, because it approaches 1 at large s . Hence the expressions for this case is similar to the previous case except for the extra contributions from the poles.

$$\begin{aligned}
\hat{V}_{\text{eff}} = & \frac{m^2}{2g^2} + \frac{T}{2\pi^{3/2}} \text{Re} \left[\int_1^\infty ds (sB) \coth(sB) s^{-5/2} \sum_{l>\bar{l}} \exp \left[-s \{ (2\pi Tl - i\mu)^2 + m^2 \} \right] \right. \\
& + i \int_1^\infty ds (sB) \coth(sB) s^{-5/2} \sum_{l=1/2}^{\bar{l}} \exp \left[s \{ (2\pi Tl - i\mu)^2 + m^2 \} \right] \\
& + i \int_0^\pi d\phi (e^{i\phi} B) \coth(e^{i\phi} B) e^{-\frac{3}{2}i\phi} \sum_{l=1/2}^{\bar{l}} \exp \left[-e^{i\phi} \{ (2\pi Tl - i\mu)^2 + m^2 \} \right] \\
& \left. + (2\pi i) \sum_{l=1/2}^{\bar{l}} \sum_{k=k_b}^\infty e^{-\frac{3}{4}\pi i} \left(\frac{B}{k\pi} \right)^{3/2} \exp \left[-ik \frac{\pi}{B} \{ (2\pi Tl - i\mu)^2 + m^2 \} \right] \right]. \quad (184)
\end{aligned}$$

Since the location of the poles are at

$$s = in\pi/B \quad \text{for all } n \in \mathbb{Z}, \quad (185)$$

for sufficiently large B , the pole at $n = 1$ (and more) comes inside the unit circle that we are excluding. Thus naively, we might exclude those poles that are inside the unit circle, *i.e.*, we set

$$k_b = \left[\frac{B}{\pi} + 1 \right]_G, \quad (186)$$

where $[y]_G$ here is the usual integer Gauss symbol. However, numerical evaluation reveals that this cross over results in a huge jump in the effective potential and it does not appear physical. This is the indication that the B field may not be much larger than the cutoff so that the poles of $n > 0$ should not cross the circle. This means that we must have $B < \pi$ and $k_b = 1$.

References

- [1] Y. Nambu and G. Jona-Lasinio, *Dynamical model of elementary particles based on an analogy with superconductivity. I*, Phys. Rev. **122**, 345 (1961).
- [2] J. M. Maldacena, *The large N limit of superconformal field theories and supergravity*, Adv. Theor. Math. Phys. **2**, 231 (1998) [Int. J. Theor. Phys. **38**, 1113 (1999)] [arXiv:hep-th/9711200].
- [3] S. S. Gubser, I. R. Klebanov and A. M. Polyakov, *Gauge theory correlators from non-critical string theory*, Phys. Lett. B **428**, 105 (1998) [arXiv:hep-th/9802109].
- [4] E. Witten, *Anti-de Sitter space and holography*, Adv. Theor. Math. Phys. **2**, 253 (1998) [arXiv:hep-th/9802150].
- [5] T. Sakai and S. Sugimoto, *Low energy hadron physics in holographic QCD*, Prog. Theor. Phys. **113**, 843 (2005) [arXiv:hep-th/0412141].
- [6] T. Hatsuda and T. Kunihiro, *QCD phenomenology based on a chiral effective Lagrangian*, Phys. Rept. **247**, 221 (1994) [arXiv:hep-ph/9401310].
- [7] S. P. Klevansky, *The Nambu-Jona-Lasinio model of quantum chromodynamics*, Rev. Mod. Phys. **64**, 649 (1992).
- [8] M. J. Strassler, *Field theory without Feynman diagrams: One loop effective actions*, Nucl. Phys. B **385**, 145 (1992) [arXiv:hep-ph/9205205].
- [9] C. Schubert, *Perturbative quantum field theory in the string-inspired formalism*, Phys. Rept. **355**, 73 (2001) [arXiv:hep-th/0101036].
- [10] J. Erdmenger, R. Meyer and J. P. Shock, *AdS/CFT with Flavour in Electric and Magnetic Kalb-Ramond Fields*, JHEP **0712**, 091 (2007) [arXiv:0709.1551 [hep-th]].
- [11] I. A. Shovkovy, *One-loop finite temperature effective potential in QED in the world-line approach*, Phys. Lett. B **441**, 313 (1998) [arXiv:hep-th/9806156].
- [12] H. Gies, *QED effective action at finite temperature*, Phys. Rev. D **60**, 105002 (1999) [arXiv:hep-ph/9812436].
- [13] M. Haack and M. G. Schmidt, *Axion decay in a constant electromagnetic background field and at finite temperature using world-line methods*, Eur. Phys. J. C **7**, 149 (1999) [arXiv:hep-th/9806138].
- [14] M. Reuter, M. G. Schmidt and C. Schubert, *Constant external fields in gauge theory and the spin 0, 1/2, 1 path integrals*, Annals Phys. **259**, 313 (1997) [arXiv:hep-th/9610191].
- [15] J. S. Schwinger, *On gauge invariance and vacuum polarization*, Phys. Rev. **82**, 664 (1951).
- [16] B. J. Harrington, S. Y. Park and A. Yildiz, *External Field Induced Phase Transition In The N -Component Thirring Model*, Phys. Rev. D **11**, 1472 (1975).

- [17] P. Elmfors, D. Persson and B. S. Skagerstam, *Real time thermal propagators and the QED effective action for an external magnetic field*, *Astropart. Phys.* **2**, 299 (1994) [arXiv:hep-ph/9312226].
- [18] P. Elmfors and B. S. Skagerstam, *Electromagnetic fields in a thermal background*, *Phys. Lett. B* **348**, 141 (1995) [Erratum-ibid. B **376**, 330 (1996)] [arXiv:hep-th/9404106].
- [19] V. P. Gusynin, V. A. Miransky and I. A. Shovkovy, *Dimensional reduction and catalysis of dynamical symmetry breaking by a magnetic field*, *Nucl. Phys. B* **462**, 249 (1996) [arXiv:hep-ph/9509320].
- [20] T. Inagaki, D. Kimura and T. Murata, *Four-fermion interaction model in a constant magnetic field at finite temperature and chemical potential*, *Prog. Theor. Phys.* **111**, 371 (2004) [arXiv:hep-ph/0312005].
- [21] S. P. Klevansky and R. H. Lemmer, *Chiral Symmetry Restriction in the Nambu-Jona-Lasinio Model with a Constant Electromagnetic Field*, *Phys. Rev. D* **39**, 3478 (1989).
- [22] O. Aharony, J. Sonnenschein and S. Yankielowicz, *A holographic model of deconfinement and chiral symmetry restoration*, *Annals Phys.* **322**, 1420 (2007) [arXiv:hep-th/0604161].
- [23] R. Casero, A. Paredes and J. Sonnenschein, *Fundamental matter, meson spectroscopy and non-critical string / gauge duality*, *JHEP* **0601**, 127 (2006) [arXiv:hep-th/0510110].
- [24] K. Peeters, J. Sonnenschein and M. Zamaklar, *Holographic melting and related properties of mesons in a quark gluon plasma*, *Phys. Rev. D* **74**, 106008 (2006) [arXiv:hep-th/0606195].
- [25] N. Horigome and Y. Tanii, *Holographic chiral phase transition with chemical potential*, *JHEP* **0701**, 072 (2007) [arXiv:hep-th/0608198].
- [26] O. Bergman, G. Lifschytz and M. Lippert, *Response of Holographic QCD to Electric and Magnetic Fields*, *JHEP* **0805**, 007 (2008) [arXiv:0802.3720 [hep-th]].
- [27] O. Bergman, G. Lifschytz and M. Lippert, *Magnetic properties of dense holographic QCD*, arXiv:0806.0366 [hep-th].
- [28] G. Lifschytz and M. Lippert, *Anomalous conductivity in holographic QCD*, arXiv:0904.4772 [hep-th].
- [29] C. V. Johnson and A. Kundu, *External Fields and Chiral Symmetry Breaking in the Sakai-Sugimoto Model*, *JHEP* **0812**, 053 (2008) [arXiv:0803.0038 [hep-th]].
- [30] K. Y. Kim, S. J. Sin and I. Zahed, *Dense and Hot Holographic QCD: Finite Baryonic E Field*, *JHEP* **0807**, 096 (2008) [arXiv:0803.0318 [hep-th]].
- [31] C. V. Johnson and A. Kundu, *Meson Spectra and Magnetic Fields in the Sakai-Sugimoto Model*, *JHEP* **0907**, 103 (2009) [arXiv:0904.4320 [hep-th]].

- [32] S. R. Coleman and E. J. Weinberg, *Radiative Corrections As The Origin Of Spontaneous Symmetry Breaking*, Phys. Rev. D **7**, 1888 (1973).
- [33] J. Polchinski, *String theory*, Vol. 1 and 2, Cambridge, UK: Univ. Pr. (1998)
- [34] L. s. Schulman, *Techniques and Applications of Path Integration*, New York, USA: Wiley (1981)
- [35] D. G. C. McKeon and A. Rebhan, *Thermal Green's functions from quantum mechanical path integrals*, Phys. Rev. D **47**, 5487 (1993) [arXiv:hep-th/9211076].
- [36] D. G. C. McKeon and A. K. Rebhan, *Thermal Green's functions from quantum mechanical path integrals 2: Inclusion of fermions*, Phys. Rev. D **49**, 1047 (1994) [arXiv:hep-th/9306148].
- [37] M. Nakahara, *Geometry, topology and physics*, Bristol, UK: Hilger (1990)
- [38] I. A. Batalin and A. E. Shabad, *Photon green function in a stationary homogeneous field of the most general form*, Zh. Eksp. Teor. Fiz. **60**, 894 (1971).
- [39] V. P. Gusynin and I. A. Shovkovy, *Derivative expansion of the effective action for QED in 2+1 and 3+1 dimensions*, J. Math. Phys. **40**, 5406 (1999) [arXiv:hep-th/9804143].
- [40] P. de Forcrand *et al.* [QCD-TARO Collaboration], *Meson correlators in finite temperature lattice QCD*, Phys. Rev. D **63**, 054501 (2001) [arXiv:hep-lat/0008005].
- [41] A. Karch and A. O'Bannon, *Metallic AdS/CFT*, JHEP **0709**, 024 (2007) [arXiv:0705.3870 [hep-th]].
- [42] T. Inagaki, D. Kimura and T. Murata, *Proper-time formalism in a constant magnetic field at finite temperature and chemical potential*, Int. J. Mod. Phys. A **20**, 4995 (2005) [arXiv:hep-ph/0307289].